LASER DIRECT-WRITE MICROFABRICATION AND PATTERNING

by

Dajun Yuan

A dissertation submitted in partial fulfillment
of the requirements for the degree of
Doctor of Philosophy
(Mechanical Engineering)
in The University of Michigan
2008

Doctoral Committee:

Associate Professor Katsuo Kurabayashi, Co-Chair
Associate Professor Suman Das, Georgia Institute of Technology, Co-Chair
Professor John W. Halloran
Assistant Professor Shorya Awtar

THE UNIVERSITY OF MICHIGAN
ARTES · SCIENTIA · VERITAS
1817

MichiganEngineering

© Dajun Yuan 2008
All Rights Reserved

ACKNOWLEDGEMENTS

This thesis and the research presented in this thesis were made possible by the support and guidance of many individuals. Without them, the completion of this work would not be possible.

First, I would like to thank my advisor Dr. Suman Das for his inspiration, guidance, and confidence in my abilities. His insights have guided me to a level of understanding far higher than what I thought was possible. I would also like to thank my other committee members; Dr. Katsuo Kurabayashi, Dr. John Halloran and Dr. Shorya Awtar for their support of and direction to my research.

I was fortunate to be a part of the intellectually Direct Digital Manufacturing Laboratory at Georgia Institute of Technology. I would like to thank all my colleagues, Dr. Andrés Fabián Lasagni, Paul Cilino, Chan Yoon, Siddharth Ram Athreya, Peng Shao, kiran rao kambly, Michael Kirka, Rohan Bansal, and Anirudh Rudraraju.

I thank Dr. David Martin's group in University of Michigan for providing PEDOT-PSS thin films for my experiments.

Last but not least, I would like to express my gratitude towards my parents and my grandparents for their devotion and help in all the stages of my life; I thank my girlfriend Wenli Xiao for making my life full of love and happiness; my sister Zheng Yuan for her affection and conviction. To them I dedicate this thesis.

TABLE OF CONTENTS

ACKNOWLEDGEMENTS……………………………………………..…..………ii

LIST OF FIGURES……………………….………………………..…..….....vii

LIST OF TABLES……………………………………………….….…,…....xiv

ABSTRACT………………………………………………......…......………xv

CHAPTER

I. INTURODUCTION...………….……….…………….…...………1

1.1 Microfabrication and micropatterning via replication…………………...….2

1.1.1 Photolithography……………………………………………….……..2

1.1.2 Micro-moulding, micro-embossing, and micro-contact printing….…....6

1.2 Maskless microfabrication and micropatterning…………………….……9

1.2.1 Direct-writing with a beam of energetic particles…………………......9

1.2.2 Direct-writing with lasers…………………………………...….….…11

1.2.2.1 Laser direct-write fabrication of microfluidic devices…………....12

1.2.2.2 Laser direct-write polymerization……………………………..…..14

1.2.3. Laser-induced near-field patterning…………………………….……21

1.3 Motivation and dissertation outline……………………………………..…28

II. DIRCT-WRITE MICROMACHINING OF POLYMETHYL-METHACRYLAT (PMMA) BY CO_2 LASER ABLATION...………..31

2.1 Mechanism of CO_2 laser processing PMMA…………………………..…..31

2.2 Experiment design and set up……………….…………………………...34

2.2.1 CO_2 laser system……………………………..…………….………..34

2.2.2 Experimental determination of threshold fluence…………….…….35

2.2.3 Chanel micromachining……………………………………………….36

2.3 Mathematical models of channel depth……………………………………37

2.4 Results and discussion……………………………………………………42

2.4.1 PMMA channel depth……………………………………………………42

2.4.2 PMMA channel profile…………………………………………………43

2.5 Summary and conclusions…………………………………………………44

III. DRICT-WRITE PHOTOPOLYMERIZATION USING A FREQUENCY-DOUBLED Nd:YAG LASER ………………………45

3.1 Mechanism of laser induced polymerization………………………………46

3.2 Hydrogel materials…………………………………………………………52

3.3 Experimental procedures……………………………………………………56

3.3.1 Materials and sample preparation………………………………………56

3.3.1.1 Materials…………………………………………………………………56

3.3.1.2 Sample preparation………………………………………………………57

3.3.2 Experimental setup and sample characterization…………………………58

3.3.2.1 Experimental setup………………………………………………………58

3.3.2.2 Sample characterization…………………………………………………60

3.4 Theoretical simulation of laser-induced direct-write polymerization………61

3.4.1 Simulation for the width and depth of laser induced polymerization..61

3.4.2 Monte Carlo method for single-shot exposure polymerization…………65

3.4.2.1 Photon packet generation………………………………………………70

3.4.2.2 Mean free path……………………………………………………………69

3.4.2.3 Photon packet scattering and weight update……………………………70

3.4.2.4 Photon packet termination………………………………………………71

3.5 Experimental results and discussion…………………………………………74

3.5.1 Experimental determination of materials parameters and model validation…………………………………………………………………………72

3.5.1.1 PETIA……………………………………………………………………72

3.5.1.2 PEG-DA (600)………………………..………………………..74

3.5.2 Direct-write fabrication of cellular structures in PETIA………..……...79

3.5.3 Direct-writing of biocompatible photocross- linkable hydrogel……..…85

3.6 Summary and Conclusions……………………………………..……..88

IV. DRECT LASER INTERFERENCE PATTERNING ….…..………..89

4.1 Interference Theory……………………………..……………..………90

4.2 Experimental procedure………………………..…………….………..94

4.2.1 Materials and sample preparation……………………….….………..94

4.2.1.1 Materials…………………………………………………..……...94

4.2.1.2 Sample preparation……………………………………..….…..96

4.2.2 Laser interference experimental setup and sample characterization……99

4.2.2.1 Experimental setup……………………………….………………99

4.2.2.2 Samples characterization…………………………..…………100

4.3 Results and discussion……………………………………..………...101

4.3.1 Laser interference pattering of PETIA…………………….…....101

4.3.2 2.5 and 3 dimensional laser interference patterning of SU-8……..…109

4.3.3 Laser interference nanopatterning of Shipley 1813………..……..113

4.4 Summary and Conclusions…………………………..………………114

V. LASER-INDUCED NEAR-FIELD PATTERINING …….…..........115

5.1 Nanosphere self-assembly……………………………….………….116

5.1.1 Theory of 2D self-assembly…………………………….…………116

5.1.2 Self-assembly methods…………………………………..…………119

5.1.2.1 Self-assembly nanospheres with spin-coating………..……...119

5.1.2.2 Self-assembly nanospheres by tilting method……….………120

5.1.2.3 Continuous convective self-assembly nanospheres…….……..120

5.1.3 Experimental results on nanospheres self-assembly……………….…...122

5.2 Mie theory of laser-microsphere interaction for nanoscale Surface Modification……………………………………………………………..…..126

5.3 Experimental procedure…………………………………………….….….132

5.3.1 Materials and sample preparation……………………………..……132

5.3.2 Laser-induced near-field pattering experimental setup and samples characterization…………………………………………….…….132

5.3.2.1 Experimental setup…………………………………………….…132

5.3.2.2 Sample characterization……………………………..………133

5.4 Results and discussion……………………………………..……...133

5.4.1 Single beam incidence laser-induced near-field pattering………..…..134

5.4.2 laser-induced near-field patterning with interference beam………..…137

5.5 Summary and Conclusions……………………………………..…..140

VI. CONCLUSIONS...…………………………………………..…...141

6.1 Direct-write laser micromaching of polymethyl methacrylate (PMMA) by CO_2 laser ablation…………………………………….……..…..141

6.1.1 Summary and conclusions……………………………………..……141

6.1.2 Scientific and Technical Contributions………………………..……142

6.2 Direct-write laser polymerization using frequency-doubled Nd:YAG laser…………………………………………………………..…...143

6.2.1 Summary and conclusion…………………………………….……..143

6.2.2 Scientific and Technical Contributions……………………….………143

6.3 Direct laser interference pattering……………………………….……144

6.3.1 Summary and conclusion…………………………………….…...144

6.3.2 Scientific and Technical Contributions………………….………..145

6.4 Laser-induced near-field pattering…………………………….………...145

6.4.1 Summary and conclusion………………………………….………...145

6.4.2 Scientific and Technical Contributions…………………….……..146

BIBLIOGRAPHY………………………………………….…………...147

LIST OF FIGURES

Figure

1.1 Contact, proximity and projection methods of photolithography. …………….………….4

1.2 The main processes in photolithography……………………………………..…………5

1.3 (i) Schematic illustration of the micro-moulding process, and (ii) SEM images of polymeric microstructures fabricated by micro-moulding [1]: A) patterned, isolated microstructures of PU on silver (one layer); B) isolated microcylinders of epoxy on 5-mm lines of epoxy supported on a glass slide (two layers); C) a continuous web of epoxy over a layer of 5-mm lines of epoxy supported on a glass slide (two layers); D) a three-layer structures on a glass slide made from a thermally curable epoxy………..…8

1.4 (a) Schematic illustration of the micro-printing process and (b) SEM image of gold features separated by narrow voids 35nm wide produced by micro contact printing technique……………………………………………………………………………..…8

1.5 (a) Schematic illustration of the micro-embossing process, which uses a mold to create a thickness contrast in a resist, and (b) SEM image of parallel lines generated in PMMA film by embossing with a rigid master……………………………………..…9

1.6 (a) Schematic illustration of the E-beam or Ion beam microfabrication process. (b) Suspended wires in 50-nm-thick silicon. The shortest wires are 7 μm long and the longest are 16 μm. The width of these wires is 200 and 120 nm for the left and right sets of wires, respectively………………………………......………………………11

1.7 Three-layered PMMA-microfluidic system for the detection of ammonia in aqueous samples. The system is supposed to mix the sample with three different reagents in sequence and then measure absorbance of a dye, which is the final product of the reaction sequence…………………………………………………………………...….13

1.8 Schematic illustration of microstereolithography process…………..…….….………..15

1.9 Schematic illustration of Integral microstereolithography. (a) LCD as pattern generator, and (b) DMD as pattern generator……………………………………………………….17

1.10 Optical system for Laser-induced two-photon absorption processs……….……........19

1.11 Two-photon microfabrication (a) Bull sculpture produced by two-photon microstereolithography (b) Laser-driven multi-degrees-of-freedom nanomanipulators produced by two-photon microstereolithography………………………........………20

1.12 (a) Schematic of the experimental setup, (b) irradiation of silica spheres on silicon from the top side, and (c) irradiation of silica spheres on glass from the bottom side…………………………………………………………………………………...22

1.13 SEM images of nanodent structures formed on a $Ge_2Sb_2Te_5$(GST) film under the removed particles after one laser pulse irradiation at different incidence angles of (a) a =0°, (b) a =30°, (c) a =45° and (d) a =60°, respectively. Laser fluence is 7.5 mJ/cm^2. Scale bar is 1.0 µm……………………………………………………….………..24

1.14 (a) Schematic illustration of the hexagonal interference patterning process. (b) SEM image of the negative photoresist columns created by hexagonal pattering. …............25

1.15 (a) Schematic set-up for the laser interference system with the optical elements: (1) lens; (2) beamsplitters; (3) mirrors; (4) sample. Note that the primary beam is divided into 3 sub-beams which are overlapped at the sample surface. (b), (c) and (d) are patterns in Fe and Al films. ……………………………………………………………26

1.16 Interference pattern created by two coherent beams. ………………………………..…27

2.1 Chemical structure of Poly (methyl methacrylate) (PMMA)………………... ………..32

2.2 Experimental system for PMMA channel fabrication. ………………….……………...34

2.3 Burn patterns in PMMA. The irradiation time t_s and laser power P for each spot (a) t_s= 0.12, P=0.46; (b) t_s= 0.08, P=0.73; (c) t_s= 0.07, P=0.98; (d) t_s= 0.1, P=0.73. …........…..35

2.4 Experiment design for CO_2 laser direct-writing…………………………….…………...36

2.5 Schematic diagram of PMMA channel and surface element……………………….………37

2.6 Channel depths as a function of laser power at different scanning speeds. The solid lines represent the theoretical fit. 1 : v=6.2mm/s, 2 : 8.6mm/s, 3: 11 mm/s, 4: 13.2 mm/s……………………………………………………………………………..…43

2.7 Modeling of PMMA channel profile. (a) P= 0.8W, v=8.6mm/s; (b) P= 0.98W, v=11mm/s……………………………………………………...……………………44

3.1 Schematic of Vinyl monomers. ………………………..…………….……………..47

3.2 Schematic of polymerization of multifunctional monomers……………………….……58

3.3 Chemical structures of materials that can be photopolymerized to create crosslinked hydrogel networks: (A) PEG diacrylate, methacrylate, and propylene fumarate derivatives, (B) Crosslinkable PVA derivatives, (C) Hyaluronic acid derivatives, (D) Dextranmeth-acrylate. ……………………………………………………..…………..55

3.4 Chemical structures of (a) Pentaerythritol triacrylate, (b) N-Methyldiethanolamine, (c) Eosin Y………………………………………………………………….…………….56

3.5 Chemical structures of photoinitiator system of PEG-DA hydrogel. …………….…..57

3.6 Schematic of 2-dimensional direct-writing experimental setup. …………….………..59

3.7 Schematic of 3-dimensional direct-writing experimental setup. ……………………..…60

3.8 Schematic view of single polymerization. ……………………..………………………..62

3.9 Schematic cure profile fabricated by a moving Gaussian laser beam. …………………65

3.10 Flow chart of the Monte Carlo simulation. ………………………..…………………..67

3.11 Schematic of the direction of input photon packet...…………………….………………69

3.12 Schematic diagram of experimental design for single exposed dots. ………..……......73

3.13 SEM pictures of single exposed dots for PETIA. ……..………………………………73

3.14 Experimentally measured working curve for PETIA at 532nm laser exposure. ……...74

3.15 Experimentally measured cure width vs. laser fluence for PETIA at 532nm laser exposure. ………..………………………………………………………………75

3.16 Monte Carlo simulation results (a) simulated polymerization with different input laser powers and exposure time, Laser input power and exposure time, from inside to outside: (1) 280 μw for 20 ms; (2) 400 μw for 50 ms; (3) 500μw for 60ms; (4) 720μw for 70ms. (b) Comparison of Monte Carol simulation results with experimental working curve..76

3.17 Schematic diagram of experimental design for PEG-DA……………………………… 77

3.18 SEM micrographs of PEG-DA block exposed by different energy density. (a) 100 J/cm^2 (b) 40 J/cm^2 (c) 18 J/cm^2 (d) 9 J/cm^2. ……………………………………..……...78

3.19 Experimentally measured working curve for PEG-DA (600) at 532nm laser exposure...79

3.20 Direct-write fabrication of square-cellular structures, wall width and period investigation: fabrication area: 300μmx300μm (a), (b) period: 25μm, wall width: 2μm; (c), (d) period: 10 μm, wall width: 2μm; (e) period: 8μm, wall width: 840nm. ……………………………………………………………………...…...81

3.21 Direct-write fabrication of square-cellular structures, wall height investigation: period: 10μm, area: 300μmx300μm (a) wall height: 0.8μm; (b) wall height: 1.5μm; (c) wall height: 2μm; (d) wall height: 2.5μm; (e) wall height: 4μm; (f) wall height: 7μm……………………………………………………………..…………..82

3.22 Comparison of cure line depth measurement results with experimental working curve ……………………………………………………………….…………………83

3.23 Comparison of cure line width measurement results with experimental working curve. 83

3.24 Direct-write fabrication of multiple-layer circular-cellular structures, laser power 70nw, scanning speed: 100μm/s…………………….……………………..…………. 85

3.25 Direct-write fabrication of biocompatible hydrogel square-cellular structures with input laser fluence of (a) 18J/cm^2; (b) 32 J/cm^2; (c)42 J/cm^2. ……………………….86

3.26 Direct - write fabrication of biocompatible hydrogel hexagonal honeycomb structures...87

3.27 Experimentally measured cure width vs. laser fluence for PEG-DA (600) at 532nm laser exposure. ………………………………………………………….……….……87

4.1 An input electric field of a wave……………………………………….….…………… 91

4.2 (a) line-like interference pattern resulting from (b) two laser beams; (c) hexagonal dot-like interference pattern from (d) three laser beams …………………..................93

4.3 Chemical structures for (a) pentaerythritol triacrylate (PETIA) and (b) N-methyl diethanolamine (N-MDEA). …………………………………………………….………94

4.4 SU-8 absorbance vs. film thickness. ………………………………………….…95

4.5 Chemical structure and Transmittance Spectrum of TINUVIN 384-2…………..……95

4.6 Chemical structure and absorption spectrum of TINUVIN 171…………...………... .96

4.7 Absorbance spectrum of Shipley 1813. …………………………….……….…..96

4.8 Spin speed vs. thickness curves for selected SU-8 resists. …………………….……..98

4.9 Spin speed vs. thickness curves for Shipley 1800 resists. …………….….………..99

4.10 Schematic set-up for the three beam laser interference system: (1) lens, (2) beam-splitters, (3) mirrors, (4) sample. Note that the primary beam is divided into 3 sub-beams which are overlapped at the sample surface…………………..………….….. 100

4.11 (a) Energy density per pulse and (b) Exposure Dose ($mJ.cm^{-2}$) necessary to photopolymerize the PETIA solution (with an interference pattern with period of 7.80 µm) as function of N-MDEA photoinitiator weight fraction. …………...……..102

4.12 (a) Line-like and (b, c) cross-like periodic patterns (period 7.8 µm) after development of the thicker PETIA layer. In (c), a macroscopic area with a cross-like structure is shown. The laser fluence (per pulse) was 244 $mJ.cm^{-2}$ and 10 laser pulses were used (scanning electron micrographs, tilt: 45°)……………………...… 104

4.13 Line-like periodic structures after development of the thin PETIA layers obtained using 5 laser pulses and (a) 174 , (b) 229, and (c) 210 $mJ.cm^{-2}$ of laser fluence (per pulse). Notice that the lines in (a) are isolated. The period in (a) and (b) was 7.80 µm while in (c) was 0.81 µm (scanning electron micrographs, Tilt: 30°)………105

4.14 (a) Cross- and honeycomb-like periodic structures after development of the PETIA solution. In (a, b and c), the period was 7.80 µm while in (d) was 15.12 µm. The lines in (c) indicate the direction of the interference pattern of both exposure processes. In (a), the sample was rotated 90° between the exposure procedures, while in (b, c and d) the angle was 45° (scanning electron micrographs, Tilt: 30°). The laser fluence (per pulse) in (a, b and c) was 244 $mJ.cm^{-2}$ while in (d) was 320 $mJ.cm^{-2}$…………………………………………………………………………....107

4.15 Two dimensional periodic structures fabricated using 3 laser beams with symmetrical configuration. For (a-d), the laser intensity of each individual laser

beam was the same ($E_{01} = E_{02} = E_{03}$), while for (e) and (f) different intensities were utilized. (a) 10 pulses, 176 mJ.cm^{-2}; (b) 3 pulses, 273 mJ.cm^{-2}; (c) 5 pulses, 273 mJ.cm^{-2}; (d) 10 pulses, 273 mJ.cm^{-2}; (e) $E_{02} = E_{03} = 1/3 \cdot E_{01}$; (f) $E_{02} = 2/3 \cdot E_{01}$; $E_{03} = 1/3 \cdot E_{01}$. The period of the structure was 4.8 µm. The inserts in (a), (e) and (f) correspond to the calculated intensity distributions of the interference patterns (scanning electron micrographs, Tilt: 30°)……………….……………………….. 108

4.16 Calculated cure depth (h) at three dosages level (E_{max}) for a symmetrical three beams interference pattern. (a) E_{max} = E; (b) E_{max} = 1.75 E; (c) E_{max} = 3.75 E………109

4.17 SEM images of line-like periodic structures after development of the thin SU-8 layer……………………………………………………………………….…………110

4.18 SEM images of 2.5D periodic structures patterned with SU-8……….………….. 111

4.19 3D periodic structures of SU-8 with 1.5% (w/w) absorber……………………….… 112

4.20 3D periodic structures of SU-8 with different percentage of absorber (a) 1% (w/w), (b) 2% (w/w), (c) 3% (w/w). ……………………………………….,……...……112

4.21 SEM images of nano periodic structures with Shipley 1813, period: 830nm, line width: 410 nm, patterning area: 1.5cm^2. ……………………..………………..….113

5.1 Two spheres partially immersed in a liquid layer on a horizontal solid substrate……117

5.2 Convective flux toward the ordered phase due to the water evaporation from the menisci between the particles in the 2D array. ……………………………………...119

5.3 Sketch of the particle and water fluxes in the vicinity of monolayer particle arrays growing on a substrate plate that is being withdrawn from a suspension………..…..121

5.4 Sketch of nanospheres self-assembly by tilting. …………………………….……122

5.5 Microscopy images of different parts of self-assembly nanospheres layer on glass substrate by tilting method, scale bar is 20 µm……………………..…………….…… 124

5.6 Microscopy images for the areas of interest on the glass substrate by spin-coating…125

5.7 SEM micrograph of the monolayer of silica spheres with a diameter of …..………..125

5.8 Schematic for particle scattering within the Mie theory. ………………………...…..126

5.9 The light intensity distributions on the surface under 800nm silica spheres. Three wavelength were used to simulate: 532nm, 355nm, and 266nm. …………...……….129

5.10 The light intensity distributions on the surface incident by 355nm laser under silica spheres with diameters of 800nm, 600nm and 430nm. …………………………...129

5.11 Schematic set-up for laser induced near-field patterning………………….………... 133

5.12 SEM images of cavity arrays formed after laser irradiation of 0.80 μm silica particles on a thin PEDOT film by a single laser pulse with a fluence of 70 mJ/cm^2..134

5.13 SEM images of cavity arrays formed at different sizes of nanospheres and the same laser fluences 80mJ/cm^2 (a) 800nm, (b) 600nm and (c) 430nm. ……….…………....135

5.14 SEM images of cavity arrays formed by different laser fluences with 800nm nanospheres, (a) 110 mJ/cm^2, (b) 84mJ/cm^2 and (c) 60mJ/cm^2. ………………...….136

5.15 SEM images of cavity arrays formed by different laser fluences with 600nm nanospheres, (a) 84 mJ/cm^2, (b) 70mJ/cm^2, (c) 56mJ/cm^2 and (d) 29mJ/cm^2. ……...136

5.16 SEM images of periodic cavity arrays formed after laser irradiation of 0.80 μm silica particles on a thin PEDOT film by two interfered laser beam with single pulse of fluence: 18 mJ/cm^2. …………………………………….………………..138

5.17 SEM images of periodic cavity arrays formed by different laser fluences with 800 nm nanospheres, (a) 52mJ/cm^2, (b) 38mJ/cm^2, (c) 18mJ/cm^2, (d) 6mJ/cm^2……….. 139

5.18 SEM images of periodic cavity arrays formed by different laser fluences with 430 nm nanospheres, (a) 110 mJ/cm^2, (b) 92mJ/cm^2, (c) 76mJ/cm^2, (d) 47mJ/cm^2……..139

LIST OF TABLES

Table

1.1 Characteristics of vector-by-vector microstereolithography machines………………..…17

1.2 Characteristics of the integral microstereolithography machines…………..…………18

2.1 Threshold fluence of PMMA……………………………………...….…………..37

4.1 Calculated processing times to fabricate different periodic arrays using LIP and DLW...94

ABSTRACT

The ability to generate small structures is central to modern science and technology. Laser direct-write microfabrication and micropatterning are general terms that encompass modification, subtraction, and addition processes capable of creating patterns of materials directly on substrates without the need for lithography or masks. In this work, four laser direct-write microfabrication and micropatterning techniques were studied:

(a) CO_2 laser micromachining provides a flexible and low cost means for the manufacture and rapid prototyping of miniaturized polymer systems such as PMMA microfluidic chip devices. In this work the relationship between the profile and depth of laser-ablated channels, laser power and scanning velocity is investigated. This work mainly focused on low laser power which can reduce the cost of the fabrication system, and low scanning speeds to obtain narrow channels. The laser power used for channel fabrication ranged from 0.45W to 1.35W and the scanning speeds ranged from 2mm/s to 14mm/s. The width and the depth of channels ranged from 44μm to 240 μm and 22μm to 130μm respectively. Physical models were developed for the depth and channel profile of ablated channels. This work incorporates the threshold fluence for CO_2 laser ablation of PMMA into the model to accurately predict the profile of the channel. The models are in excellent agreement with experimental results, with a maximum deviation of approximately 5%.

(b) A sub-micrometer resolution laser direct-write polymerization technique for creating two-dimensional and three-dimensional structures was developed using a

frequency-doubled Nd:YAG laser. Functional patterns were directly fabricated in photocurable monomers and hydrogels via a layer-by-layer fabrication approach. Experimental studies and Monte Carlo simulations were conducted to understand the detailed microscale optical scattering, chemical reaction, polymerization, and their influence on critical fabrication parameters. The experimental data are in good agreement with the theoretical model.

(c) Direct laser interference is a good method for rapid and large area fabrication of two-dimensional and three-dimensional periodic structures on photopolymerizable materials. In this work, different aspects of the direct laser interference method were studied. A fabrication system using a frequency-tripled Nd:YAG laser with 10ns pulses and an optical delivery system was developed. Three different photopolymerizable materials were investigated: (1) pentaerythritol triacrylate (PETIA) with photoinitiator N-methyldiethanolamine (N-MDEA) was used to study the effect of photoinitiator concentration for line-, cross-, honeycomb- and dot-like structures; (2) SU-8 with absorber TINUVIN 384-2 was used to investigate three-dimensional patterning; (3) Shipley 1813 was used to achieve patterns with submicron period.

(d) A new approach to fabricating nanometer sized cavity arrays on Poly(3,4-ethylene dioxythiophene)-poly(styrenesulfonate) (PEDOT-PSS) thin films using laser-assisted near-field pattering was investigated. Periodic nano-cavity arrays were patterned by combining direct laser interference technology and laser induced near-field technology. An analytical model based on Mie theory was developed, the predicted intensity distributions on the substrate indicate a strong near-field enhancement confined to a very small area (nanometer scale).

CHAPTER I

INTRODUCTION

Currently, the development of products at the micro- and nanoscale is receiving considerable attention worldwide due to expected benefits in properties and performance. Micro- and nanotechnology are seen as the next steps in the industrial revolution and requires manufacturing processes that will revolutionize the way we exist. The challenges for engineers and scientists are manifest in the construction of products at small scales. The future of micro- and nano-science and technology depends critically on the availability of versatile techniques for micro- and nano-fabrication.

As fabrication of microstructures grows in importance in a wide range of areas, from microelectronics through optics, microanalysis, combinatorial synthesis, display, and MEMS to cell biology, the utility of microfabrication and micropatterning methods certainly increase. In the last several years, various different techniques for the fabrication of micro- and nano-functional devices have emerged. These techniques can be principally divided into two groups: (1) Microfabrication and micropatterning by replication, and (2) maskless or masterless microfabrication.

The first group can also be divided into two sub-categories: (a) Replication with a mask, to which all versions of photolithography belong. Here, the key component is a photomask that consists of alternating regions of opaque and transparent features to

modulate the intensity of light impinging on a photoresist film. (b) Replication with a master, which includes micro-moulding [1, 2], micro-embossing [3] and micro-contact printing [4].

The second group includes direct-writing with a rigid stylus [5] or energetic particles [6-11], self-assembly nanosphere lithography [12], and laser interference lithography [13-15].

This chapter intends to provide a general and methodological review of the various techniques for microfabrication and micropatterning. I do not aim to cover in depth all the technical details of these techniques. The focus of this chapter is to illustrate the different operational and mechanistic principles involved in these microfabrication and patterning techniques, and show the necessity for and value of this doctoral dissertation.

1.1 Microfabrication and micropatterning via replication

1.1.1 Photolithography

Photolithography, literally meaning light-stone-writing in Greek, is the process by which patterns on a semiconductor material can be defined using light. It is the means by which the small-scale features of integrated circuits are created. The steps involved in the photolithographic process are wafer cleaning; barrier layer formation; photoresist application; soft baking; mask alignment; exposure and development; and hard-baking.

Before the resist is applied to the substrate, the surface is cleaned to remove any traces of contamination from the surface of the wafer such as dust, organic, ionic and metallic compounds and a layer of silicon dioxide is formed by a wet or dry oxidation process. The cleaned wafer is subject to priming, to aid the adhesion of the resist to the

surface of the substrate material [16].

A resist is applied to the surface using a spin-coating machine. This device holds a semiconductor wafer, using a vacuum, and spins it at high-speed (3000-6000 rpm) for a period of 15-30 seconds. A small quantity resist is dispensed in the centre of the spinning wafer. The rotation causes the resist to be spread across the surface of the wafer with excess resist being thrown off. Close to the centre of the wafer, the variation in the thickness of resist is around 30 nm. Preparation of the resist is concluded by a pre-bake, where the wafer is gently heated in a convection oven and then on a hotplate to evaporate the resist solvent and to partially solidify the resist.

The photomask is created by a photographic process and developed onto a glass substrate. The cheapest masks use ordinary photographic emulsion on soda lime glass, while chrome-on-quartz glass is used for high-resolution deep UV lithography. In-plane as well as rotational alignment of the mask is critical and must be achieved prior to exposure. Industrial photolithography machines use automatic pattern recognition to achieve the registration alignment. Depending on the design of the photolithography machine, the mask may be in contact with the surface, very close to the surface, or used to project the pattern onto the surface of the substrate through optical elements. These methods are called, contact, proximity and projection lithography respectively. Figure 1.1 shows a schematic diagram of these methods. The projection system is the most complex method but does mean the projection of the mask can be scaled.

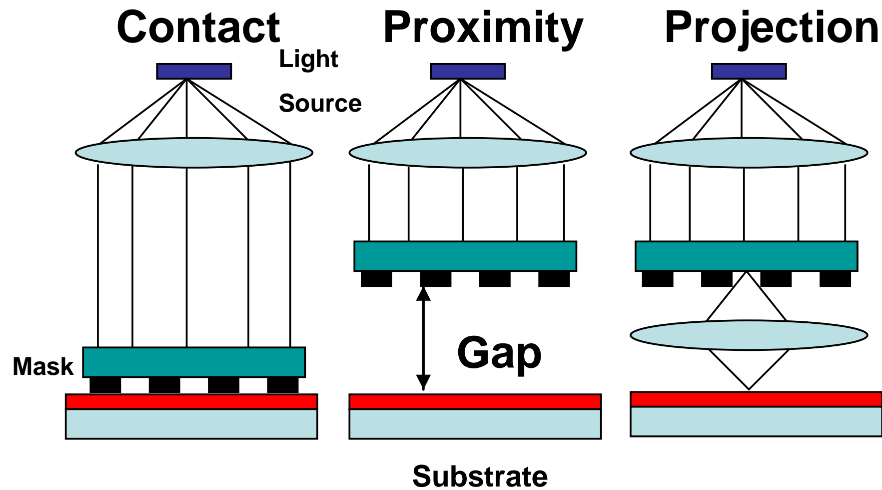

Figure 1.1 Contact, proximity and projection methods of photolithography.

During the exposure process, the resist undergoes a chemical reaction. Depending on the chemical composition of the resist, it can react in one of two possible ways when the light strikes the surface. The action of light on a positive resist causes it to become polymerized where it has been exposed to the light. A negative resist has the reverse property. Exposure to UV-light causes the resist to decompose. After the developing process, a negative of the mask remains as a pattern of resist. Although not necessary for all processing, to further harden the resist and remove any residue of the developer, the wafer undergoes a post-bake process. During this process, the resist temperature can be controlled to cause a plastic flow of the resist which can be desirable for tailoring sidewall angles. After either deposition of semiconductor layers or metal, or etching down to selectively remove parts of the SiO_2, the resist can be removed. For positive photoresists, acetone, trichloroethylene, and phenol-based strippers may be used, while negative resists are generally removed using Methyl Ethyl Ketone (MEK) or Methyl Isobutyl Ketone (MIBK). Figure 1.2, shows the process schematically using a proximity mask.

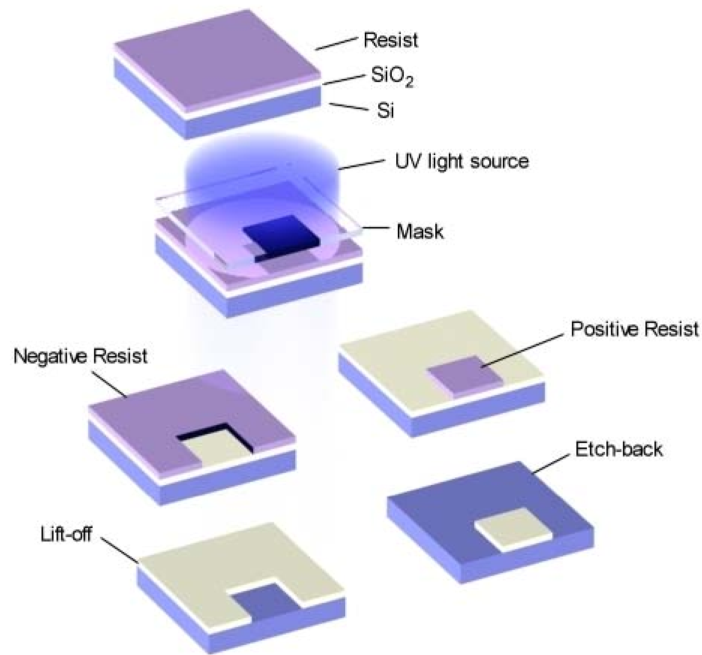

Figure 1.2 The main processes in photolithography.

The ability to project a clear image of a small feature onto the wafer is limited by the wavelength of the light that is used, and the ability of the reduction lens system to capture enough diffraction orders from the illuminated mask. Current state-of-the-art photolithography tools use deep ultraviolet (DUV) light with wavelengths of 248 and 193 nm, which allow minimum feature sizes down to 50 nm.

The minimum feature size that a projection system can print is given approximately by [17]:

$$\mathrm{F} = \kappa \cdot \frac{\lambda}{NA} \tag{1.1}$$

where F is the minimum feature size (also called the target design rule), κ is a coefficient that encapsulates process-related factors, and typically equals 0.5, λ is the wavelength of light used, and NA is the numerical aperture of the lens as seen from the wafer. It is also

common to write F as 2 times the half-pitch.

According to equation (1.1), minimum feature sizes can be decreased by decreasing the wavelength, and increasing the numerical aperture, i.e. making lenses larger and bringing them closer to the wafer. However, this design method runs into a competing constraint. In modern systems, the depth of focus D_F is also a concern:

$$D_F = 0.6 \cdot \frac{\lambda}{NA^2} \tag{1.2}$$

The depth of focus restricts the thickness of the photoresist and the depth of the topography on the wafer. Chemical mechanical polishing is often used to flatten topography before high-resolution lithographic steps.

1.1.2 Micro-moulding, micro-embossing, and micro-contact printing

Moulding, embossing and printing are age-old techniques that have recently been given new twists by microtechnologies. The printing industry depends on stamping the inked typeface against paper for transferring the ink. The very same process has now been adopted in microfabrication, with sophisticated tools and materials for plastics and ceramics that can be extended to novel applications by microfabrication techniques.

In a moulding process, structures are formed inside the void spaces of a master or mould, as shown in figure 1.3. The traditional method of casting is still in use in microfabrication: thick polymethyl methacrylate (PMMA) resist and polydimethyl siloxane (PDMS) elastomers are cast. But micro-moulding includes various transport and deposition processes: injection of thermoplastics, electroplating of metals, CVD of polysilicon or diamond or sol-gel of PZT. With the use of an appropriate material, the shape, structure, and pattern of the mould can all be transferred into the replica with high

fidelity and accuracy, even on the nanometer length scale. This technique also allows the duplication of 3D structures in a single step [18]. Micro-moulding requires at least three steps to complete [1, 2]: 1) the voids on a mould are filled with a polymer precursor; 2) the excess material is removed; and 3) the mould is placed on the desired substrate. After curing the prepolymer, the mould is peeled off leaving behind the replicated structures on the substrate. An important advantage of micro-moulding is its capability to generate complex patterns in a layer-by-layer fashion and on non-planar or curved surfaces, which often is a prerequisite for building 3D microstructures.

Printing is an efficient method for pattern transfer [19], as shown in figure 1.4. A conformal contact between the stamp and the surface of the substrate is the key to its success. Printing has the advantage of simplicity and convenience: Once the stamp is available, multiple copies of the pattern can be produced using straightforward experimental techniques. Printing is an additive process; the waste of material is minimized. Printing also has the potential to be used for patterning large areas. Although contact printing is most suitable for two-dimensional fabrication, it has also been used to generate quasi-three- dimensional structures through combination with other processes such as metal plating [20].

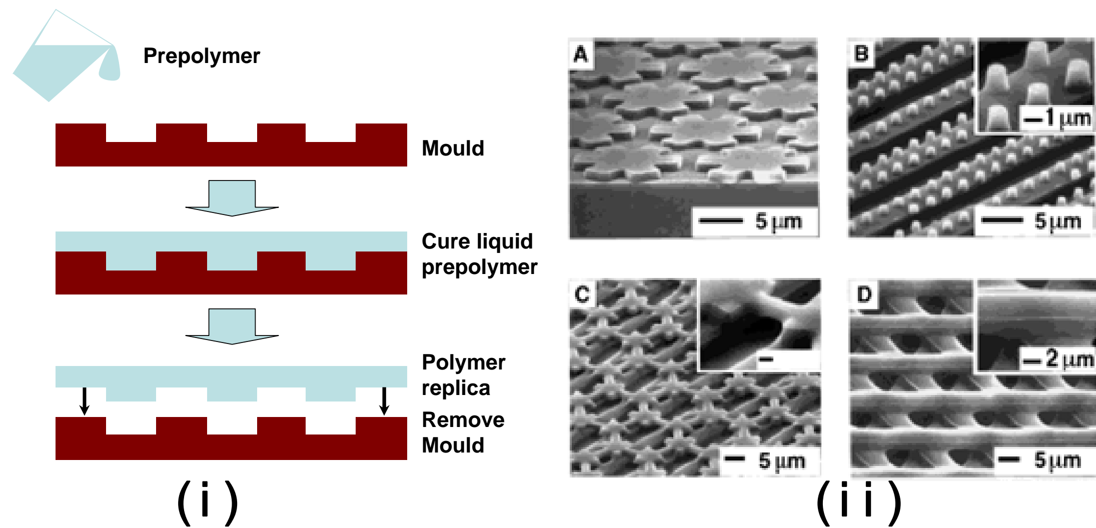

Figure 1.3 (i) Schematic illustration of the micro-moulding process, and (ii) SEM images of polymeric microstructures fabricated by micro-moulding [1]: A) patterned, isolated microstructures of PU on silver (one layer); B) isolated microcylinders of epoxy on 5-µm lines of epoxy supported on a glass slide (two layers); C) a continuous web of epoxy over a layer of 5-µm lines of epoxy supported on a glass slide (two layers); D) a three-layer structures on a glass slide made from a thermally curable epoxy [2].

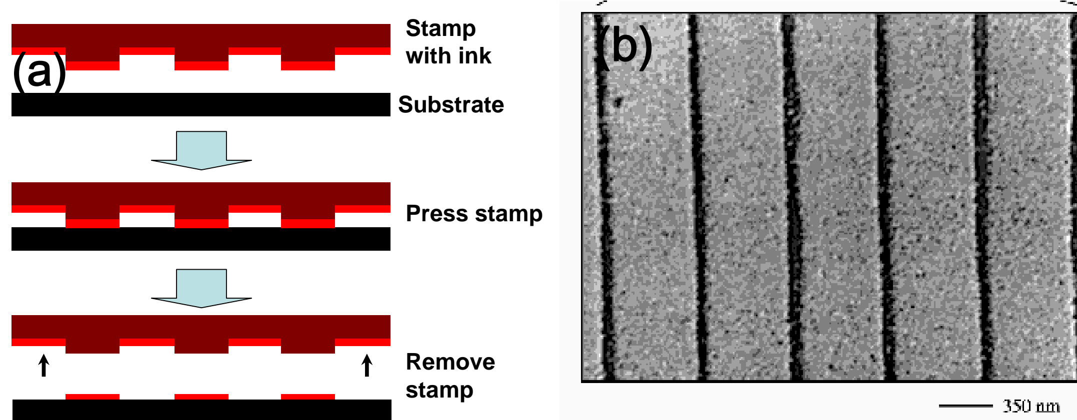

Figure 1.4 (a) Schematic illustration of the micro-printing process and (b) SEM image of gold features separated by narrow voids 35nm wide produced by micro contact printing technique [4].

Embossing is a simple and convenient technique that generates relief patterns in a polymer by mechanical deformation using a rigid master, as shown in figure 1.5 [3]. The polymer must be either thermoplastic, UV- or thermally curable, or deformable to adapt the shape of the patterns on the master. In most cases, residual films of the polymer

remain in the compressed areas, which can be removed using a dry etching process [21, 22]. The resolution of structures that can be generated using this technique is mainly determined by the mechanical stability of the master, the properties of the polymer and the dimensional change of the embossed structures with temperature or pressure. Experimental results indicate that features with critical dimensions well below 10nm are achievable without modifying the procedure significantly [23].

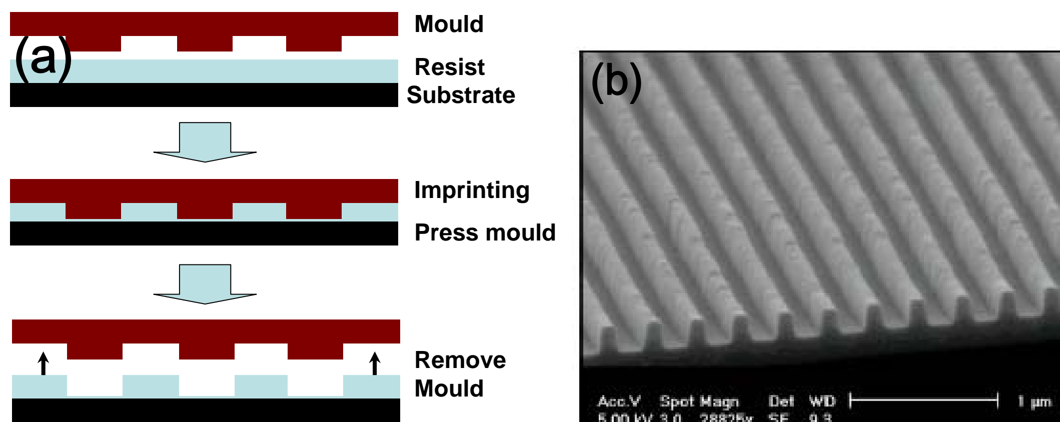

Figure 1.5 (a) Schematic illustration of the micro-embossing process, which uses a mold to create a thickness contrast in a resist, and (b) SEM image of parallel lines generated in PMMA film by embossing with a rigid master [3].

1.2 Maskless microfabrication and micropatterning

1.2.1 Direct-writing with a beam of energetic particles

Focused beams of energetic particles comprising electrons, ions, and electrically neutral metastable atoms provide means for generating patterns in a proper resist material [6-11], as shown in figure 1.6.

These techniques have extremely high resolution capabilities because of their short wavelengths (<0.1nm) combined with a large depth of focus. Electron-beam (e-beam)

lithography is a feature that can be readily added to most conventional scanning electron microscopy (SEM) systems. Although high throughput continues to be a major challenge for this technique, e-beam lithography has become a standard tool for writing arbitrary patterns for many technological and scientific applications. A variety of materials have been demonstrated for use with e-beam lithography, including polymers [24-27], inorganic materials [28], and self-assembled monolayers or SAMs [29]. Reactions that are thereby induced depend on the chemical composition of the resist. For polymers, they can include polymerization, crosslinking, local chain scission, or a more complex processes such as chemical amplification involving acids or bases [30]. The practical resolution of this technique is mainly determined by the spot size of the beam, and several other factors such as scattering effects and the generation of secondary electrons. Poly(methyl methacrylate) (PMMA) remains a classical resist for e-beam lithography, and much work continues to be done with this polymer despite extensive technological advances and development in e-beam lithography, and the large number of resist formulations that have been developed. Direct etching induced by an e-beam is possible, but generally requires higher doses, which limits its practical utilization.

Techniques using focused ion beams (FIBs) are conceptually related to e-beam lithography [31]. In principle, the higher mass of ions may result in patterning capabilities that are less prone to distortions due to back-scattering from the substrate. Other advantages include the possibility of highly localized implantation doping (the formation of a new material or a new phase under the surface of a substrate), ion-induced deposition, and the capability of removing material from a surface using ion milling or ion-beam assisted etching. Until now, high-resolution variants of these techniques remain

in a relatively less-developed state than e-beam writing.

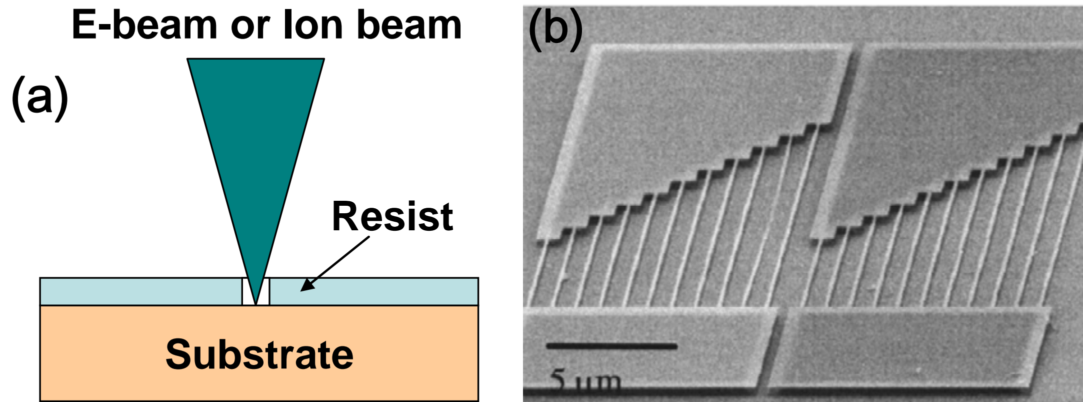

Figure 1.6 (a) Schematic illustration of the E-beam or Ion beam microfabrication process. (b) Suspended wires in 50-nm-thick silicon. The shortest wires are 7 μm long and the longest are 16 μm. The width of these wires is 200 and 120 nm for the left and right sets of wires, respectively [31].

1.2.2 Direct-writing with lasers

Laser direct-write and patterning are general terms that encompass modification, subtraction, and addition processes capable of creating patterns of materials directly on substrates without the need for lithography or masks. Given a laser source, one can either fix the location of the beam and raster the substrate using motion-control stages, fix the substrate and raster the beam using mirrors, or use a combination of both. For laser direct-write modification (LDWM) or subtraction (LDW-), the material of interest is directly irradiated and is either removed (laser micromachining) or modified (melting, sintering, and so on). In both cases, either pulsed or CW lasers can be effective. Laser direct-write and patterning is of paramount importance in many areas of modern science and technology, with applications ranging from the production of integrated circuits, information storage devices, and display units to the fabrication of micro-electromechanical systems (MEMS), miniaturized sensors, microfluidic devices, biochips,

photonic bandgap crystals, micro-optical components, and diffractive optical elements [12, 32-40].

1.2.2.1 Laser direct-write fabrication of microfluidic devices

Microfluidic devices, which are used to manipulate liquids and gases in channels having cross-sectional dimensions on the order of 10-500µm, find increasing applications as analytical systems, biomedical devices, tools for chemistry and biochemistry, and as systems for fundamental research [41-45] . Most prototype devices to date have been fabricated in glass, silica, or silicon-based substrates by conventional lithography. To fabricate such devices, highly resistant masks are needed, which raises the cost of the fabrication and extends the production cycle. Although successful cell-patterning and microfluidic chips [46] have been prepared using silica- or silicon-based substrates, the associated fabrication techniques, including channel fabrication and sealing, are generally difficult and expensive to implement.

Polymer substrates are promising alternatives for microfluidic devices. Industrial interest in utilizing plastics for the production of microanalytical systems is primarily driven by the fact that these materials are less expensive and easier to manipulate than silica-based or glass substrates. A wide variety of low-cost polymer materials enable their selection for thermal and chemical resistance, molding temperature, and surface derivation properties [47].

A large number of polymer microfabrication technologies have been established over recent years. These technologies can roughly be divided into two groups: replication techniques [48, 49], in which a master structure is replicated into the polymer material; and the direct techniques [50-52], in which each single device is manufactured separately.

Replication methods such as hot embossing and injection molding are not only complex but also expensive compared with laser ablation. Laser direct-write is an attractive technique for the fabrication of microfluidic devices. No mask is necessary and redeposition problems may be widely reduced. A number of groups have investigated laser ablation on polymers [53, 54] for applications such as multimode lightguides and microfuel cells [46, 55]. Klank et al [56, 57] investigated the usage of a commercial CO_2 laser system for PMMA microfluidic systems fabrication and a three-layered microfluidic device made by them is shown in figure 1.7. The laser power they used ranged from 10W to 60W; scanning speed ranged from 80mm/s to 400mm/s and the typical width of the channel was 250 μm. They derived a least squares fit model through their experimental data. Modest [58] developed a three dimensional conduction model based on the finite difference method. There are series of works for CO_2 laser cutting and drilling of PMMA with even higher laser power [59, 60].

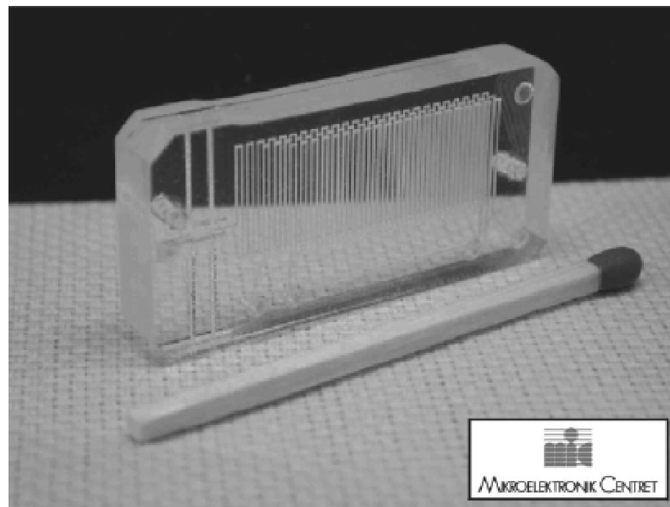

Figure 1.7 Three-layered PMMA-microfluidic system for the detection of ammonia in aqueous samples. The system is supposed to mix the sample with three different reagents in sequence and then measure absorbance of a dye, which is the final product of the reaction sequence [32].

1.2.2.2 Laser direct-write polymerization

Laser direct-write polymerization is also known as stereolithography process, which was invented and patented by Dr. Charles Hull in the 1980s. In the 1986 patent publication for the very first SLA patent, the process is described as follows: "Stereolithography is a method and apparatus for making solid objects by successively "printing" thin layers of a curable material, e.g., a UV curable material, one on top of the other. A programmed movable spot beam of UV light shining on a surface or layer of UV curable liquid is used to form a solid cross-section of the object at the surface of the liquid. The object is then moved, in a programmed manner, away from the liquid surface by the thickness of one layer, and the next cross-section is then formed and adhered to the immediately preceding layer defining the object. This process is continued until the entire object is formed".

In recent years, there has been increasing interest in using rapid prototyped parts as functional prototypes rather than just visual aids. According to the 2006 Wohlers Report on Rapid Prototyping, more than 20% of rapid prototyped parts are being used as functional prototypes. This means that more accurate parts with smaller features need to be built using stereolithography machines. In addition, MEMS and other Micro-manufacturing industries see stereolithography as a way of obtaining parts in addition to silicon-based micro-manufacturing techniques. MEMS devices cannot be built using traditional stereolithography machines, because the smallest feature that can be built using these machines is around 60μm, while operating in the high resolution mode.

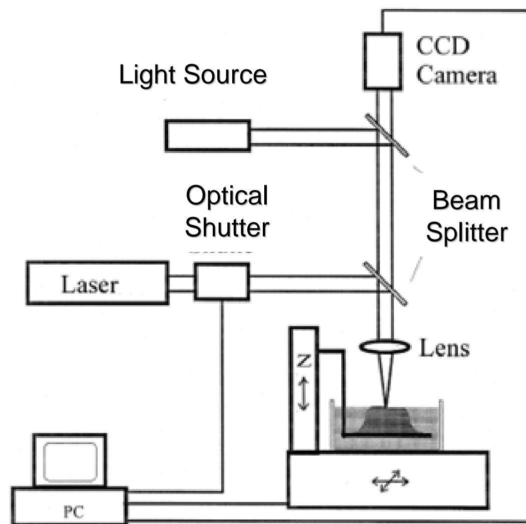

Figure 1.8 Schematic illustration of microstereolithography process.

Microstereolithography is the general designation of various microfabrication technologies based on the principle used in stereolithography as shown in figure 1.8. All microstereolithography machines have the same aim and the same basic principle: They allow building small-size, high-resolution three-dimensional objects, by superimposing a certain number of layers obtained by a light-induced and space-resolved polymerization of a liquid resin into a solid polymer.

Photopolymerization is the chemical reaction underlying the change of state that makes it possible to create the layers composing the objects in the stereolithography process: the absorption of a given quantity of photons per unit volume of photosensitive medium creates reactive species, which induces the polymerization of the liquid monomer into a solid polymer by a chain reaction. This polymer is generally cross-linked and cannot dissolve again in a monomer bath.

The evolution of the polymerized depth with the irradiation time in stereolithography can be easily predicted and is presented extensively in the literature

[61]. Equation 1.3 gives the temporal evolution of the polymerized depth:

$$e = \frac{1}{\alpha c} \ln\left(\frac{t}{t_0}\right) \tag{1.3}$$

Where, t (s) is the irradiation time, t_0 (s) the irradiation time at the threshold, α ($l \cdot mol^{-1} \cdot cm^{-1}$) the Napierian coefficient of molar extinction, c ($mol \cdot l^{-1}$) the concentration of the absorbing substance. This relation shows that the evolution of the polymerized depth e with the irradiation time is logarithmic. This simple model is in good agreement with experimental results in the case of resins that do not undergo changes in their absorption coefficient during the polymerization process.

Presently, there are two major types of microstereolithography: vector-by-vector microstereolithography and integral microstereolithography. The basic principle of all vector-by-vector microstereolithography machines is very similar to that of the stereolithography technique shown in figure 1.8: every layer of the object is made by scanning a focused light beam on the surface of a photosensitive resin. To get a better resolution than stereolithography, the beam is focused more precisely in order to reduce the spot size to a few micrometers in diameter, requiring additional technological developments in the designed microstereolithography machines. In particular, it is necessary to measure precisely and continuously the position of the surface on which the beam is scanned and to dynamically focus it with a sufficient precision. Table 1.1 presents a summary of microstereolithography demonstrations in the literature.

Research team	Light source	Irradiation	Component size	Resolution
Takagi et al. [62]	He-Cd laser, UV (325 nm)	From below	20x20x20mm^3	5 x 5 x 3 μm (x,y,z)
Ikuta et al. [63]	Xenon lamp, UV	From above	10x10x10mm^3	60μm, up to 8μm
Zissi et al. [61]	Argon ion laser	From above	Not reported	30x 30x 20 μm (x,y,z)
Zhang et al. [64]	Argon ion laser	From above	Not reported	Spots of 1-2 μm

Table 1.1 Characteristics of vector-by-vector microstereolithography machines

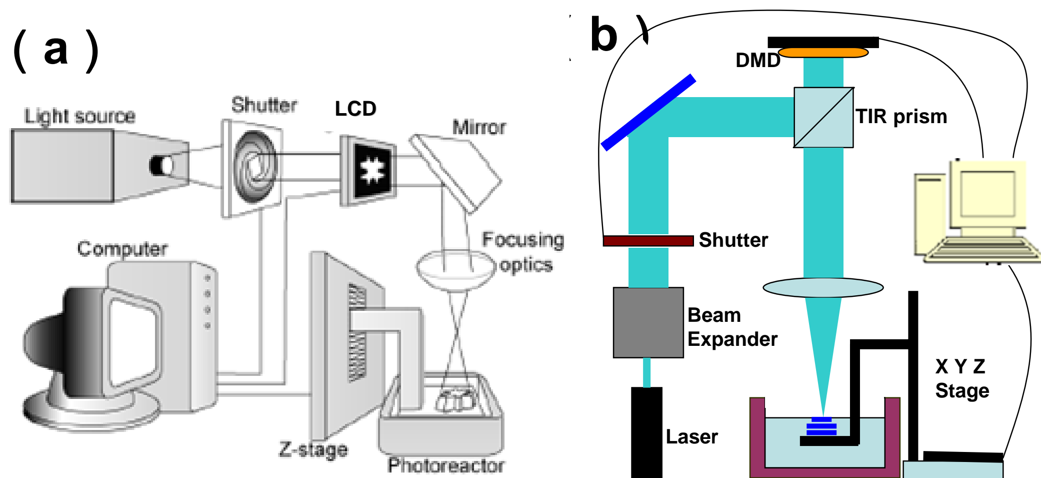

Figure 1.9 Schematic illustration of Integral microstereolithography. (a) LCD as pattern generator [65], and (b) DMD as pattern generator.

In integral microstereolithography, every layer of the object is made in one irradiation step by projecting its image on the surface of the photopolymerizable resin with a high resolution at a certain depth of focus. This avoids the problems related to the fine focusing of a light beam in one point on the liquid surface, which often limits vector-by-vector microstereolithography processes. A pattern generator allows shaping the light, such that it contains the image of the layer to be solidified. This image is then reduced

and focused on the surface of the reactive medium with the appropriate optical system. The superimposition of the different layers composing the object is done in the same way as in conventional stereolithography. Integral microstereolithography processes are fast, because the irradiation of an entire layer is done in one step, whatever its pattern may be. There are two popular pattern generators: a) Liquid crystal displays (LCDs), and b) Digital Micromirror Device™ as shown in figure 1.9. Different embodiments of integral microstereolithography reported in the literature are presented in Table 1.2.

Research team	Light source	pattern generators	Component size	Resolution
Bertsch et al. [66]	Ar+ laser (515nm)	LCD	6x8x15mm^3	5 x 5 x 5 µm (x,y,z)
Chatwin et al. [67]	Ar+ laser (351.1nm)	LCD	Not reported	50µm in Z
Loubère et al. [68]	Halogen lamp	LCD	3x2.4x15mm^3	5 x 5 x 10 µm
Zhang et al. [64]	Argon ion laser	LCD	Not reported	Spot has 1-2 µm
Bertsch et al. [65]	Argon Ion laser	DMD	6x8x15mm^3	5 x 5 x 5 µm
Bertsch et al. [65]	Argon Ion laser	DMD	10.24x7.68x20mm^3	10x 10x 10µm
Zhang et al. [69]	Argon ion laser	DMD	Not reported	5 x 5 x 10 µm

Table 1.2 Characteristics of the integral microstereolithography machines

There are, of course, many advantages to creating the object directly in the resin, without superimposing layers: No support parts are needed. No time is spent spreading the liquid on the part being manufactured, which potentially can speed-up the process significantly. Freely movable structures can be fabricated without the need of sacrificial layers. Many attempts have been made to develop such processes in the rapid prototyping domain for creating large objects, but they have never been successful. However, when making small objects, one solution has been found to create them directly inside the

reactive medium using two-photon absorption, as shown in figure 1.10.

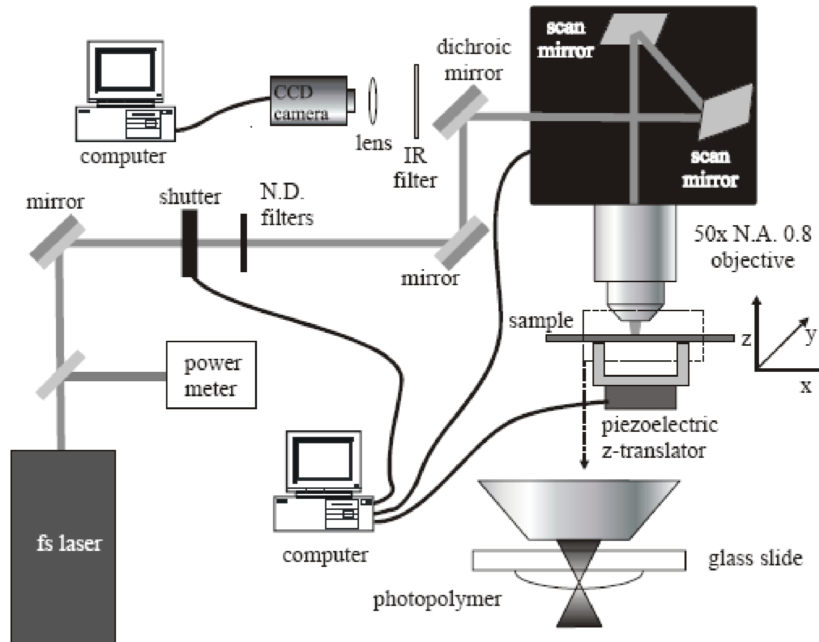

Figure 1.10 Optical system for Laser-induced two-photon absorption processs [70].

Two-photon absorption is a nonlinear optical phenomenon that occurs at sufficiently high level of irradiance in all materials, when the combined energy of two photons matches the transition energy between the ground state and the excited state of the absorbing medium. The rate of two-photon absorption is proportional to the square of the incident light intensity. The quadratic dependence of the two-photon absorption rate on the light intensity confines the absorption to the area at the focal point. As the two-photon transition rate is extremely small, the power of the light source has to be extremely high. Such high power light sources can be achieved through ultrafast lasers. In this technique, photopolymerization occurs only in the vicinity of the focal point of a laser beam thus generating a voxel, which is a 3D volume element of solidified resist. The patterning procedure is performed by pinpoint-scanning a focused laser according to a pre-

programmed pattern design in the form of a voxel matrix. The dimensions of such a voxel are mainly determined by the spot size and pulse energy of the laser beam, and can go beyond the limit of Rayleigh diffraction [70]. The voxel dimension can also be reduced to further improve the spatial resolution of resultant structures when nonlinear processes are incorporated into the photochemical reactions. Figure 1.11 (a) shows scanning electron micrographs of 'micro-bull' sculptures [71] fabricated via two-photon absorption polymerization. These 10-μm-long, 7-μm-high bulls are the smallest model animals ever made artificially, and are about the size of a red blood cell. The tiny volume attainable for such micromachines would allow them to be transported to locations inside the human body through even the smallest blood vessels, for example to deliver clinical treatments. To depict the tiny features of the microbulls, a fabrication accuracy of about 150 nm was needed. The nanotweezers shown in figure 1.11(b) have probe tips measuring only 1.8 μm in length and 250 nm in diameter. The nanotweezers can be driven by a focused laser beam [72].

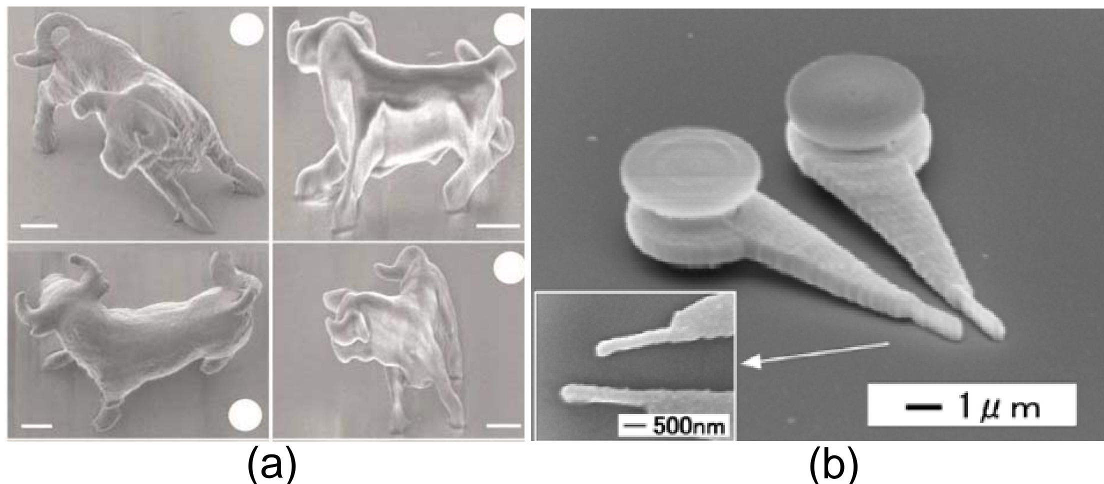

Figure 1.11 Two-photon microfabrication (a) Bull sculpture produced by two-photon micro-stereolithography [71] (b) Laser-driven multi-degrees-of-freedom nanomanipulators produced by two-photon microstereolithography[72, 73].

1.2.3. Laser-induced near-field patterning

Fabrication technology on the nanometer scale has attracted much attention in the last decade due to the industrial demand for smaller and smaller structures, such as quantum devices and extremely high-density recording media. As a result, structuring techniques such as lithography [27] and field ion beam patterning [74] have been investigated for nanofabrication. However, most of these techniques are limited either by their inability for large-area fabrication or by the diffraction limit and in most cases the high manufacturing costs. To overcome the diffraction barrier and to spatially control matter on a nanometer scale, a variety of nanofabrication techniques employing optical near fields has been proposed.

Laser-induced near-field patterning of surfaces at a resolution below the diffraction limit has attracted more and more attention in recent years due to its extensive potential application in high-density data storage and high-resolution optical lithography for nanodevice fabrication [75]. If the aperture-to-medium separation is controlled at a distance much smaller than the wavelength, the resolution will be determined by the aperture size instead of the diffraction limit [76]. This technique is used in the scanning near-field optical microscope (SNOM) system: a single hollow optical fiber with a small aperture at its end is used to deliver the laser beam [77]. Due to the near-field optical enhancement effect at the tip, the SNOM system is able to perform nanoscale surface modification of different kinds of materials. However, this approach is difficult to implement in an industrial application due to sophisticated hardware needed to control the near-field distance and the low throughout. One promising approach that could lead to massively parallel nanostructuring was demonstrated by using a particle-mask to pattern

a solid substrate [28, 78]. The technique employs a regular two-dimensional (2D) array of microspheres/nanospheres to focus the incident laser radiation onto the substrate. It permits single step surface patterning of thousands or millions of sub-microm cavities or holes on the substrate with a single or a few laser pulses. The energy conversion efficiency by particle microlens/nanolens is close to 100%, which is significantly higher than that in SNOM system (10^{-4}-10^{-5}) [75].

The accidental discovery of particle-induced damage during dry laser cleaning of irregularly shaped Al_2O_3 particles on glass [79] has led to this exciting yet simple technique. Nanosphere-based fabrication induced by the optical near-field was also employed for patterning a urethane-urea copolymer containing a push-pull type azobenzene. In this kind of polymer, the surface deformation is attributed to the gradient force of the optical near-field [80].

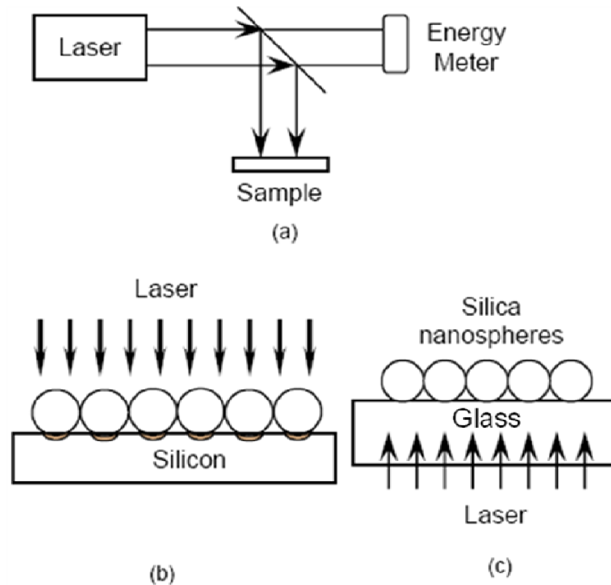

Figure 1.12 (a) Schematic of the experimental setup, (b) irradiation of silica spheres on silicon from the top side, and (c) irradiation of silica spheres on glass from the bottom side.

A schematic of laser-induced near-field patterning with self-assembled micro/nanospheres is shown in figure 1.12. When the laser beam is incident on the top surface of spheres, there is a field enhancement at the interface between the sphere and the substrate. This optical field enhancement by nanospheres can be explained by Rayleigh and Mie scattering theories [81]. Rayleigh scattering takes place when the diameter of the sphere is less than the wavelength of the light. In this case, the sphere is treated as a dipole radiator and the electric field enhancement is at its sides along the direction of polarization of the incident light and there is hardly any focusing. In contrast, when the diameter of the sphere is equal to or greater than the laser wavelength, light is scattered elastically and the field is enhanced several times at the exit side of the spheres. Mie theory calculations show that this enhancement is due to both near-field and scattering effects [82]. Such optical enhancement can lead to local melting or even vaporization of the substrate materials for nanoscale surface patterning. It has been reported that the intensity distribution changes dramatically with the size of the sphere and also the distance between the sphere and the substrate [28].

When the laser beam is incident from the backside of the sample, the effect of scattering on the surface modification is minimized, only optical the near-field enhancement effect for surface modification is used.

The influence of the incidence wave angle on the pattern structures was also investigated [12], as shown in figure 1.13. Polystyrene spherical particles were deposited on the surface in a monolayer form by self-assembly. The sample was then irradiated with 248 nm KrF laser at different incidence angles. It was found that nanostructures can be formed at different positions with different incidence angles. Both round-shape and

comet-shape nanostructures can be produced. By varying the incidence angles, the depth of the nanostructures can also be controlled.

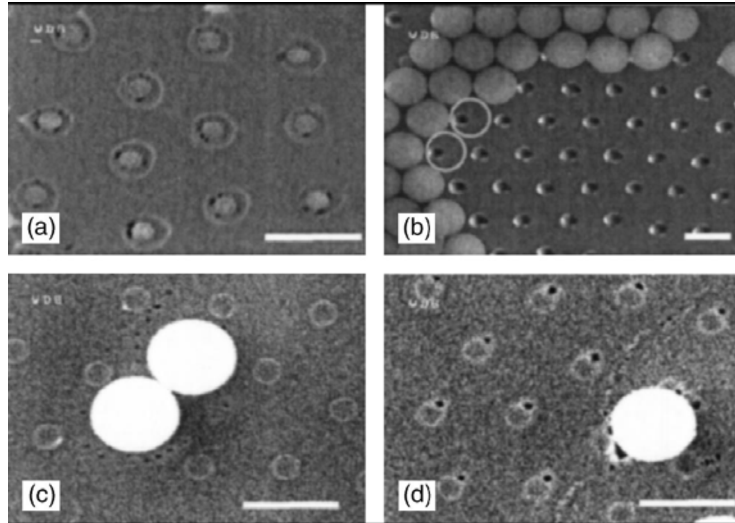

Figure.1.13 SEM images of nanodent structures formed on a $Ge_2Sb_2Te_5$(GST) film under the removed particles after one laser pulse irradiation at different incidence angles of (a) a =0°, (b) a =30°, (c) a =45° and (d) a =60°, respectively. Laser fluence is 7.5 mJ/cm^2. Scale bar is 1.0 µm [12].

1.2.4- Holographic patterning and direct laser interference

Holographic patterning as shown in figure 1.14, involves the interference of two or more laser-beams and allows rapid fabrication (~seconds) and high design flexibility not limited by multiphase equilibrium [83, 84]. The major advantage of this technique is that it is a relatively simple and fast process which consists of two steps: exposure and development.

In the case of two mutually coherent and interfering laser-beams, the resultant pattern of field intensity can be readily recorded in a thin film of photoresist. After development, an array of parallel lines will be created in the photoresist film.

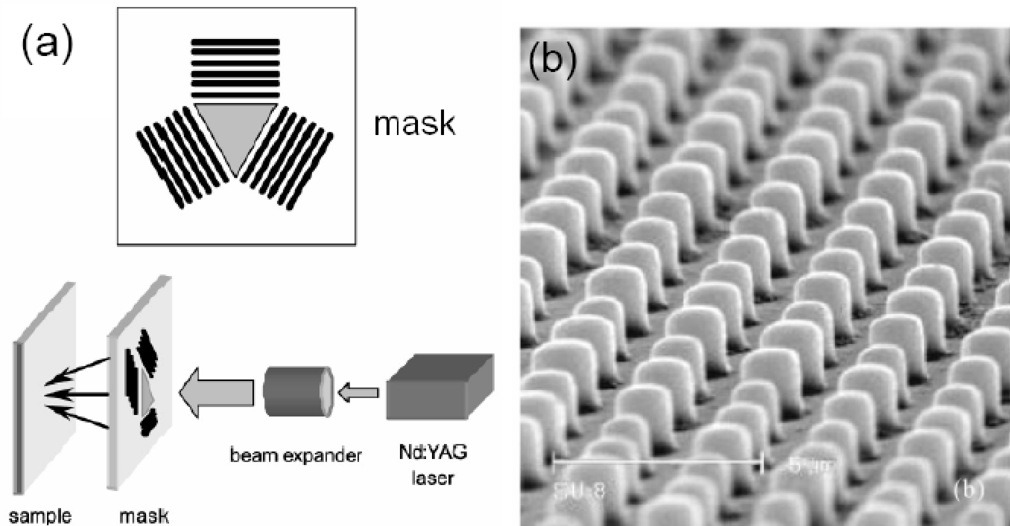

Figure 1.14 (a) Schematic illustration of the hexagonal interference patterning process. (b) SEM image of the negative photoresist columns created by hexagonal patterning [85].

This method is commonly used to fabricate photonic crystals by forming a polymer template through exposure of a photoresist to the interference pattern [85, 86]. Normally, a diffraction-mask is employed to produce the interference patterns [85-88]. For example, figure 1.14 shows the interference pattern produced with a collimated Nd:YAG laser-beam impinging on a mask that has three gratings oriented 120° relative to one another. Each grating has 2 mm wide, 4 mm long features separated by 2 mm. The photoresist sample is exposed by placing it at the focal point of the diffraction pattern, yielding a hexagonal array of photoresist columns. By exposing the same photoresist film to the interference pattern twice (orthogonal to each other), a 2D array of posts will be generated. This technique is widely used in the photonic industry to manufacture holographic diffraction gratings and anti-reflection coatings [89].

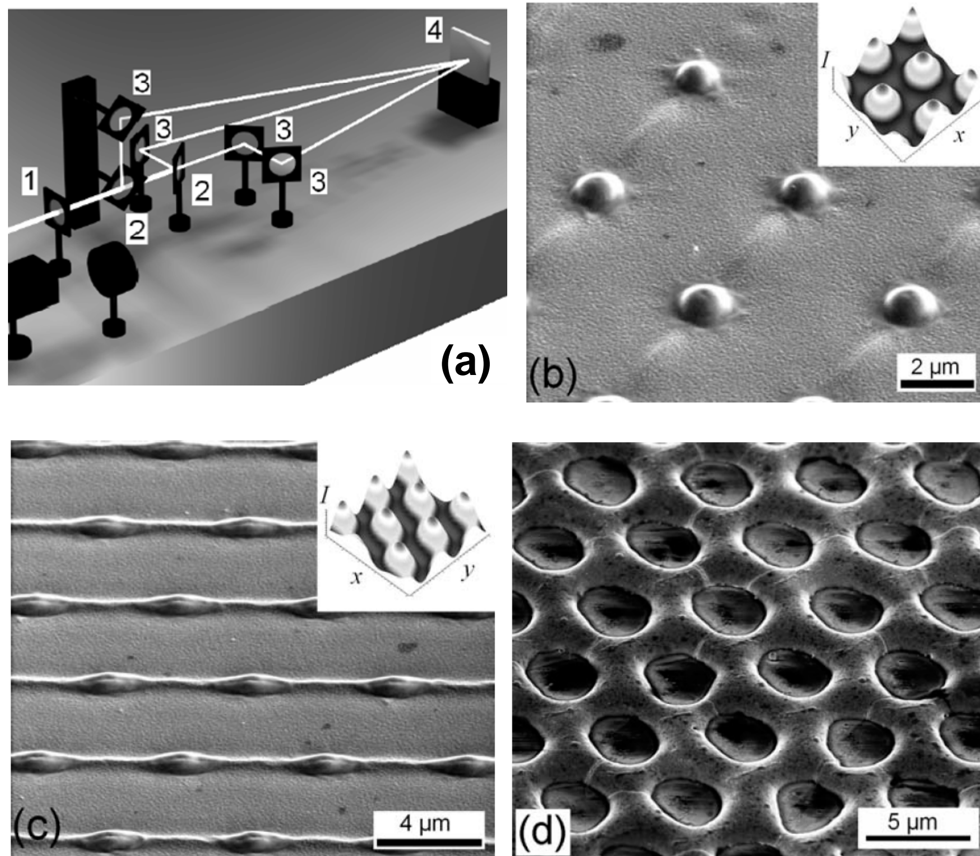

Figure 1.15 (a) Schematic set-up for the laser interference system with the optical elements: (1) lens; (2) beam splitters; (3) mirrors; (4) sample. Note that the primary beam is divided into 3 sub-beams which are overlapped at the sample surface. (b), (c) and (d) are patterns in Fe and Al films[14].

The "direct laser interference structuring" method makes use of interference of two or more laser-beams, like in holographic patterning, but in this case no development of the irradiated sample is needed, as shown in figure 1.15 [14]. The most important requirement to produce the periodical structures with this method is that the material to be processed must absorb the energy of the laser at the selected wavelength and the laser must be of high-power. The method allows the production of periodic structures of features with a well defined long-range order in the scale of typical microstructures (i.e. from the sub-micrometer level up to micrometers). The micropatterning process is based on mechanisms of photo-thermal, photo-physical, or photo-chemical nature, depending

on the type of material.

In addition, in the case of laser interference patterning, no masks are required. Relatively large areas can be directly structured (of the order of cm^2) in a time scale of a few seconds. For example, using the direct laser writing technique, about 56 hours are required to produce a periodical line-type structure on an area of 3mm x 3mm with a period of 10 μm. The same structure can be realized in only 10ns using the direct laser interference patterning technique [14].

Direct laser interference patterning has been applied to different materials such as semiconductors, metals, ceramics, and polymers [15, 90]. In the case of metals, the interference pattern produced by beams of a high power pulsed laser permits direct, periodical local heating of the surfaces through the local photo-thermal interaction between laser and metal. In the process of light interaction with metals, the light quanta are absorbed by conducting electrons, which dissipate the absorbed energy as thermal lattice vibrations. Thus, different metallurgical effects such as melting, recrystallization, quenching, recovery, defect or phase formation can be exploited.

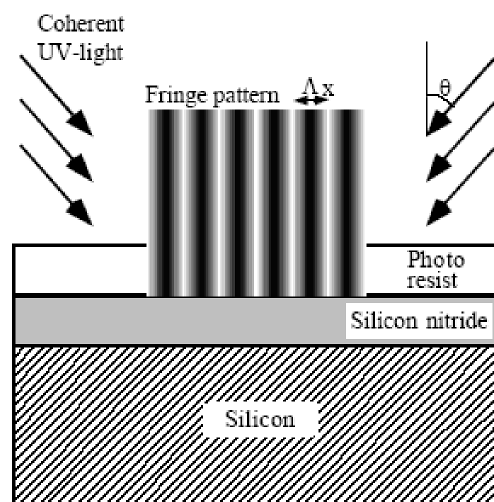

Figure 1.16 Interference pattern created by two coherent beams[13]

When two beams of coherent light interfere, a pattern of parallel fringes will appear. These fringes can be used for the exposure of a photosensitive layer. Figure 1.16 [13] gives a schematic illustration of this method of exposure.

The depth-of-focus of this method is dependent on the coherence length of the light and can be of the order of meters or more, compared to microns for conventional optical lithography systems. As a result, the demands on substrate flatness and wafer positioning are not critical.

If the light intensity of each beam is I_0, the irradiance on the surface is given by:

$$\mathrm{I} = 4I_0 \sin^2\left(\frac{\pi x}{\Lambda_x}\right) \tag{1.4}$$

With Λ_x the fringe period in the x-direction (see figure 1.14):

$$\Lambda_x = \frac{\lambda}{2\sin\theta} \tag{1.5}$$

Here, λ is the wavelength of the laser light in the medium that surrounds the substrate (usually air) and θ is the half angle between the two beams. The smallest period that can theoretically be obtained occurs when $\theta = 90^\circ$ and is equal to $\lambda/2$.

1.3 Motivation and dissertation outline

The primary motivation of this doctoral dissertation is to investigate laser-based direct-write and patterning methods for making two-dimensional and layered three-dimensional micro- and nanostructures. This chapter presented detailed reviews of “laser direct writing process”, “Direct laser interference structuring” and “Laser-induced near-field patterning”.

Chapter 2 presents experimental and theoretical analysis of direct-write laser

micromachining of polymethyl methacrylate (PMMA) by CO_2 laser ablation. In contrast with large size channels (100μm-500μm in width) fabricated in the previous works, I mainly focus on low laser power which can reduce the cost of the fabrication system, and low scanning speed to obtain narrow channels. The laser power used for channel fabrication range from 0.45W to 1.35W and the scanning speeds range from 2mm/s to 14mm/s. The width and the depth of channels range from 44μm to 240 μm and 22μm to 130μm respectively. Physical models are developed for the depth and channel profile of ablated channels. This work incorporates the threshold fluence for CO_2 laser ablation of PMMA into the model to predict the profile of the channel. The models are in excellent agreement with experimental results, with a maximum deviation of approximately 5%.

Chapter 3 is focused on frequency-doubled ND:YAG laser direct-write polymerization. The first part of the chapter is dedicated to the mechanism of laser-induced polymerization and biocompatible hydrogel materials. In section 3.3, experimental procedure, sample preparation and experimental setup are discussed in detail. A resolution of 840nm with PETIA, which is the highest resolution by laser direct-write polymerization, can be realized with this system. In the theoretical simulation part, a numerical model with Monte Carlo method was developed to simulate light scattering and absorption in photocrosslinkable materials. The cure depth and width can be predicted by this model, which is in excellent agreement with experimental results. The successful fabrication of square-, circular-, and honeycomb-cellular structures demonstrates the ability of this technique to fabricate micro patterns with arbitrary shapes in a wide variety of functional materials, which is shown in the last part of this chapter.

Chapter 4 presents the technique of direct laser interference patterning. This

technique is used for rapid and large area fabrication of two-dimensional and three dimensional periodic structures in photopolymerizable materials with 10ns pulses from a frequency-tripled Nd:YAG laser emitting at 355 nm. Surface areas up to 3.6 cm^2 can be patterned in one second showing the high fabrication speeds that can be reached. Different periodic structure arrays including line-, cross-, honeycomb- and dot-like structures were fabricated. For samples irradiated with three beams, by tuning the laser intensity or number of laser pulses, it was possible to fabricate different types of periodic arrays from isolated dots to symmetric honeycomb structures. Three-dimensional line-like structures were for the first time successfully fabricated with SU-8 associating with absorber TINUVIN 384-2. Concentrations of 1%-2% of absorber were found to be appropriate to achieve massive, stable three-dimensional structures. By adjusting the separation angle between two incident beams, sub-microm line-like patterns were realized with Shipley 1813.

Chapter 5 describes Laser-induced near-field patterning. Features created on Poly(3,4-ethylene dioxythiophene)-poly(styrenesulfonate) (PEDOT-PSS) thin films by the irradiation of nanospheres on the film surface with a pulsed laser are presented. The features indicate an enhancement of the incident intensity in the near field due to the presence of the sphere. The near field has been calculated for a single sphere on a substrate using the results of Mie theory. The results of these calculations predict a strong enhancement directly under the sphere, which is assumed to be responsible for the substrate damage. Periodic nano-cavity arrays were for the first time patterned by combining direct laser interference technology and laser induced near-field technology.

Chapter 6 concludes with a summary of the research described in this dissertation.

CHAPTER II

DIRECT-WRITE MICROMACHING OF POLYMETHYL-METHACRYLATE (PMMA) BY CO_2 LASER ABLATION

The main motivation for this work was to develop experimental techniques for micromachining of PMMA by CO_2 laser ablation and corresponding physical models for the depth and profile of micromachined channels, especially for low laser power (0.45–1.35W) and low scanning speed (2-14mm/s). The models developed in this work incorporate for the first time, the threshold fluence for ablation of PMMA by CO_2 laser radiation, to predict the channel profile achievable with low laser power. Within the range of parameters tested, these models can be used to predict the channel depth and profile for a specific choice of laser power and scanning speed.

2.1 Mechanism of CO_2 laser processing PMMA

Poly(methyl methacrylate) (PMMA), whose structure is shown in figure 2.1, is a fast-burning thermoplastic. PMMA has long been regarded as a viable surrogate fuel for modeling the behavior of hybrid rockets in which the oxidizer (usually air or O_2) passes over the surface at a high velocity. Following ignition, pyrolysis at the fuel surface produces volatile molecules to sustain the flame zone. Because PMMA is widely used in consumer products, its thermal decomposition, ignition, and combustion characteristics have motivated the majority of previous studies.

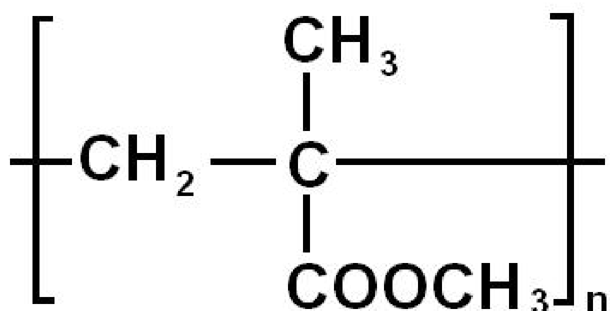

Figure 2.1 Chemical structure of Poly (methyl methacrylate) (PMMA).

The thermal decomposition process of PMMA is more exhaustively studied than most other polymers, in part because the process is comparatively straightforward. The random chain-breaking model of Kuhn [91] and the end-chain scission model of Simha [92] for polymer degradation appear to apply to PMMA. Because of the very large zip length of PMMA (the number of monomers produced per single initiation event), the overwhelmingly dominant product released from the bulk phase is the monomer methyl methacrylate (MMA). Although this process would seem to be relatively simple, the mechanistic details have motivated more than 50 years of study. Most inferences have been drawn from the decomposition characteristics at temperatures below 360°C. For radically polymerized PMMA, at least two processes are revealed. The interpretation is that one of these processes involves depolymerization initiated by the vinyl end groups, while the other involves initiation at saturated C-C bonds, including the $–CH_3$ end-group [93, 94]. Opinions vary as to whether the rate is faster for the saturated or the unsaturated site. For anionically polymerized PMMA, no unsaturated end groups exist, which makes the thermal stability higher than that of radically polymerized PMMA. Random C-C scission is the dominant mechanism of depolymerization. Of course, various termination

reactions compete with the depolymerization reaction.

The process of a plate of homogeneous and isotropic material absorbing a monochromatic and parallel laser beam (incident power density I_0) can be described by the Beer-Lambert law, which gives the power density I at the depth z:

$$I = I_0 \exp(-az)$$

where a is the spectral absorption coefficient (cm^{-1}). In reference [60], values for a from $10^2 cm^{-1}$ to $10^5 cm^{-1}$ are reported for PMMA.

A strong rise in temperature occurs due to the high power density of the focused incident laser beam radiation. The material will first melt and then decompose, leaving a void. Poly (methyl methacrylate) (PMMA) is a fast-burning thermoplastic. Below 115°C, it remains in glassy state. When the temperature increases beyond 115°C, PMMA reaches a rubbery state. At higher temperatures between 170°C and 210°C, long range deformations of chains of molecules occur. The thermal decomposition process of PMMA is comparatively straightforward. Because of the very large zip length of PMMA, the overwhelmingly dominant product released from the bulk phase is the monomer methyl methacrylate (MMA). The main part of decomposition occurs at temperatures around 360°C depending on the heating rate.

2.2 Experimental design and set-up

2.2.1 CO_2 laser system

An experimental system for PMMA channel fabrication is shown in figure 2.2. The laser system is a series48 commercial laser system from SYNRAD whose maximum output power is 50W, beam diameter is 3.5mm and beam divergence (full angle) is 4mrad.

The 3.5 mm beam was collimated using a 10x beam expender (CVI laser) to a 30mm beam. The 30 mm diameter Gaussian laser beam was focused on the surface of the sample using a ZnSe lens with 63.5 mm focal length. The sample was mounted on a XY table driven by stepping motors; moving range is 200mm×200mm. A focused beam radius ($1/e^2$) of 320μm was measured by a high precision beam profilemeter (Photon Inc. NanoScan) with 93% Gaussian fit. The laser power ranged from 0.45 W to 1.35 W.

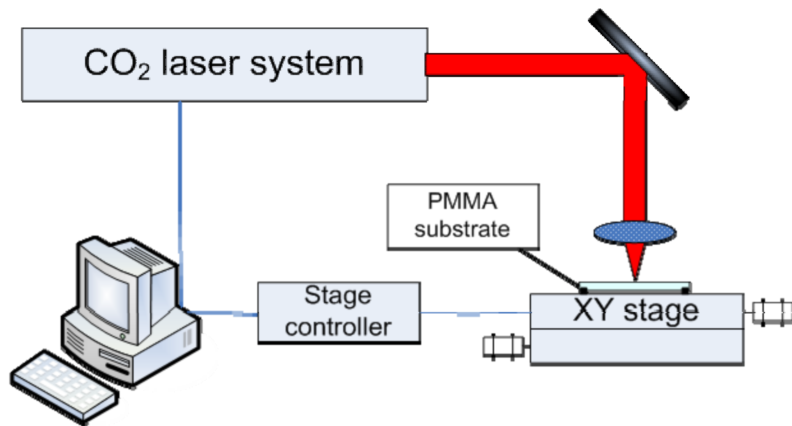

Figure 2.2 Experimental system for PMMA channel fabrication.

2.2.2 Experimental determination of threshold fluence

First, the threshold fluence for CO_2 laser ablation of PMMA was investigated in the incident laser power range of 0.45W to 1.35W. For a scanning speed of v in the experiment of channel fabrication, the single irradiation time t_s is 2R/v. With different laser powers and irradiation times, a series of burn patterns were made, as shown in figure 2.3. The threshold fluence of PMMA was derived by substituting the radius of these patterns y_w, the irradiation times t_s and the laser power P into Equation (2.18). As shown in table 2.1, the experimentally determined threshold fluences are close to the

F_{th}=0.15 J/mm^2 reported in previous work [95] in the power density range of 60 W/cm^2 to 120 W/cm^2. The variation of threshold fluence across the range of laser power in table 1 is small, therefore the mean threshold fluence, $\overline{F_{th}} = 0.173$ J/mm^2 was used.

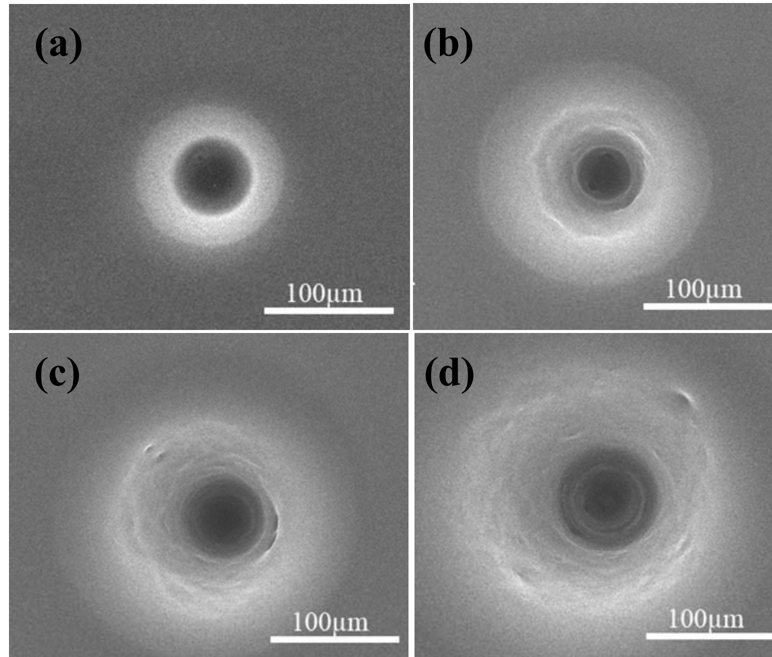

Figure 2.3 Burn patterns in PMMA. The irradiation time t_s and laser power P for each spot (a) t_s= 0.12, P=0.46; (b) t_s= 0.08, P=0.73; (c) t_s= 0.07, P=0.98; (d) t_s= 0.1, P=0.73.

P (W)	t_s (s)	y_w (mm)	F_{th} (J/mm^2)
0.46	0.12	0.091	0.178
0.73	0.1	0.186	0.176
0.73	0.08	0.128	0.172
0.98	0.07	0.179	0.170
1.12	0.05	0.118	0.171
1.31	0.04	0.079	0.173

Table 2.1 Threshold fluence of PMMA

2.2.3 Channel micromachining

PMMA raw material (type 99530) was received from Altuglas International, in the form of 2 mm thick extruded sheet. The sheet was then cut into 20mm x 20mm pieces for microchannel machining, and 20mm x 5mm for microchannel profiles observation.

The PMMA sample was mounted on an x-y stage. The position and speed of the stage were controlled by two stepper motors. In the experiments, the scanning speed was varied between 2 and 14 mm/s. In order to investigate how the channel depth and the channel width depend on the laser power and scanning speed from the cross-sections, a test layout was designed as shown in figure 2.4. First a measurement part with dimensions of 30mm long, 7 mm wide and 5 mm thick was prepared by milling and polishing the measurement surface before laser fabrication. A protecting part with the same thickness and length was then mounted together with measurement part on the X-Y stage to avoid damage to the stage from the laser beam. A series of channels with varying laser power and scanning speed were fabricated by controlling the stage and CO_2 laser. After fabrication, the measuring surface was given a quarter turn to face upward and the channel dimensions were measured with a scanning electron microscope (Philips XL30).

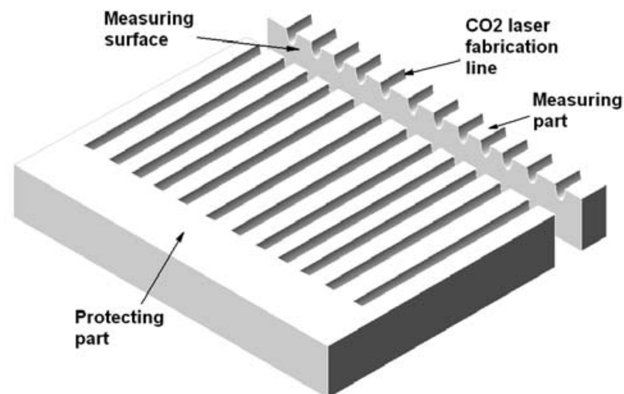

Figure 2.4 Experiment design for CO_2 laser direct-writing.

2.3 Mathematical models of channel depth

A model of CO_2 laser ablation based on a heat balance and the Gaussian mode of propagation was developed. We consider a Gaussian laser beam, which strikes the surface of a substrate, having semi-infinite thickness and infinite length, moving in the positive x-direction with a uniform velocity v. The laser power is absorbed at the surface. Once the material reaches the evaporation temperature T_v, it consumes some latent heat. The following three assumptions were made.

1) The CO_2 laser beam propagation can be described by Gaussian distribution as follows:

$$I(x,y,z) = \frac{P}{\pi w^2(z)} e^{(-\frac{x^2+y^2}{w^2(z)})} \tag{2.1}$$

$$w^2(z) = R^2[1+(\lambda z/\pi R^2)^2] \tag{2.2}$$

Where P is laser power, w(z) is the laser beam radius at z. Because of $\lambda z/\pi R^2 << 1$, w(z) can be treated as a constant R.

2) Volatiles will not affect the CO_2 laser.

3) Energy losses due to radiation and conduction are negligible.

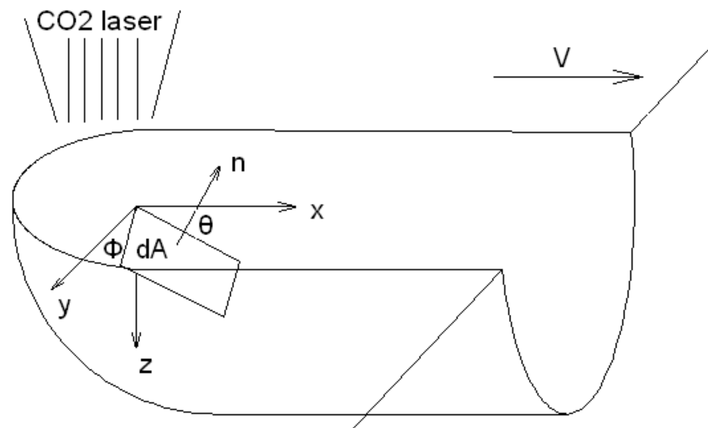

Figure 2.5 Schematic diagram of PMMA channel and surface element.

The complex 3D channel surface as shown in figure 2.5, can be separated into finite surface elements described by inclination angles θ in the x direction and Φ in the y direction [96]. For each element, the energy balance can be described as follows: the laser input energy is equal to the energy that conducts into the surface element and the decomposition energy:

$$E_{laser}\,dxdy = E_{conduction}\,dA + E_{decomposition}\,dxdy \tag{2.3}$$

From the geometry relationship in figure 2.5:

$$dA = \sqrt{1+\tan^2\theta + \tan^2\varphi}\;dxdy \tag{2.4}$$

The laser input energy density is given by:

$$E_{laser} = \int_{-\infty}^{+\infty} I(x,y,z)\frac{dx}{v} = \int_{-\infty}^{+\infty} \frac{aP}{\pi v w^2(z)}\exp\left(-\frac{x^2+y^2}{w^2(z)}\right)dx = \frac{aP}{\sqrt{\pi}Rv}\exp\left(\frac{-y^2}{R^2}\right) \tag{2.5}$$

where a is the absorptance of PMMA at the CO_2 laser wavelength of 10.6 µm.

The decomposition energy is given by:

$$E_{decomposition}\,dxdy = \rho L D(y)\,dxdy \tag{2.6}$$

Where ρ is the density of PMMA, L is latent heat of decomposition from PMMA to MMA and D(y) is the depth of the channel at y.

The energy conducted into the surface is given by:

$$E_{conduction}\,dA = \left(\int_{-\infty}^{+\infty} -k\left(\frac{\partial T}{\partial n}\right)\Bigg|_{n=0}\frac{dx}{v}\right)dA \tag{2.7}$$

The heat transfer equation for the moving heat source with velocity v in the x-direction is:

$$\nabla^2 T = \frac{\partial^2 T}{\partial n^2} = \frac{v}{\alpha}\frac{\partial T}{\partial x} \tag{2.8}$$

Where α is thermal diffusivity with units of m^2/s.

From the geometry in fig.2.5, the following relation can be derived:

$$E_{conduction} dA = (\int_{-\infty}^{+\infty} \frac{k}{\alpha}(T_v - T_0)\tan\theta dx)dxdy = \frac{k}{\alpha}(T_v - T_0)D(y)dxdy \qquad (2.9)$$

where T_0 is room temperature and T_v is decomposition energy, k is thermal conductivity with units of W/(m K). From Equation (2.5, 2.6, 2.9), Equation (2.3) becomes:

$$\frac{aP}{\sqrt{\pi}Rv} e^{\left(\frac{-y^2}{R^2}\right)} dxdy = \rho L D(y)dxdy + \frac{k}{\alpha}(T_v - T_0)D(y)dxdy \qquad (2.10)$$

The channel depth D(y) can be obtained from Equation (2.10) as:

$$D(y) = \frac{aP}{\sqrt{\pi}Rv\left(\rho L + \frac{k}{\alpha}(T_v - T_0)\right)} e^{\left(\frac{-y^2}{R^2}\right)} \qquad (2.11)$$

When y=0, the depth of the channel can be solved as:

$$D(0) = \frac{aP}{\sqrt{\pi}Rv\left(\rho L + \frac{k}{\alpha}(T_v - T_0)\right)} \qquad (2.12)$$

Therefore, the channel profile in the y-direction can be expressed as:

$$D(y) = D(0)e^{\left(\frac{-y^2}{R^2}\right)} \qquad (2.13)$$

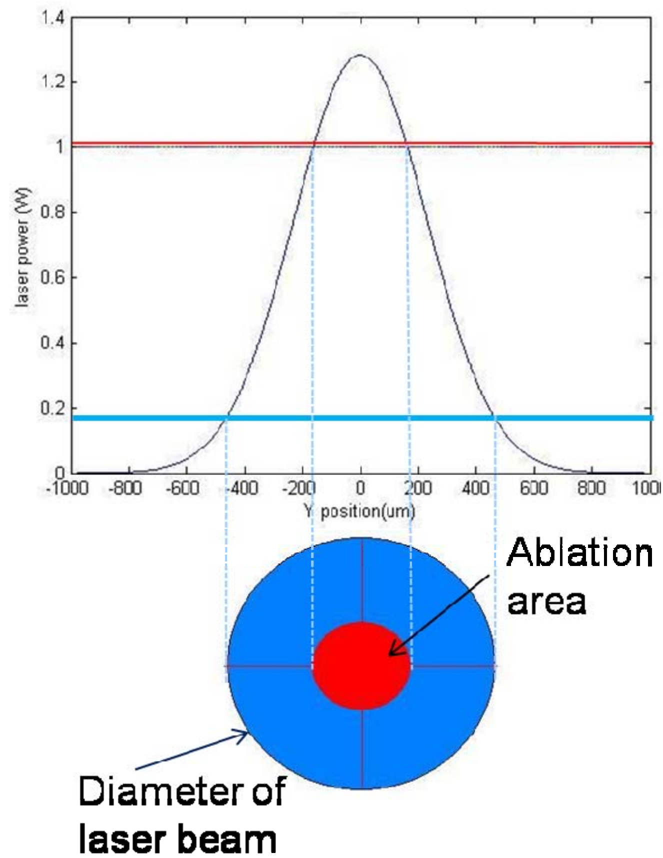

Figure 2.6 Schematic of laser diameter and ablation area.

From the form of Equation (2.13) it can be seen that the profile of the channel is also Gaussian. The width of the channel is the width of the laser beam. This expression is applicable for high power density laser fabrication which can ablate PMMA in the entire area of laser width. As for the low laser power case, the laser input energy is not sufficient to ablate all the PMMA material exposed to the laser beam because of a Gaussian intensity distribution. Beyond a given radius, the energy intensity is below the threshold fluence required to initiate ablation of PMMA. Consequently the channel profiles have a smaller width than that of the laser beam. Therefore, R term in Equation (2.13) needs be corrected. For a given energy density I_s, there is a threshold irradiation

time t_s that causes visible damage on the PMMA substrate. The product of I_s and t_s can thus be defined as the threshold fluence for laser ablation of PMMA, F_{th}.

$$F_{th} = I_s t_s \tag{2.14}$$

Then

$$I_s = \frac{F_{th}}{t_s} \tag{2.15}$$

But

$$t_s = \frac{2R}{v} \tag{2.16}$$

So we can get:

$$I_s = \frac{F_{th} v}{2R} \tag{2.17}$$

$I_s = I_{th}$ for a given v, or equivalently for a given exposure time t_s. For x=0, the intensity distribution of laser is given by Equation (2.1). At $I=I_{th}$, the threshold intensity to initiate ablation of PMMA, $y=y_{th}$

$$I_{th} = \frac{P}{\pi R^2} e^{\left(-\frac{y_{th}^2}{R^2}\right)} \tag{2.18}$$

Since F_{th} can be determined from experiments, we can solve for y_{th} from Equation (2.17, 2.18), as follows:

$$\frac{P}{\pi R^2} e^{(-\frac{y_{th}^2}{R^2})} = \frac{F_{th} v}{2R} \tag{2.19}$$

$$y_{th} = R\sqrt{\ln \frac{2P}{\pi R F_{th} v}} \tag{2.20}$$

Substituting R in Equation (2.13) by y_{th}, the corrected channel profile in the y direction for low laser power fabrication is given by:

$$D(y) = D(0)e^{(\frac{-y^2}{{y_{th}}^2})} \tag{2.21}$$

2.4 Results and discussion

Experiments were focused on fabricating channels with low laser powers and low scanning speeds. With the parameter ranges reported in section 4, the resulting channel depths ranged from 22µm to 130µm, while the channels widths ranged from 44µm to 240µm.

2.4.1 PMMA channel depth

Our model for channel depth in Equation (2.12) predicts a linear relationship between channel depth, D(0), and laser power, P, for fixed scanning speed and beam diameter. In order to compare this theoretical model with the experimental results, the channels were fabricated in PMMA with a constant scanning speed and at different laser powers. Figure 2.7 presents the depth of the channels versus the laser powers at different scanning speeds along with the theoretical model plotted for the experimental conditions investigated. There is excellent agreement between the theoretical model and our experimental results despite the exclusion of energy losses due to radiation and conduction in the model. For a given scanning speed, the channel depth is linearly proportional to laser power. At fixed laser power, channel depth is inversely proportional to scanning speed.

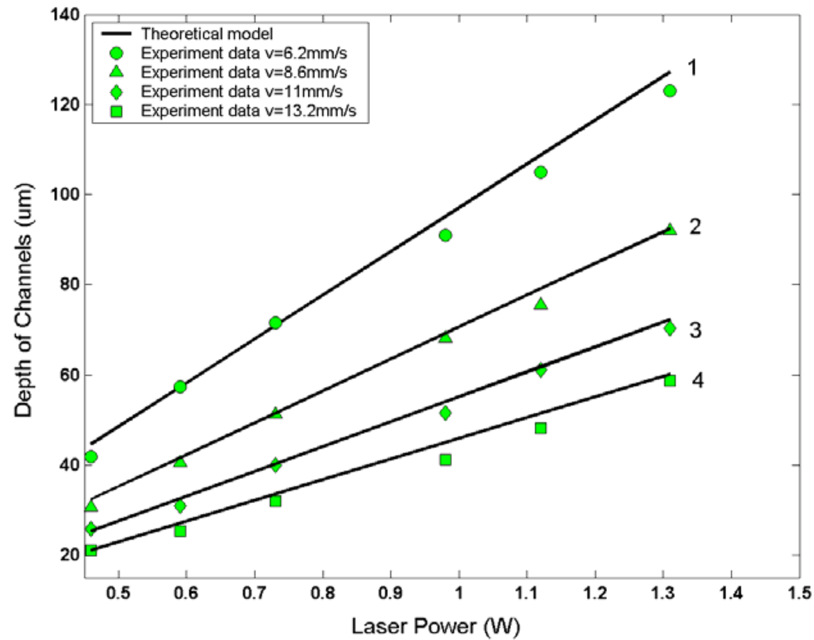

Figure 2.7 Channel depths as a function of laser power at different scanning speeds. The solid lines represent the theoretical fit. 1: v=6.2mm/s, 2: 8.6mm/s, 3: 11mm/s, 4: 13.2mm/s.

2.4.2 PMMA channel profile

With $\overline{F_{th}}$ and Equation (2.15, 2.16), the channel profile was modeled for different fabrication parameters. The model indicated that the profiles of the channels are Gaussian shapes because of the Gaussian distribution of the ablating laser. In total, 64 comparisons of the experimental channel profiles with modeling results were made, and approximately 5% deviation was observed between the model and the experimental data. Figure 2.8 shows scanning electron micrographs of two typical experimental channel profiles and the superimposed modeling results for different laser power and scanning speed. For a given scanning speed, the channel width is proportional to laser power and inversely proportional to scanning speed.

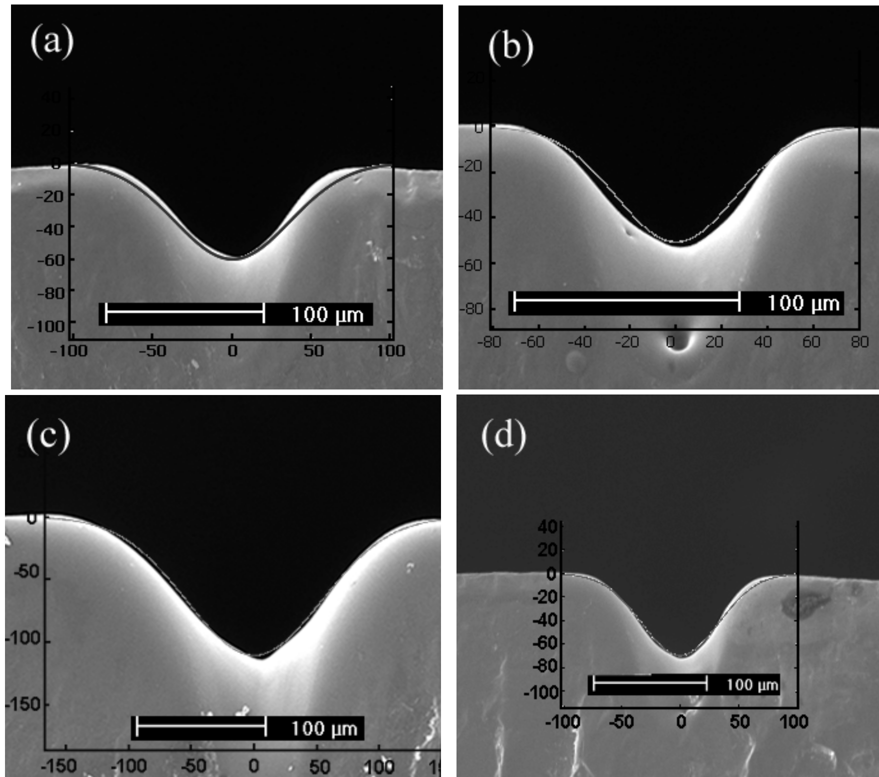

Figure 2.8 Modeling of PMMA channel profile. (a) P= 0.8W, v=8.6mm/s; and (b) P= 0.98W, v=11mm/s [97].

2.5 Summary and conclusions

It has been shown that infrared laser micromachining is a tool for rapidly producing microfluidic structures in PMMA. In this chapter, a micromachining system was designed and realized. The laser power used for channel fabrication ranged from 0.45W to 1.35W and the scanning speeds ranged from 2mm/s to 14mm/s. The width and the depth of channels ranged from 44µm to 240 µm and 22µm to 130µm respectively. Physical models that can be used to calculate the channel depth and channel profile from the laser settings were presented and shown to be reliable with a maximum deviation of approximately 5%.

CHAPTER III

DIRECT-WRITE PHOTOPOLYMERIZATION USING A FREQUENCY-DOUBLED Nd:YAG LASER

Laser direct-write photopolymerization is also known as the stereolithography process, which was invented and patented by Dr. Charles Hull in the 1980s. It is the first and most widely used rapid prototyping technique. It allows building a part layer-by-layer through laser induced polymerization. The laser beam is focused and scanned on the open surface of a photosensitive liquid and a liquid/solid transformation occurs locally, which allows the creation of an arbitrary shape of one layer of the object. When a layer is finished, fresh resin is spread on top of the already manufactured part of the object, and the light-induced solidification of the next layer is started.

Microstereolithography is the general designation of various microfabrication technologies based on the principle used in stereolithography. All microstereolithography machines have the same aim and the same basic principle: They allow building small-size, high-resolution three-dimensional objects, by superimposing a certain number of layers obtained by a light-induced and space-resolved polymerization of a liquid resin into a solid polymer.

Zissi et al. published a paper describing a microstereolithography process using an Argon ion laser in 1996. Specific photopolymerizable materials were developed based on

acrylate formulations. The resolution for the system was 30μm x 30μm x 20μm (x,y,z) [61]. More recently, Zhang et al. also designed a similar microstereolithography system [64]. The UV curable resins developed for the setup contained 1,6 hexanediol diacrylate (HDDA) as a low viscosity monomer, and a conventional UV initiator. The resolution was improved to be 2μm x 2μm x 2μm (x,y,z).

The main motivation for this work was to design and develop an advanced laser direct-writing system with low cost visible laser (frequency-doubled Nd:YAG laser) to realize even higher resolution and the ability to process a wide range of materials for microfabrication. An additional motivation was to develop physical models of the direct-write photopolymerization process using a Monte Carlo method. Assuming good correlation with experimental results, these models would allow the shape of a polymerized unit to be predicted as a function of input laser fluence.

3.1 Mechanism of laser induced polymerization

Photopolymerization refers to the process of using light as an energy source to induce the conversion of small unsaturated molecules in the liquid state to solid macromolecules thorough polymerization reactions. Although other radiations, including x-ray, g-ray, microwave, and even electron and ion beams can induce similar curing reactions [98], photopolymerization deals with those that are induced by light in the UV, visible, to IR spectral region. The advantages of liquid photocurable resins extend beyond their composition involving fully 100% reactive components. These systems are also energy efficient, requiring 50 to 100 times less energy than that consumed in thermally cured coatings. The basic components of the starting liquid material are monomers (or prepolymer). Upon light excitation, the monomers or oligomers may be solidified by two

means: polymerization and crosslinking [98-102]. An important feature of polymerization is the chain reaction by which macromolecules are created; while cross-linking is concerned more with the formation of crosslinks with chemical bonds (different from the entangling of polymer chains). An important difference of these two kinds of reaction lies in their quantum yield, which is defined as the ratio of number of polymerized monomer units to the number of photons that are needed to cause this polymerization. In the case of photocrosslinking, addition of each monomer unit requires absorption of a photon, leading to a quantum yield less than 1. In contrast, photopolymerization is realized via chain reactions as shown in equation (3.1), so the quantum yield can reach several thousands [102].

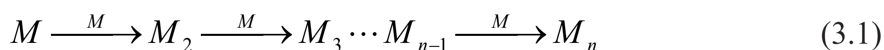

$$M \xrightarrow{M} M_2 \xrightarrow{M} M_3 \cdots M_{n-1} \xrightarrow{M} M_n \tag{3.1}$$

Here M is the monomer or oligomer unit, and M_n, the macromolecule containing n monomer units.

Vinyl monomers are broadly defined as monomers containing a carbon-carbon double bond. The vinyl group may be attached to other molecular structures, represented by “R” in figure 3.1 [103]. The “R” group may contain one or more other vinyl groups, in which case the monomer is called multifunctional, difunctional or trifunctional and so on. Polymerization of multifunctional monomers results in a cross-linked polymer, as shown in figure 3.2.

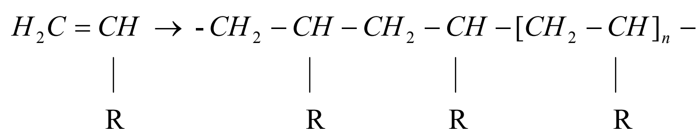

Figure 3.1 Schematic of Vinyl monomers.

Chemical reaction of the vinyl group allows each carbon atom in the carbon-carbon

double bond to form a new bond, typically with a carbon atom from another monomer molecule. In going from loose Van der Waals interactions with neighboring monomers to a network of covalent bonds, many bulk properties change. As shear strength increases, the system changes from liquid to solid. The average distance between groups decreases, resulting in an increase in density, and thus shrinkage. For multifunctional systems, these changes will tend to occur at a lower degree of reaction.

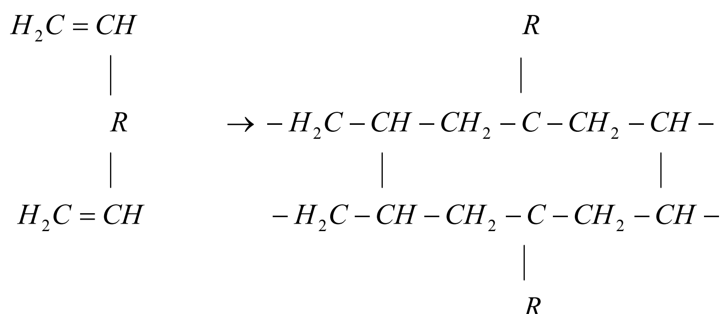

Figure 3.2 Schematic of polymerization of multifunctional monomers.

Acrylate monomers are a subset of the vinyl family with high reactivity and versatility due to the carboxylic acid group (-COOH) attached to the carbon-carbon double bond. Attachment of various chemical segments (through acrylate ester functionality) is a relatively easy transformation. This has led to the great variey of acrylate functionalized monomers.

For practical photopolymer systems, more components are included, most importantly photoinitiators and photosensitizers [98-102]. The quantum yield of general monomers and oligomers is low. In order to increase the initiating efficiency, one or several low-weight molecules that are more sensitive to light irradiation are added. They form initiating species of radicals or cations by absorbing photons. Such small molecules are called photoinitiators. The production of active species that attack monomers or oligomers is called photoinitiation, the most important step in photopolymerization. Take

the radical case for example, with the following initiation step:

$$I \xrightarrow{hv} I^{*} \longrightarrow R\cdot \tag{3.2}$$

where symbols denote photoinitiator (I), radical (R·) and I*, an intermediate state of the photoinitiator after absorbing a photon. Therefore the polymerization process is more precisely described by the following equation:

$$R\cdot + M \rightarrow RM\cdot \xrightarrow{M} RMM\cdot \cdots \rightarrow RM_n\cdot \tag{3.3}$$

The photoproduced radicals react with monomers or oligomers, producing monomer radicals, which combine with new monomers, and so on; so the monomer radicals expand in a chain reaction, until two radicals meet with each other. This chain propagation stops in either of the following channels:

$$RM_n\cdot + RM_m\cdot \rightarrow RM_{m+n}R \tag{3.4}$$

$$RM_n\cdot + RM_m\cdot \rightarrow RM_n + RM_m \tag{3.5}$$

Therefore the polymerization process consists of several steps: (i) photoinitiation (Equation 3.2), (ii) chain propagation, (Equation 3.3), and (iii) termination, (Equation 3.4, 3.5). We can see from the above description that a good photoinitiator should be (i) easily reduced to an initiating species upon light irradiation, and (ii) provide photoproduced radicals or cations active enough to react with monomers or oligomers.

On the average, for every two actinic photons (roughly 1.2 x 10^{-18} Joule of energy), one radical will be produced. Each radical will result in the polymerization of more than 1000 acrylate monomers.

In many cases, the energy collection and triggering chain polymerization are cooperatively accomplished by multi-type molecules. A photosensitizer is a molecule that

absorbs light and then transfers the energy to a photoinitiator. With such a scheme, the photoinitiation process is expressed as:

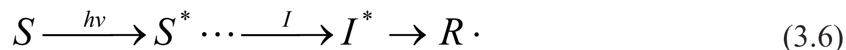

$$S \xrightarrow{hv} S^{*} \cdots \xrightarrow{I} I^{*} \rightarrow R \cdot \quad (3.6)$$

where S is the photosensitizer. A coinitiator itself does not absorb light, but it is involved in the production of radical species. The above descriptions of polymerization are based on radical initiators. Actually, photopolymerization reactions are basically classified into two categories: radical polymerization and ionic polymerization. Among these two types of photopolymerization, reactions that are typically used for laser fabrication are [98-102]:

(i) double-bond addition of acrylates (radical-type)

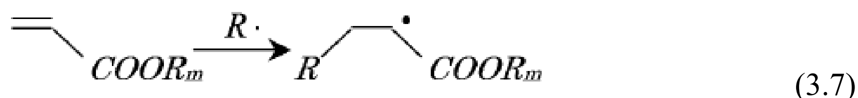

(3.7)

(ii) ring-opening of expoxides (cationic-type)

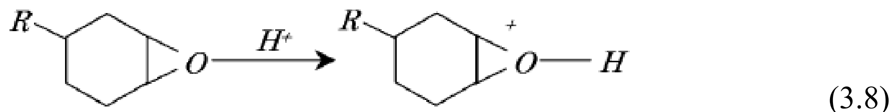

(3.8)

These two types of reactions require triggering by different initiators. For a radical type initiator, benzoyl is the most widely used chromophore since it exhibits good absorption in the UV region.

Although radicals may be produced by various photochemical conversion processes like photoscission, abstraction of intramolecular hydrogen, and electron and proton transfer, the most efficient radical initiators developed so far work via bond cleavage [102], for example:

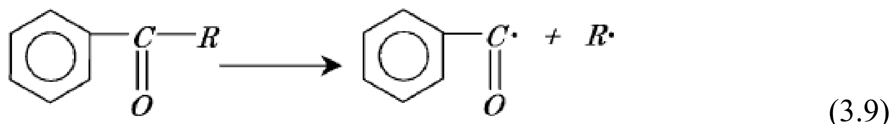

(3.9)

Good reviews of the synthesis, performance, and general research into various radical type photoinitiators can be found in [98, 101].

Cationic photopolymerization is much less used than the radical type. The photoinitiation is generally based on the ring opening of the oxirane group [98-102]:

$$I \xrightarrow{hv} C^{+} \tag{3.10}$$

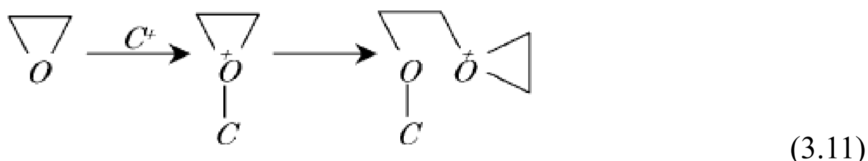

(3.11)

Three classes of molecules are found to be valuable for practical use here: diazonium salts, onium salts and organometallic complexes, about which detailed discussion have been published [98]. Compared to radical type reactions, cationic polymerizations feature (i) low curing speed, (ii) lower viscosity, (iii) small shrinkage after polymerization, and (iv) severe post-irradiation dark polymerization. Sometimes extra thermal processing is needed to increase the conversion of monomers.

After polymerization, the oligomer constitutes the backbone of the polymer network. The physical, chemical and mechanical properties of the solidified resin strictly depend on the nature and structure of the oligomer. Oligomers generally contain at least two reactive groups, from which both cross-linking and polymerization could occur. For example, oligomers possessing two acrylate groups may have many different backbones due to different components of R: polyester, polyurethane, polyether, epoxy, and so forth.

Monomers have a much smaller molecular weight and consist of one or several reactive groups. They polymerize similarly to oligomers and are an important factor in determining the efficiency of polymerization. In addition, monomers are also useful for

diluting resins so that the polymer is easier to handle for a particular use. For 3D micro-nanolithography, a suitable viscosity is of particular importance due to the opposing requirements in different steps of processing: a high viscosity is needed for keeping early produced volumes where they are created; while a low viscosity facilitates removal of unsolidified resin from intervals. Strictly speaking, resin is the oligomers that have a molecular weight ranging from 500 to 3000, and exhibit a viscosity of 5 to 25 Pa·s. In addition to the viscosity, among many, the following behaviors are preferred for a successful fabrication: (i) high polymerization efficiency upon light irradiation, (ii) lower shrinkage after polymerization, (iii) fast reaction time and low dark polymerization.

3.2 Hydrogel materials

Hydrogels, by definition, are three-dimensional cross-linked polymeric networks that can imbibe large amounts of water [104-106]. These materials are generally classified into one of two categories based on their cross-linking chemistry [107]. The first category entails physical gels which are defined as polymeric networks that are bound together via polymer chain entanglement and/or non-covalent interactions that exist between polymer chains [104, 106, 108]. The attractive forces holding these networks together are typically based on hydrogen bonding, electrostatic or hydrophobic interactions and thus, the gels can be reversibly dissolved under certain conditions that would weaken these attractive forces, i.e. a change in pH. In contrast to these weak physically cross-linked networks, the other general class of hydrogels is chemically cross-linked gels. These hydrogels exhibit improved stability due to the formation of covalent bonds between different polymer chains throughout the networks and display endurance with respect to network structure [104, 107, 109]. These gels are commonly

formed through monomer polymerization in the presence of a cross-linking agent, which is typically a monomer with at least two polymerizable functional moieties.

Another area in which hydrogel materials can be categorized is based on gel dimensions. Typically, hydrogels can be categorized as either macrogels or microgels. Macrogels are bulk, monolithic networks that typically range in size from millimeters or greater [110]. Microgels, on the other hand, are defined as colloidally stable, water swellable polymeric networks whose diameter typically ranges from 100 nm to 1 μm [111]. While microgels internally have the same gel structure as their macroscopic version, microgels and macrogels are physically different. Microgel particles have surface to volume ratios that are several orders of magnitude larger than those existing in bulk gels [112]. The synthesis of microgel particles typically involves a nucleation, aggregation and growth mechanism that ultimately results in a non-uniform distribution of polymer chains throughout the network [112]. Macrogels, on the other hand are typically prepared under conditions that result in fairly homogenous structures [112].

Some types of hydrogels can be photopolymerized in vivo and in vitro in the presence of photoinitiators using visible or ultraviolet (UV) light. Photopolymerization is used to convert a liquid monomer or macromer to a hydrogel by free radical polymerization in a fast and controllable manner under ambient or physiological conditions. Photopolymerized hydrogels have been investigated for a number of biomedical applications including prevention of thrombosis [113]; post-operative adhesion formation [114, 115]; drug delivery [116, 117]; coatings for biosensors [118, 119]; and for cell transplantation [120, 121].

Polymerization of monomers using visible or UV irradiation has been thoroughly

investigated. While such systems work well for many applications, they generally cannot be utilized in tissue engineering because most monomers are cytotoxic. As a result, photopolymerizable hydrogels for tissue engineering applications have generally been formed from macromolecular hydrogel precursors. These are water-soluble polymers with two or more reactive groups. Examples of photopolymerizable macromers include PEG acrylate derivatives [122], Polyethylene Glycol (PEG) methacrylate derivatives [123], polyvinyl alcohol (PVA) derivatives [124], and modified polysaccharides such as hyaluronic acid derivatives [125, 126] and dextran methacrylate [127]. Chemical structures of some of the macromers that can be used to form photopolymerizable hydrogels are shown in figure 3.3.

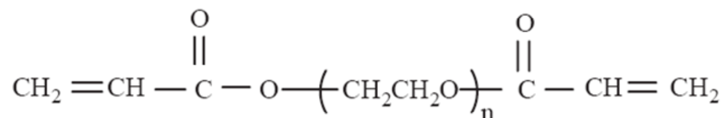

PEG diacrylate

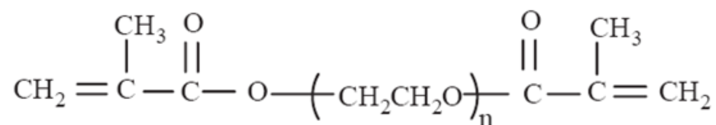

PEG dimethacrylate

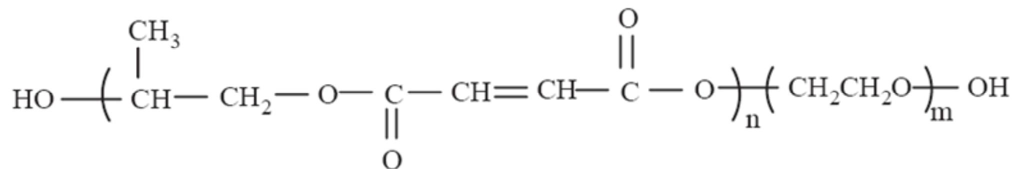

(A) Poly(propylene fumarate-co-ethylene glycol)

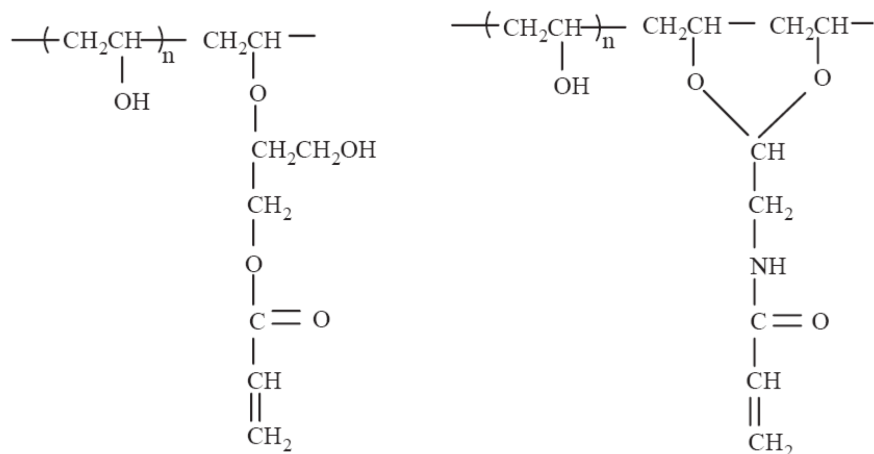

(B) Acrylic modified PVA

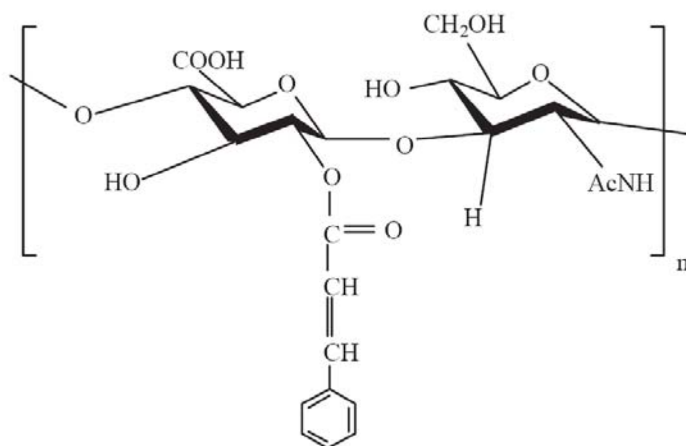

(C) Cinnamated hyaluronic acid

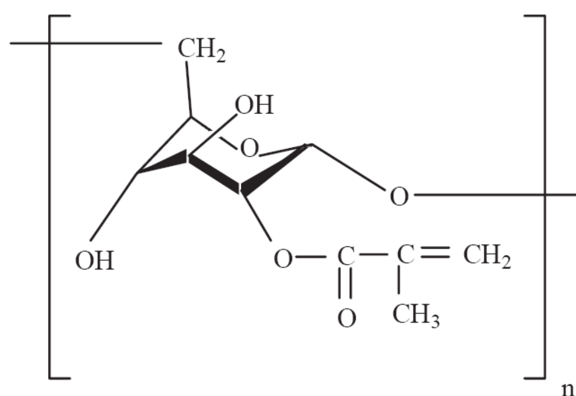

(D) Methacrylate-modified Dextran

Figure 3.3 Chemical structures of materials that can be photopolymerized to create crosslinked

hydrogel networks: (A) PEG diacrylate, methacrylate, and propylene fumarate derivatives, (B) Crosslinkable PVA derivatives, (C) Hyaluronic acid derivatives, (D) Dextranmethacrylate [46].

3.3 Experimental procedures

3.3.1 Materials and sample preparation

3.3.1.1 Materials

The first material used in this work is an acrylate-based photo-polymer. It consists of three basic components: a sensitizer dye, an amine photo-initiator and a multifunctional acrylate monomer. Pentaerythritol triacrylate (PETIA) forms the backbone of the polymer network. N-methyldiethanolamine (MDEA) is used as a photo-initiator and Eosin Y (2-, 4-, 5-, 7--tetrabromofluorescein disodium salt) as sensitizer dye, chemical structures are shown in figure 3.4. This system was developed because of its high sensitivity in the spectral region from 450 to 550 nm and in particular to frequency doubling Nd:YAG laser light (532 nm). Results reported in this doctoral work were obtained with mixtures containing: 0.5% w/w eosin and 1.5% w/w MDEA, with acetone as the developer.

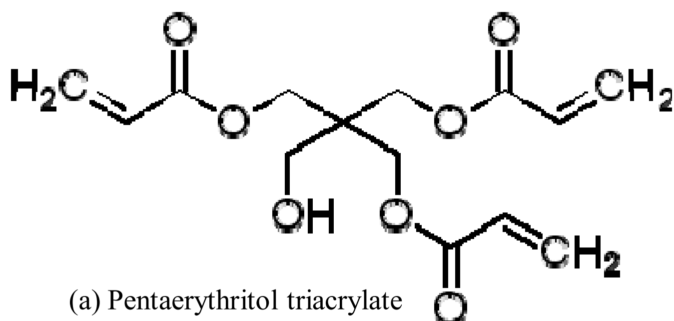

(a) Pentaerythritol triacrylate

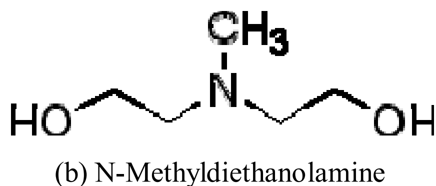

(b) N-Methyldiethanolamine

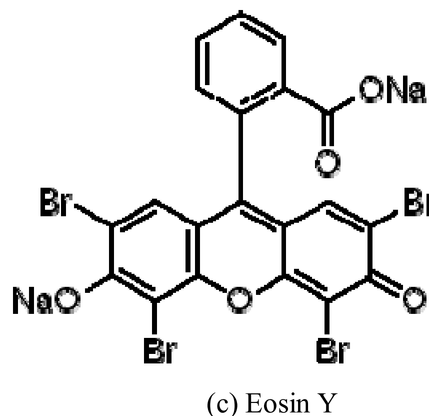

(c) Eosin Y

Figure 3.4 Chemical structures of (a) Pentaerythritol triacrylate, (b) N-Methyldiethanolamine, (c) Eosin Y.

The second photopolymerizable system used in our experiments consisted of three components: (i) Polyethylene Glycol Diacrylate (PEG-DA, molecular weight 600), a hydrophilic and biocompatible hydrogel, purchased from Sartomer, the chemical structure is shown in figure 3.3; (ii) photoinitiator, Camphorquinone (CQ) and an amine 4-N,N-dimethylaminobenzoate (4EDMAB) purchased from Sigma Aldrich: as shown in figure 3.5 which was 1% (w/w) for each; (iii) Eosin Y (2-,4-,5-,7--tetrabromofluorescein disodium salt) as sensitizer dye, 0.5% (w/w). The developer for this system is DI water.

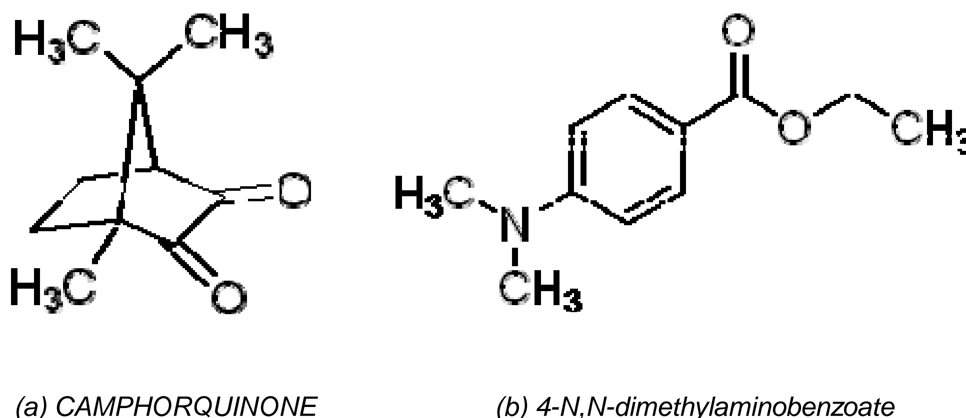

(a) CAMPHORQUINONE *(b) 4-N,N-dimethylaminobenzoate*

Figure 3.5 Chemical structures of photoinitiator system of PEG-DA hydrogel.

3.3.1.2 Sample preparation

Sample surface treatment: Cover glass substrates (18mm x 18mm purchased from Sigma Aldrich) were cleaned by immersion in 20% hydrochloric acid in ethanol for 30 minutes; then they were dipped into 2% 3-aminopropyltriethoxysilane (3APT) acetone solution for 1 minute; and at last, the substrates were dipped in water for 1 minute and air dry.

For 2D microfabrication, materials were deposited as drops on the treated substrates,

and then the substrates were turned over and mounted onto the nanostage. During fabrication, the laser beam was focused firstly through substrates then into the materials. For 3D microfabrication, the substrates were first spin-coated with the same material at 2500 rpm for 30 seconds to get the first layer, and then mounted onto the platform.

3.3.2 Experimental setup and sample characterization

3.3.2.1 Experimental setup

A schematic of the experimental setup for 2D direct-writing is shown in figure 3.6. A beam of frequency doubled CW Nd:YAG laser (Quantronix Model 117), wavelength 532nm, was led into a modified upright microscope (Olympus BX41) and focused onto a three dimensional nanostage with nanometer resolution and 300μm X 300μm X 300 μm work range (PI P-563.3CD, controller E-710.3CD) by a 20X objective lens (OFR LMH-20X-532, NA=0.4, working length=6mm). A mechanical shutter (Uniblitz Electronic VS14, controller: VCM-D1) and the nanostage were controlled by a software, developed in Visual C++, to realize designed pattern. The microscope was equipped a high resolution CCD camera (Sony DXC-190), which can be used for real-time observation. One bandpass filter was installed between transmitted lamp and nanostage avoiding the effect of illuminating light to the photopolymerizable materials, another 532nm wavelength filter was installed in front of the CCD camera to reduce the amount of laser reflection into the CCD camera.

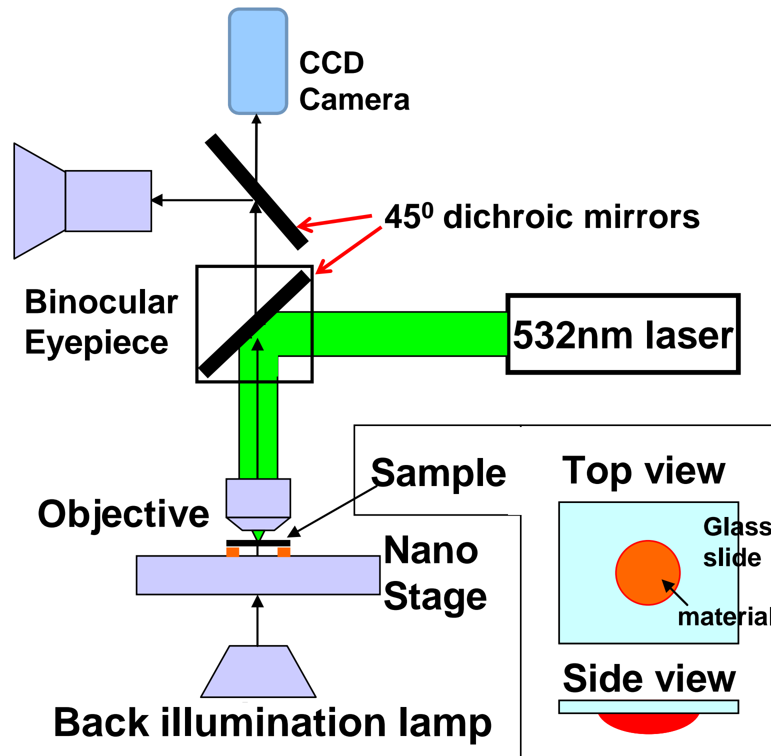

Figure 3.6 Schematic of 2-dimensional direct-writing experimental setup.

Some modifications were made to the setup for 3D fabrication, as shown in figure 3.7. A resin vat was mounted on a z-direction stage in the center of the open frame nanostage. A build platform was fabricated with a transparent PMMA sheet and mounted onto the nanostage. The recoating system was realized by installing a knife edge onto a linear motorized stage. The recoating system was installed onto a four degree-of-freedom (x, y, z and rotation) work platform. The 3D nanostage, optical shutter, and linear motorized stage were all controlled by software, developed in Visual C++, to realize designed 3D patterns. After the contour for a layer was scanned, the build platform was lowered in order to cover the top surface of the build. This is termed the dipping step. After the incomplete prototype was dipped, it was raised above the resin level and the excess resin was swept across it using the knife edge. Sweeping ensures that only a

certain thickness of resin is left on the build to be cured during the next scan. This thickness of material was the same as the desired layer thickness of the part. The recoating and laser-writing processes were repeated until a part was completely finished.

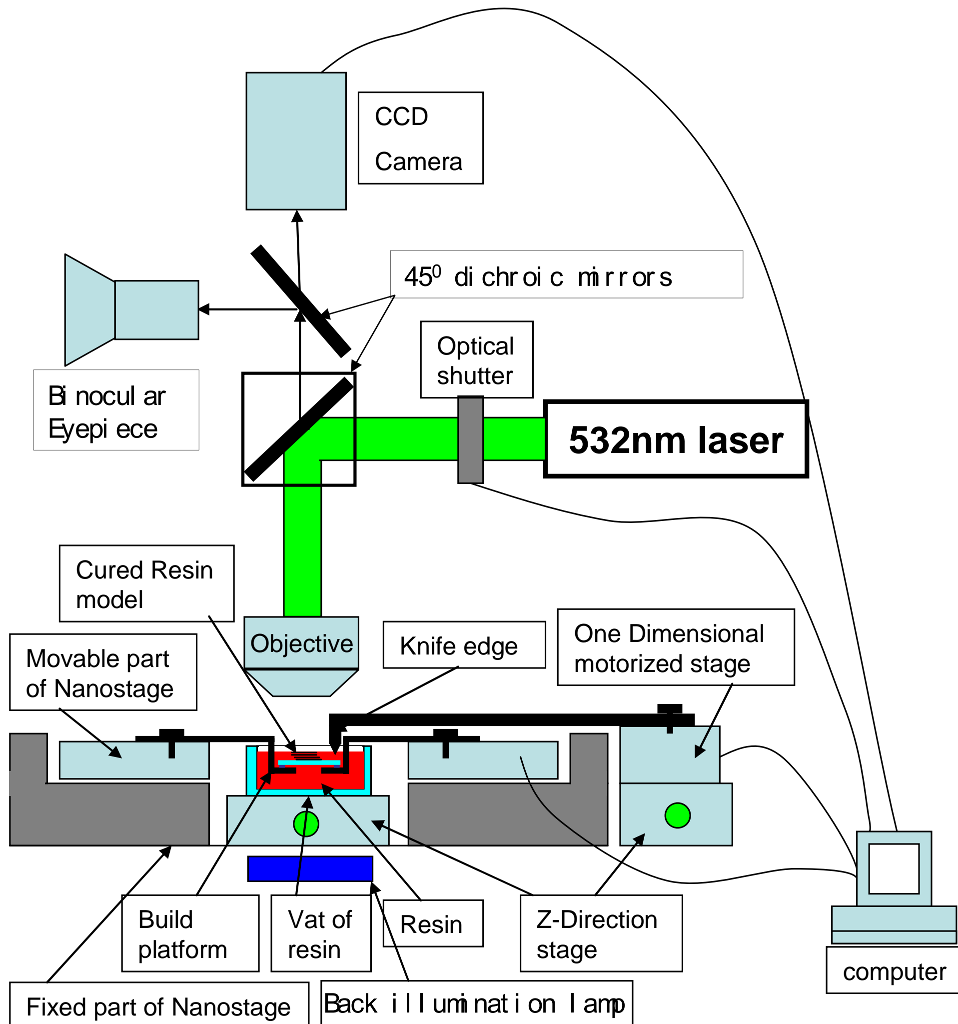

Figure 3.7 Schematic of 3-dimensional direct-writing experimental setup.

3.3.2.2 Sample characterization

All samples were imaged using high-resolution scanning electron microscopes (SEM) with an operating voltage of 10 kV (LEO 1530 and Philips XL30 FEG Thermally-Assisted Field Emission microscope). All samples were coated with 2 nm gold/palladium layer to improve the electrical conductivity, prior to imaging.

A white light interferometer (Zygo PTI 250) was used for measuring the thickness of Hydrogel block patterns; all samples were also coated with 2nm gold/palladium layer to improve the reflection of sample surfaces.

3.4 Theoretical simulation of laser-induced direct-write polymerization

A model based on Monte Carlo method was developed. Some key parameters of the materials were needed to be predicted. The first part of this section provides a method to extract these parameters through experiments. The second part introduces the Monte Carlo simulation for photopolymerization.

3.4.1 Simulation for the width and depth of laser induced polymerization

We consider a Gaussian laser beam, which strikes the interface between the substrate and photopolymerizable material, having semi-infinite thickness and infinite length. The following assumptions were made.

1) The coordinate system is shown in figure 3.8. The x-y plane is coincident with the resin surface, x axis is coincident with the centerline of the scanned laser beam. The z axis is normal to the resin surface, with positive z directed downward in the resin. The origin is selected at the interface of substrate and resin.

2) The laser beam propagation can be described by Gaussian distribution as follows:

$$I(x,y,z) = I_0 e^{\left(-2\frac{x^2+y^2}{w^2}\right)} \tag{3.12}$$

where w is diameter of focused laser beam, I_0 is incident power density at z=0.

The laser power P, which can be measured by laser power meter, is given by:

$$P = \int_{-\infty}^{\infty}\int_{-\infty}^{\infty} I(x,y)dxdy = \int_{-\infty}^{\infty}\int_{-\infty}^{\infty} I_0 \exp\left(-\frac{2(x^2+y^2)}{w^2}\right)dxdy = \frac{\pi}{2}w^2 I_0 \qquad (3.13)$$

So the incident power density at z=0:

$$I_0 = \frac{2}{\pi w^2}P \qquad (3.14)$$

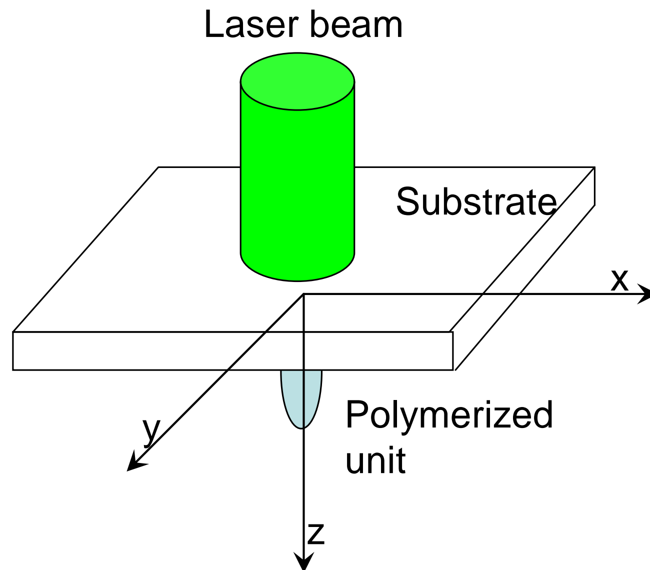

Figure 3.8 Schematic view of single polymerization.

3) The process of a plate of homogeneous and isotropic material absorbing the laser beam can be described by the Beer-Lambert law, which gives the laser power density I at the depth z:

$$I = I_0 \exp(-\alpha z) \qquad (3.15)$$

or laser energy density E at the depth z:

$$E = E_0 \exp(-\alpha z) \qquad (3.16)$$

Where α is spectral absorption coefficient (cm^{-1}) and $1/\alpha$ is the penetration depth D_p.

Consider a laser beam is exposed into resin for a period of T, the exposure energy

density distribution at z=0 can be expressed as

$$E(x,y,0,t)=\int_0^T I(x,y)dt = I_0 T \exp\left(-\frac{2(x^2+y^2)}{w^2}\right) \tag{3.17}$$

From equation 3.16

$$E(x,y,z,t)=E(x,y,0,t)\exp(-\alpha Z) \tag{3.18}$$

For photopolymers, when the exposure is less than a critical value, E_c, the resin remains liquid. When the exposure is greater than E_c, the polymer is at the "gel point" [128], corresponding to the transition from the liquid phase to the solid phase. Thus, we may solve for the locus of points y=y* and z=z*, which are just at the gel point, or equivalently, the outer boundary of that portion of the resin which has been at least partially polymerized.

When $E=E_c$, then y=y* and z=z*, we can get from equation 3.17 and 3.18:

$$E_c=\exp(-\alpha z^*)\cdot\int_0^T I(x,y^*)dt=\exp(-\alpha z^*)\cdot I_0 T\exp\left(-\frac{2(x^2+y^{*2})}{w^2}\right) \tag{3.19}$$

$$z^*=\frac{1}{\alpha}\ln\frac{I_0 T}{E_c}-\frac{2}{\alpha}\frac{(x^2+y^{*2})}{w^2} \tag{3.20}$$

From equation 3.20, since α is positive, then all nonzero value of x and y* must result in reducing the value of z*. Thus it is clear that the largest value of z* will occur when x=y*=0. Then the maximum cure depth is given by

$$z^*=H=\frac{1}{\alpha}\ln\frac{I_0 T}{E_c} \tag{3.21}$$

Since $I_0 T$ is input energy at the origin point and 1/α is the penetration depth of the resin, we can conclude the following statements:

1. The cure depth is proportional to the natural logarithm of the input energy of laser

beam.

2. A semilog plot of cure depth, z*, versus input energy I_0T should be a straight line. This plot is known as the working curve for a given resin.

3. The slope of the working curve is precisely the penetration depth, 1/α, of the resin at the laser wavelength.

4. The value of the input energy at which the cure depth is zero is E_c, the critical input energy of the resin at the laser wavelength.

When z*=0, we can get the maximum cure diameter:

$$2y^* = D = w\sqrt{2\ln\frac{I_0T}{E_c}} \tag{3.22}$$

Consider a Gaussian laser beam being scanned in a straight line at constant velocity V_s, the cure depth of the polymerized line can be achieved by similar way. First the input energy density at origin position:

$$\begin{aligned} E(x,y,0) &= \int_{-\infty}^{\infty} I(x+V_st,y,t,0)dt = \int_{-\infty}^{\infty} I_0 \exp\left(-\frac{2(x+V_st)^2+y^2}{w^2}\right)dt \\ &= I_0\exp\left(-\frac{2y^2}{w^2}\right)\int_{-\infty}^{\infty}\exp\left(-\frac{2(x+V_st)^2}{w^2}\right)dt \end{aligned} \tag{3.23}$$

Assuming:

$$m = x + V_st \tag{3.24}$$

Then

$$dt = \frac{1}{V_s}dm \tag{3.25}$$

Equation 3.23 becomes:

$$E(x,y,0) = \sqrt{\frac{\pi}{2}}\frac{w}{V_s}Io\exp\left(-\frac{2y^2}{w^2}\right) = \sqrt{\frac{2}{\pi}}\frac{P}{wV_s}\exp\left(-\frac{2y^2}{w^2}\right) \tag{3.26}$$

Following the Beer-lambert absorption law:

$$E(x,y,z)=\sqrt{\frac{2}{\pi}}\frac{P}{wV_s}\exp\left(-\frac{2y^2}{w^2}\right)\exp(-\alpha z) \tag{3.27}$$

When E=E_c, then y=y* and z=z*, we can get from equation 3.26 and 3.27:

$$E_c=\sqrt{\frac{2}{\pi}}\frac{P}{wV_s}\exp\left(-\frac{2y^{*2}}{w^2}\right)\exp(-\alpha z^*) \tag{3.28}$$

When y*=0， we can get the cure depth of polymerized line:

$$z^*=H=\frac{1}{\alpha}\ln\frac{P\sqrt{\frac{2}{\pi}}}{E_c wV_s} \tag{3.29}$$

And when z*=0, we can get the cure width:

$$2y^*=W=w\sqrt{2\ln\frac{P\sqrt{2/\pi}}{E_c wV}} \tag{3.30}$$

A schematic of the parabolic cure profile is shown in figure 3.9

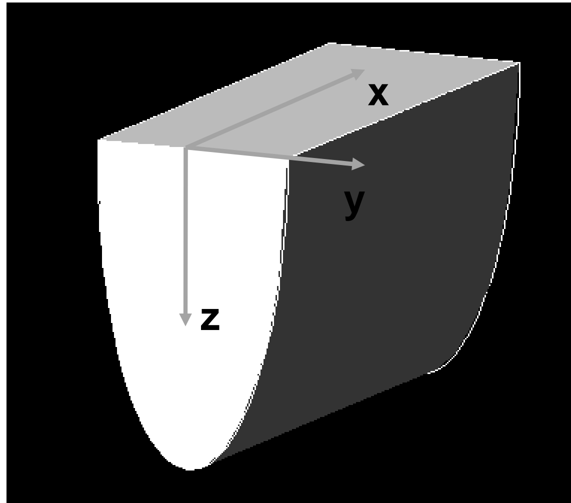

Figure 3.9 Schematic cure profile fabricated by a moving Gaussian laser beam.

3.4.2 Monte Carlo method for single-shot exposure polymerization

The Monte Carlo (MC) method is a statistical simulation technique whose particle

transport capabilities have progressed into many different areas of application since its introduction in the 1940s [129]. Applications of MC techniques in medical physics have been discussed in numerous publications [130, 131] and have been demonstrated and accepted as the most accurate method for radiotherapy dose calculations. The MC technique involves using known probability distributions that govern the physical interactions of photons and electrons in various materials to simulate random trajectories of individual particles. By keeping track of processes of interest for a large number of histories, information regarding the average quantities and their correlated distributions can be obtained as well as the statistical fluctuations of specific events.

Presented here is a model of a photon Monte Carlo method to investigate the detailed microscale optical scattering, and polymerization. The Monte Carlo method is necessarily statistical and therefore requires significant computation time to achieve precision. In the simplified model, the following variance reduction technique is used to reduce computational time. Instead of propagating photons individually, a photon packet with a specific weight is created. As the photon interacts in the resin, it will deposit weight due to absorption and the remaining weight will be scattered to other parts of the resin. Each photon packet will repeatedly undergo the following numbered steps until it terminates. The flow chart is shown in figure 3.10. The simulation process includes 4 steps:

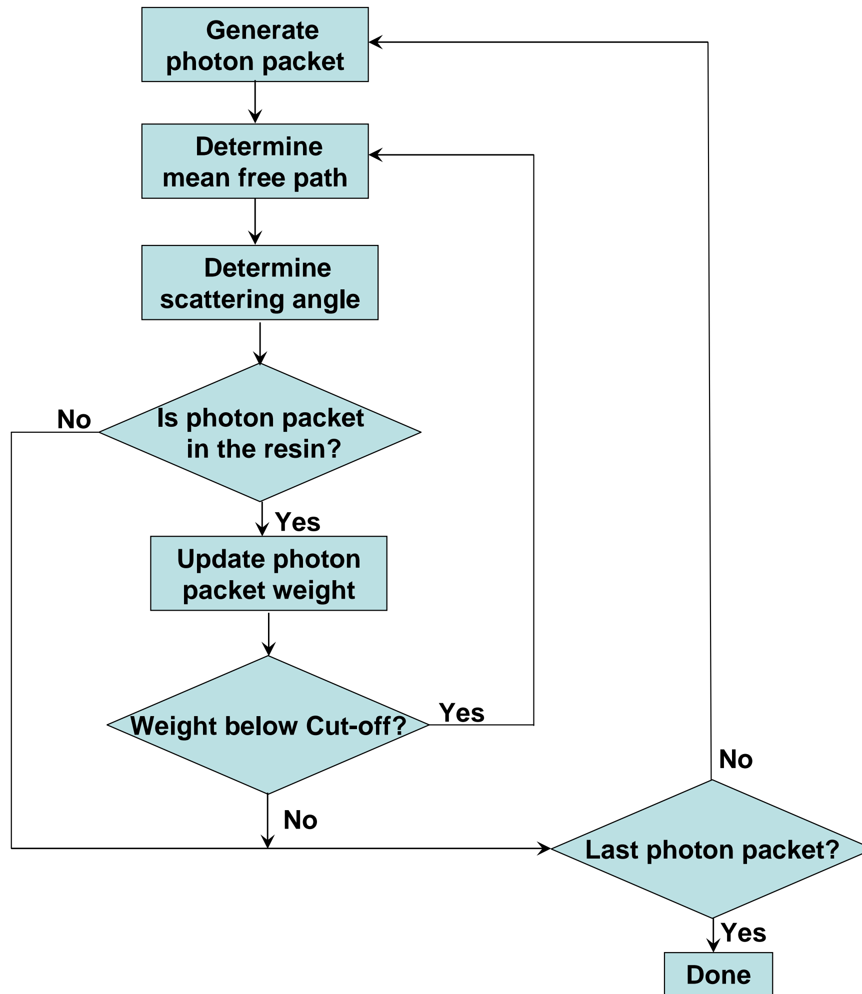

Figure 3.10 Flow chart of the Monte Carlo simulation.

3.4.2.1 Photon packet generation

To generate a photon packet, the initial position of the photon packet, the initial direction, as well as the photon packet weight is needed to set. It is convenient to use a global coordinate system. Three Cartesian coordinates are used to determine the photon packet position, along with three direction cosines to determine the direction of propagation. The initial start conditions will vary based on the laser energy distribution. For Gaussian laser beams, there are two ways to generate random samples: the first way is to initiate the position of photon packet with random sampling from Gaussian

distribution and set the entire photon packet with the same weight, as following:

$$\begin{cases} R = randn \cdot w_0 \\ \varphi = rand \cdot 2\pi \\ x = R\cos\varphi \\ y = R\sin\varphi \\ weight = 1 \end{cases} \tag{3.31}$$

where randn: generating a random number with Gaussian distribution;

rand: generating a uniformly distributed random number;

w_0: the radius of the laser beam at initial position.

The second way is to initiate the position of photon packet with uniform random sample and set the weight of photon packet with Gaussian distribution, as following:

$$\begin{cases} R = rand \cdot w_0 \\ \varphi = rand \cdot 2\pi \\ x = R\cos\varphi \\ y = R\sin\varphi \\ weight = \exp(-2R^2 / w_0^2) \end{cases} \tag{3.32}$$

Figure 3.11 shows the scheme of input photon packet. The x'-y' plane is the surface of resin, x-y plane is the output plane of objective lens, WL is the working length of the objective lens. When a photon packet is emitted from position A and focused to O' with angle α_1 between Z axes, due to refraction in the resin, the angle will change to α_2. The reversing extension line intersects the x-y plane at R. So the three direction cosines can be expressed as:

$$(U,V,W) = \left(\frac{R\cos\phi}{\sqrt{WL^2 + R^2}}, \frac{R\sin\phi}{\sqrt{WL^2 + R^2}}, \alpha_2 \right) \tag{3.33}$$

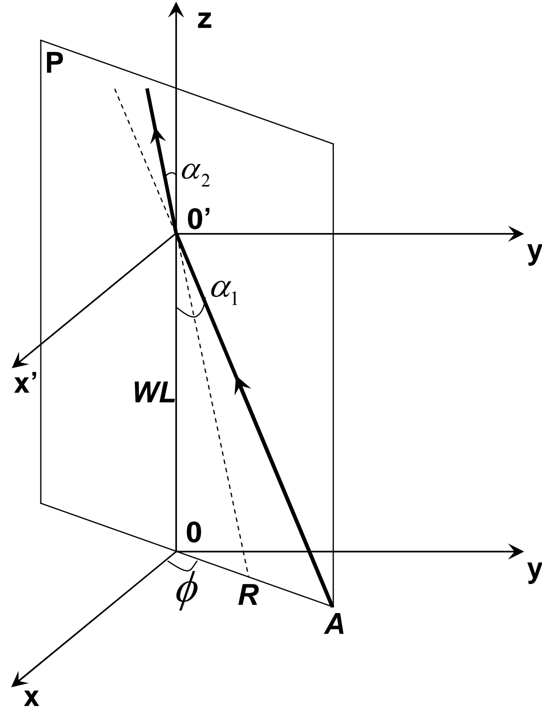

Figure 3.11 Schematic of the direction of input photon packet.

3.4.2.2 Mean free path

The mean path length between successive interactions is called mean free path. There are a variety of methods for step size selection. Below is a basic form of photon step size selection [132]:

$$L = -\frac{\ln \xi}{\mu_t} \tag{3.34}$$

$$\mu_t = \mu_a + \mu_s \tag{3.35}$$

where $0<\xi<1$ is a uniformly distributed random number, μ_a and μ_s are absorption and scattering coefficients, and μ_t is the total attenuation coefficient. This formulation generates an exponential distribution of interaction path lengths.

3.4.2.3 Photon packet scattering and weight update

A portion of the photon weight is absorbed at each interaction site. This fraction of the weight is determined as follows:

$$\Delta weight = weight \cdot \frac{\mu_a}{\mu_t} \tag{3.36}$$

The weight fraction can then be recorded in an array. The weight of the photon packet must then be updated as follows:

$$weight = weight - \Delta weight = weight \cdot \frac{\mu_s}{\mu_t} \tag{3.37}$$

Following absorption, the photon packet is scattered. The weighted average of the cosine of the photon scattering angle is known as scattering anisotropy (g), which has a value between -1 and 1. If the optical anisotropy is 0, this generally indicates that the scattering is isotropic. If g approaches a value of 1 this indicates that the scattering is primarily in the forward direction. In order to determine the new direction of the photon packet (and hence the photon direction cosines), we need to know the scattering phase function. Often the Henyey-Greenstein phase function is used.

$$B(\mu) = (\mu_s / \mu_t)(1-\mu^2)(1+\mu^2 - 2g\mu)^{-3/2} \tag{3.38}$$

where $\mu = \cos\theta$, θ is the scattering angle, and $g = \overline{\mu}$, the mean value of $\cos\theta$.

Then the scattering angle, θ, is determined using the following formula.

$$\left.\begin{array}{ll} \cos\theta = 2\xi - 1 & g = 0 \\ \cos\theta = \left[(1+g^2) - (1-g^2)^2(1-g+2g\xi)^{-2}\right] / (2g) & g \neq 0 \end{array}\right\} \tag{3.39}$$

And, the azimuthal angle φ is generally assumed to be uniformly distributed between 0 and 2π. Based on this assumption, we can set:

$$\varphi = 2\pi\xi \tag{3.40}$$

Based on these angles and the original direction cosines, we can find a new set of direction cosines. The new propagation direction can be represented in the global coordinate system as follows:

$$\begin{cases} U' = \sin\theta(UW\cos\varphi - V\sin\varphi)(1-W^2)^{-1/2} + U\cos\theta \\ V' = \sin\theta(VW\cos\varphi - U\sin\varphi)(1-W^2)^{-1/2} + V\cos\theta \\ W' = -(1-W^2)^{1/2}\sin\theta\cos\varphi + W\cos\theta \end{cases} \tag{3.41}$$

3.4.2.4 Photon packet termination

If a photon packet has experienced many interactions, the weight left in the packet is of little consequence. As a result it is necessary to determine a means for terminating photon packets of sufficiently small weight. A simple method would use a threshold, $Weight_{door}$, and if the weight of the photon packet is below the threshold, the packet is considered dead. The aforementioned method is limited as it does not conserve energy. To keep total energy constant, a Russian roulette technique is often employed for photons below a certain weight threshold. This technique uses a roulette constant m to determine whether or not the photon will survive. The photon packet has one chance in m to survive, in which case it will be given a new weight of m*Weight where "Weight" is the initial weight (this new weight, on average, conserves energy). All other times, the photon weight is set to 0 and the photon is terminated. This is expressed mathematically below:

$$Weight_{door} \leq \frac{E_c}{N} \tag{3.42}$$

$$Weight_{survive} = \begin{cases} mWeight_{door} & \xi \leq 1/m \\ 0 & \xi > 1/m \end{cases} \tag{3.43}$$

3.5 Experimental results and discussion

Materials parameters were firstly measured through experiments and the theoretical models were validated by comparing with these data. Some 2D and 3D patterns were then fabricated to show the fabrication ability.

3.5.1 Experimental determination of material parameters and model validation

Critical exposure, E_c, and penetration depth, $1/\alpha$ are two key parameters for modeling a laser direct-write polymerization using a given wavelength. From the statements of equation 3.21 in section 3.4.1, a semilog plot of cure depth, z*, versus input energy $I_0 T$ should be a straight line. This plot is known as the working curve for a given resin at a given wavelength. The slope of the working curve is the penetration depth, $1/\alpha$, of the resin and the value of the input energy at which the cure depth is zero is E_c, the critical input energy of the resin at the laser wavelength. Experiments are designed to get the working curve for each material. These experiments are described in the following sections.

3.5.1.1 PETIA

As mentioned earlier, PETIA is multifunctional acrylate- based photo-polymer with sub-microm resolution. Single exposure dots could be fabricated with different laser powers and exposed times, as shown in figure 3.12. A glass substrate coated with PETIA was turned over and mounted onto the nanostage. The optical shutter was used to control the exposure time and a round continuously variable neutral density filter was used to adjust laser power. Figure 3.13 shows the fabricated pattern of dots. Each pattern contains 10 rows and 10 columns of dots fabricated with same laser power. Each row containing

10 dots was fabricated with same exposure time, allowing repeat measurement and computation of average dot size. A total of 30 patterns were fabricated and measured, yielding 300 data points.

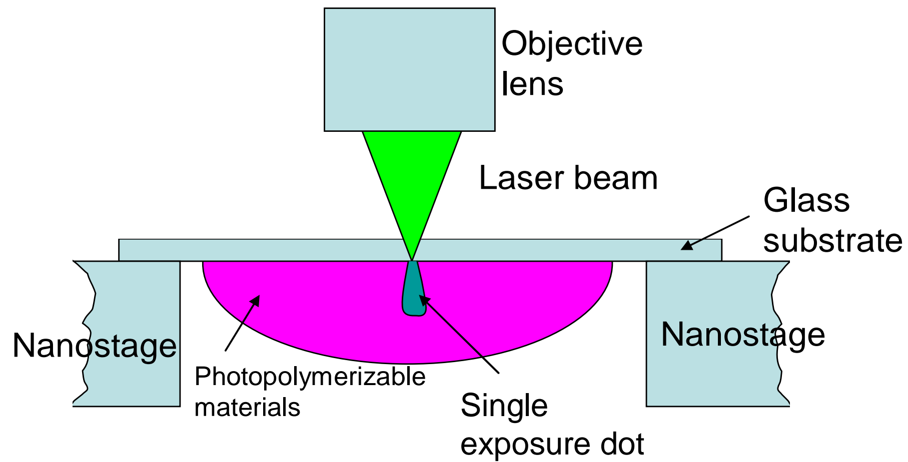

Figure 3.12 Schematic diagram of experimental design for single exposed dots.

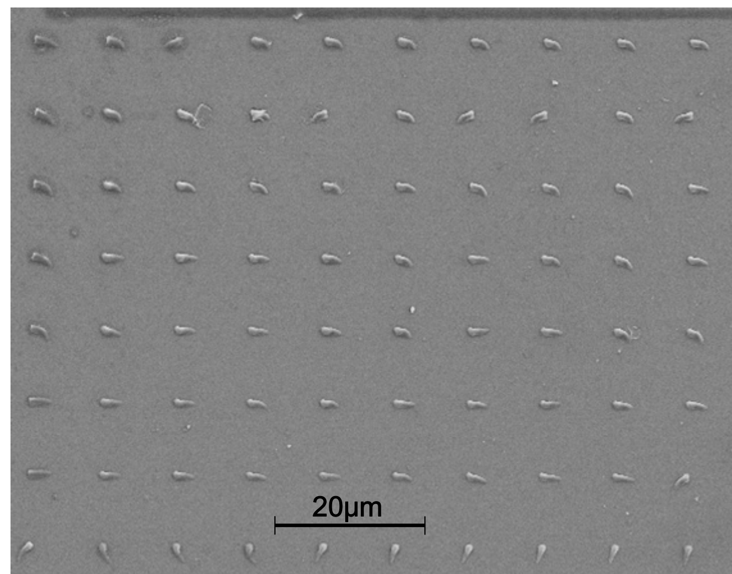

Figure 3.13 SEM pictures of single exposed dots for PETIA.

Cure width and depth of the dots were measured using measuring function in the

scanning electron microscope controlling software. The deviations for a row of dots which were fabricated with same parameters were observed less than 0.1. Figure 3.14 shows experimentally measured working curve for PETIA at 530nm laser exposure. This figure is a semilogarithmic plot; with cure depth on the ordinate and the logarithm of the input laser fluence on the abscissa. It is evident from inspection of figure 3.14 that cured depth is indeed directly proportional to the logarithm of the input fluence, as indicated by the fact that the experimental data conform very closely to a straight line. Least squares fit method was used to simulate the difference between experimental data and the fitting line, a correlation of 0.9 was achieved. The slope corresponds to the value of the resin penetration depth:

$$\mathbf{D_p=1/\alpha=5.452\ \mu m}$$

The straight line trend of the data shows an abscissa intercept, which is the critical laser input fluence:

$$\mathbf{E_C=0.0695\ J/cm^2}$$

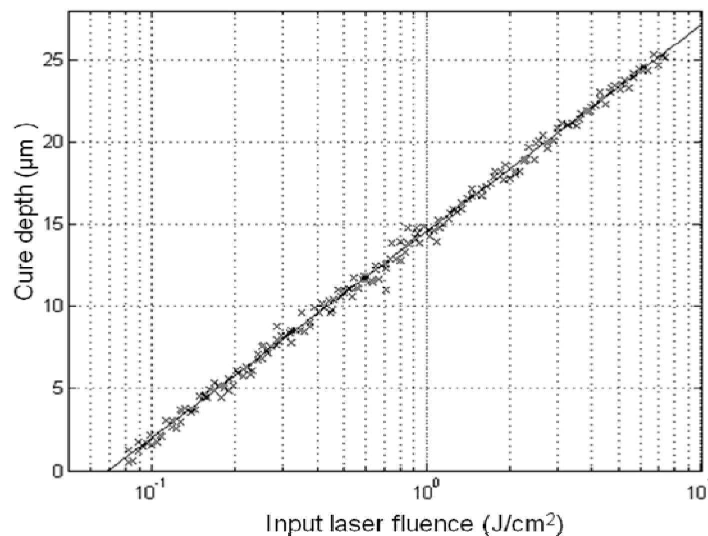

Figure 3.14 Experimentally measured working curve for PETIA at 532nm laser exposure.

From equation 3.22, the cure width C_w can be expressed as a function of the focused beam diameter w, the cure depth C_d, and penetration depth D_p as:

$$C_w = 2w\sqrt{C_d / 2D_p} \quad (3.44)$$

A comparison of theoretical model and experimental data is shown in figure 3.15. The experimental data is in agreement with the model, with a correlation of 0.85.

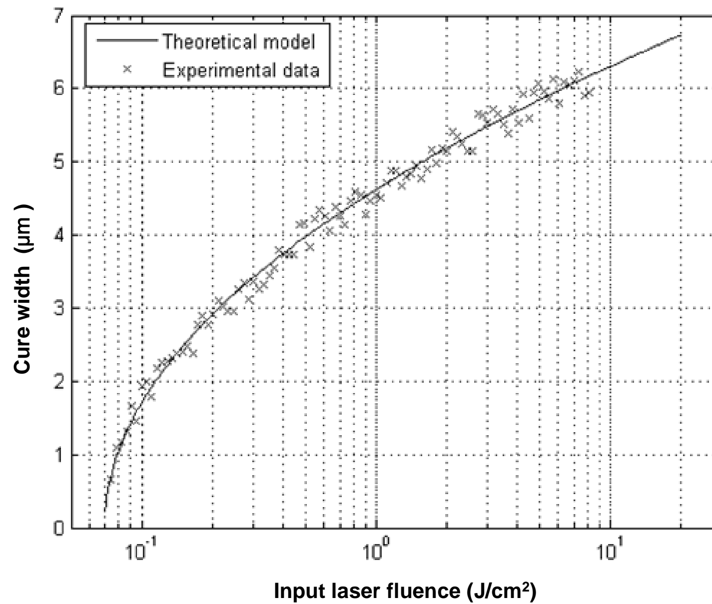

Figure 3.15 Experimentally measured cure width vs. laser fluence for PETIA at 532nm laser exposure.

With the data achieved from the working curve, a simulation program based on Monte Carlo method was developed using MATLAB software. One million photon packets were generated and initiated for each simulation. Figure 3.16 (a) shows simulation results of laser input power and exposure time, from inside to outside: (1) 280 µw for 20 ms; (2) 400 µw for 50 ms; (3) 720µw for 70ms. A comparison of Monte Carlo simulation results and experimental working curve is shown in figure 3.16 (b). Most of the Monte Carlo simulation results are bigger than the experimental results by 8-11%. From the least squares fit line of computational experiment results (the dashed line), the abscissa intercept is approximately the same as working curve, but the slope corresponds

to the value of the resin penetration depth is 5% larger than working curve. One possible explanation involves the material shrinkage. During the 2D and 3D fabrication of PETIA, 10%-15% shrinkage rate was observed. The working curve was obtained by fitting a line through experimentally measured cured depths. These measurements were made after the polymer had experienced shrinkage. For the Monte Carlo method, we only tracked the photon packet and obtained the average quantities and their correlated distributions as well as the statistical fluctuations of specific events, material shrinkage was not considered in the program.

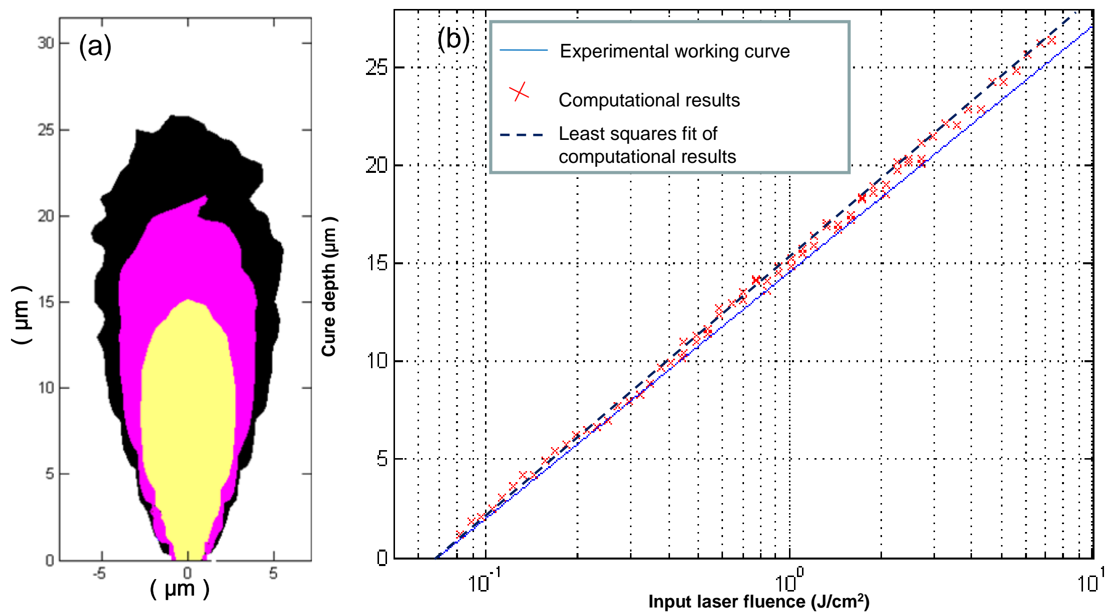

Figure 3.16 Monte Carlo simulation results (a) simulated polymerization with different input laser powers and exposure time, Laser input power and exposure time, from inside to outside: (1) 280 μw for 20 ms; (2) 400 μw for 50 ms; (3) 720μw for 70ms. (b) Comparison of Monte Carol simulation results with experimental working curve.

3.5.1.2 PEG-DA (600)

PEG-DA (600) is a biocompatible hydrogel material which can be used for a number of biomedical applications including prevention of thrombosis [113]; post-operative adhesion formation [114, 115]; drug delivery [116, 117]; coatings for biosensors [118,

119]; and for cell transplantation [120, 121]. Due to the difference of mechanical property, single-shot exposure dots of PEG-DA can not properly stay attached to the glass substrate after developing. The following experimental procedure was designed for PEG-DA. The samples preparation was the same as for PETIA shown in figure 3.12. Exposure time was adjusted by varying the scanning speed of the nanostage, instead of adjusting optical shutter. A schematic of the fabrication scan pattern is shown in figure 3.17. The arrow lines are scanning direction with shutter opened and the dashed lines are the scanning direction with shutter closed. A total of 100 patterns, with size of 100μm X 100μm, were fabricated with different laser powers and scanning speeds. Examples of such patterns are shown in figure 3.18. The thicknesses of the patterns were measured with a white light interferometer which has the resolution of 0.1nm.

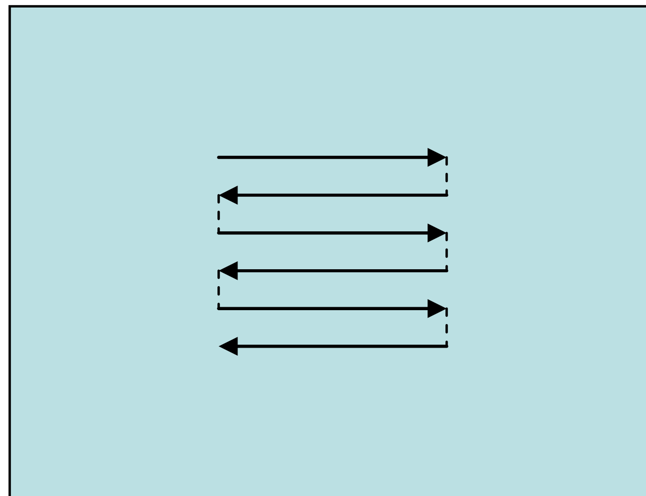

Figure 3.17 Schematic diagram of experimental design for PEG-DA.

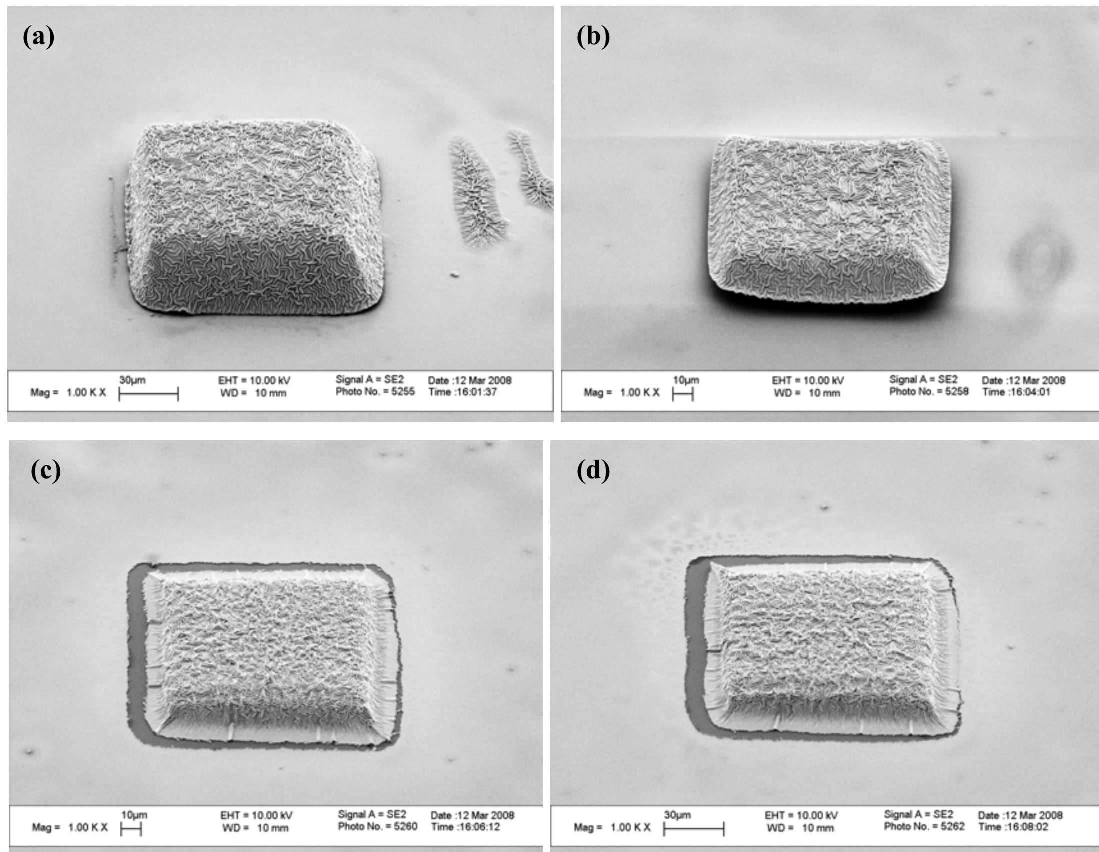

Figure 3.18 SEM micrographs of PEG-DA block exposed by different energy density. (a) 100 J/cm^2 (b) 40 J/cm^2 (c) 18 J/cm^2 (d) 9 J/cm^2

Figure 3.19 shows the experimentally measured working curve for PEG-DA at 532nm laser exposure. Similar to the PETIA working curve, this figure is a semilogarithmic plot; with cure depth on the ordinate and the logarithm of the input laser fluence on the abscissa. The experimental data conform very closely to a straight line. The slope corresponds to the value of the resin penetration depth:

$$\mathbf{D_p=1/\alpha=17.53\ \mu m}$$

The straight line trend of the data shows an abscissa intercept, which is the critical laser input fluence:

$$\mathbf{E_C=7.83\ J/cm^2}$$

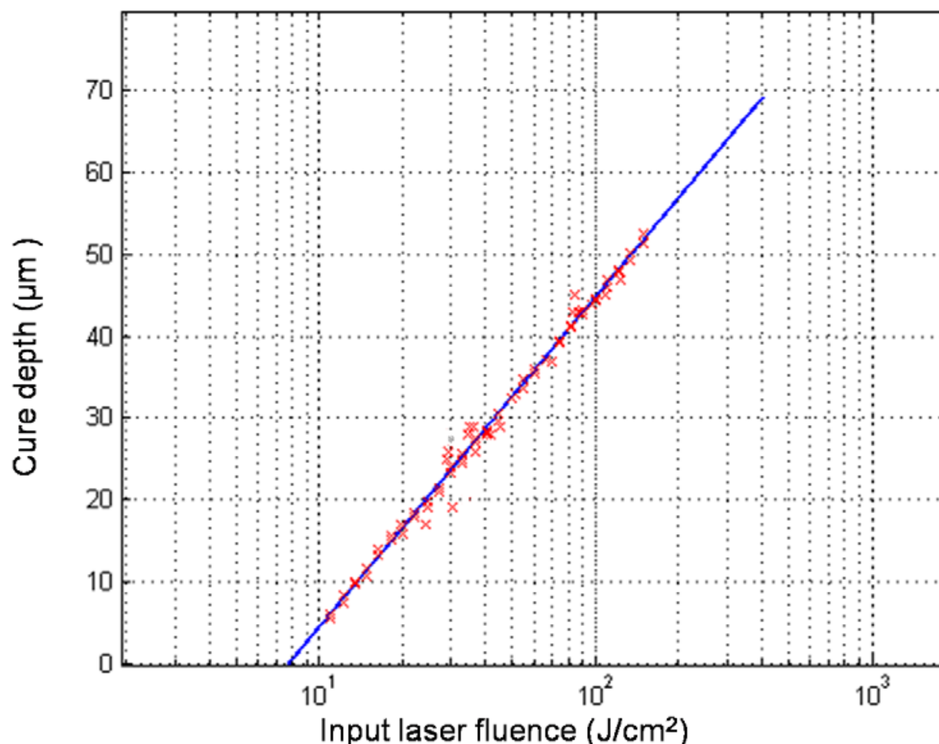

Figure 3.19 Experimentally measured working curve for PEG-DA (600) at 532nm laser exposure.

3.5.2 Direct-write fabrication of cellular structures in PETIA

Cellular polymer structures have been highlighted in the bio-testing area. They are typically used for patterning of proteins and cells [133], topographical control of cells [134-136], and force measurements in cells [137, 138]. In particular, 3D cellular arrangements in 3D polymer scaffolds can provide physiological microstructures for tissue engineering and diagnostic applications [134, 136].

Laser direct-write microfabrication technology is favored in patterning cellular polymer structures because of its straightforward processes and the ability to realize arbitrary shape designs. Microfabrication of square- cellular and circular-cellular structures with PETIA was investigated. Square-cellular structures with different periods,

wall widths and wall heights were designed for different applications. Figure 3.20 shows square-cellular structures with period of (a) and (b) 25μm, (c) and (d) 10μm, and (e) 8μm. The smallest wall width is 840nm. Figure 3.21 shows square-cellular structures with wall height of (a) 0.8μm, (b) 1.5μm, (c) 2μm, (d) 2.5μm, (e) 4μm and (f) 7μm.

For moving Gaussian laser beam, the cure depth and width can be expressed as equations 3.19, 3.20. In the equations,

$$E_{input} = \sqrt{\frac{2}{\pi}} P \Big/ wV \tag{3.45}$$

Subsequently, equations 3.19 and 3.20 can be modified to the same expressions as single-shot exposure working curve equations. The comparisons of cured line depth and line width are shown in figures 3.23 and 3.24. From these figures it can be seen the models are in excellent agreement with experimental results, with a maximum deviation of approximately 10%.

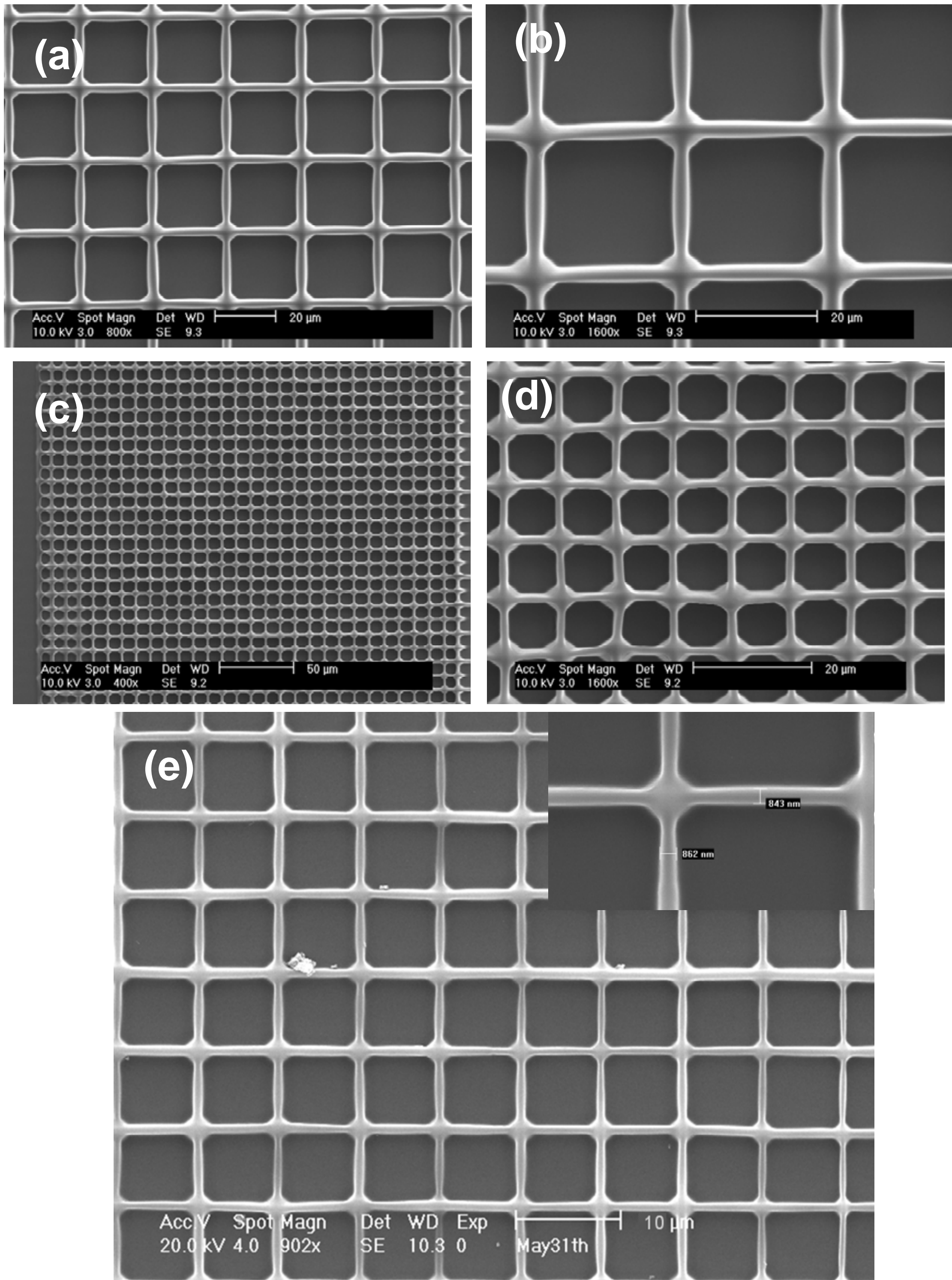

Figure 3.20 Direct-write fabrication of square-cellular structures, wall width and period investigation: fabrication area: 300μmx300μm (a), (b) period: 25μm, wall width: 2μm; (c), (d) period: 10μm, wall width: 2μm; (e) period: 8μm, wall width: 840nm.

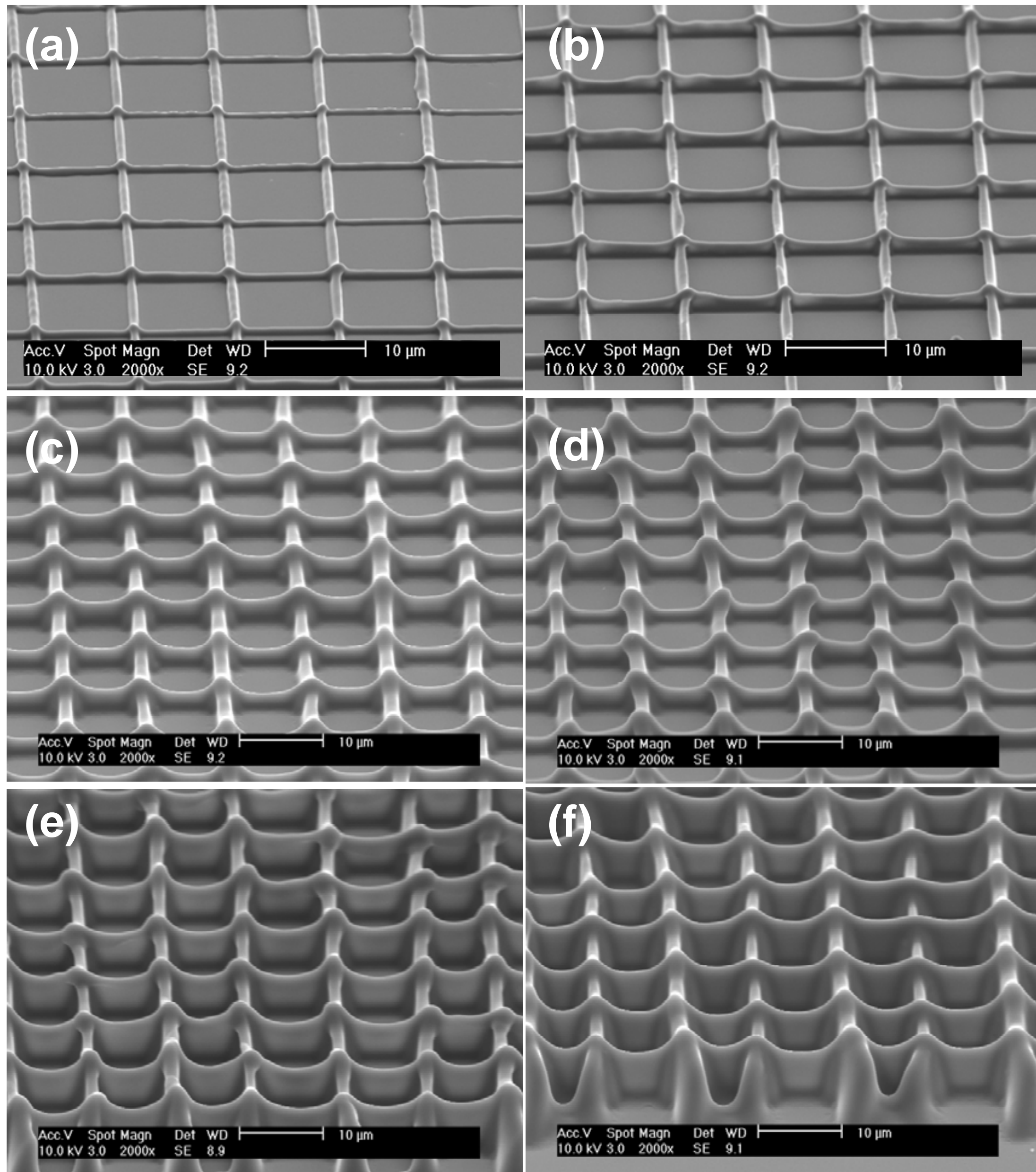

Figure 3.21 Direct-write fabrication of square-cellular structures, wall height investigation: period: 10μm, area: 300μmx300μm (a) wall height: 0.8μm; (b) wall height: 1.5μm; (c) wall height: 2μm; (d) wall height: 2.5μm; (e) wall height: 4μm; (f) wall height: 7μm.

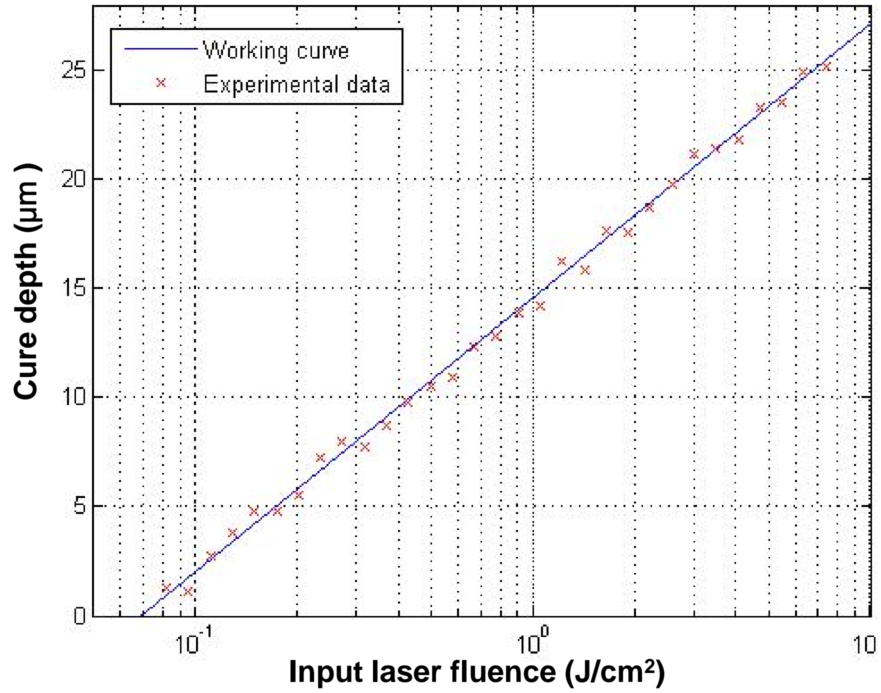

Figure 3.22 Comparison of cure line depth measurement results with experimental working curve.

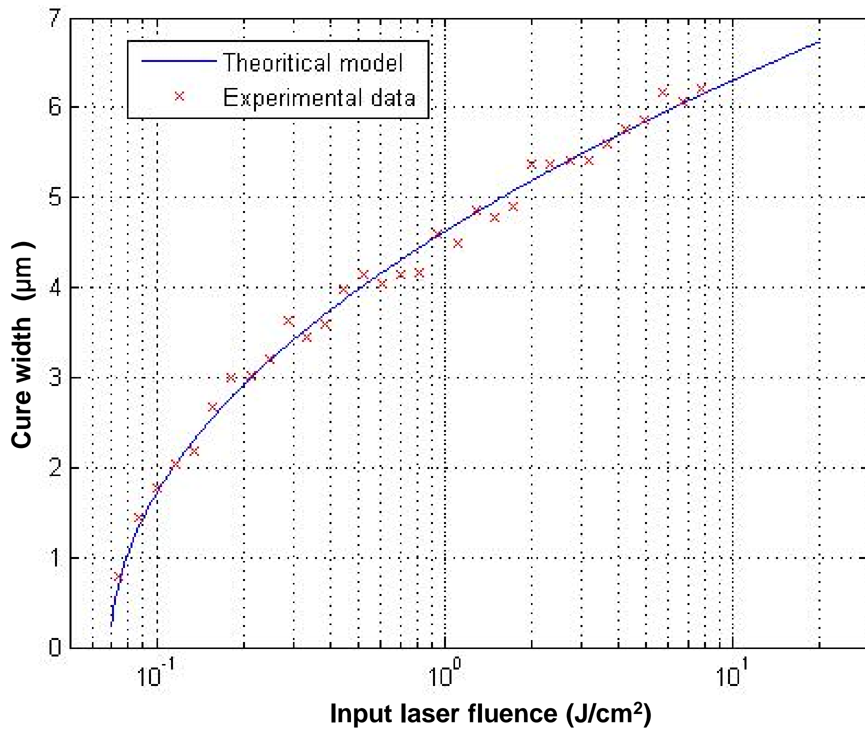

Figure 3.23 Comparison of cure line width measurement results with experimental working curve.

For microfabrication of cellular structures with arbitrary shapes, the structures were

firstly designed in AutoCAD (Autodesk inc. The design files were imported by a control software developed with Visual C++. The control software generated and sent the motion control commands to the nanostage, the laser modulation commands to the optical shutter, and material delivery commands to a knife edge to realize the designed cellular structures. Figure 3.24 (a) shows the AutoCAD model of circular-cellular structures composed of 5 layers, and figure 3.24 (b) shows the developed circular-cellular structures fabricated with PETIA. The scanning speed was 20μm/s. Raster scanning path was used for each layer fabrication followed with contour scanning. It took 3 minutes to fabricate a 5μm thick layer and 16 minutes for the total fabrication.

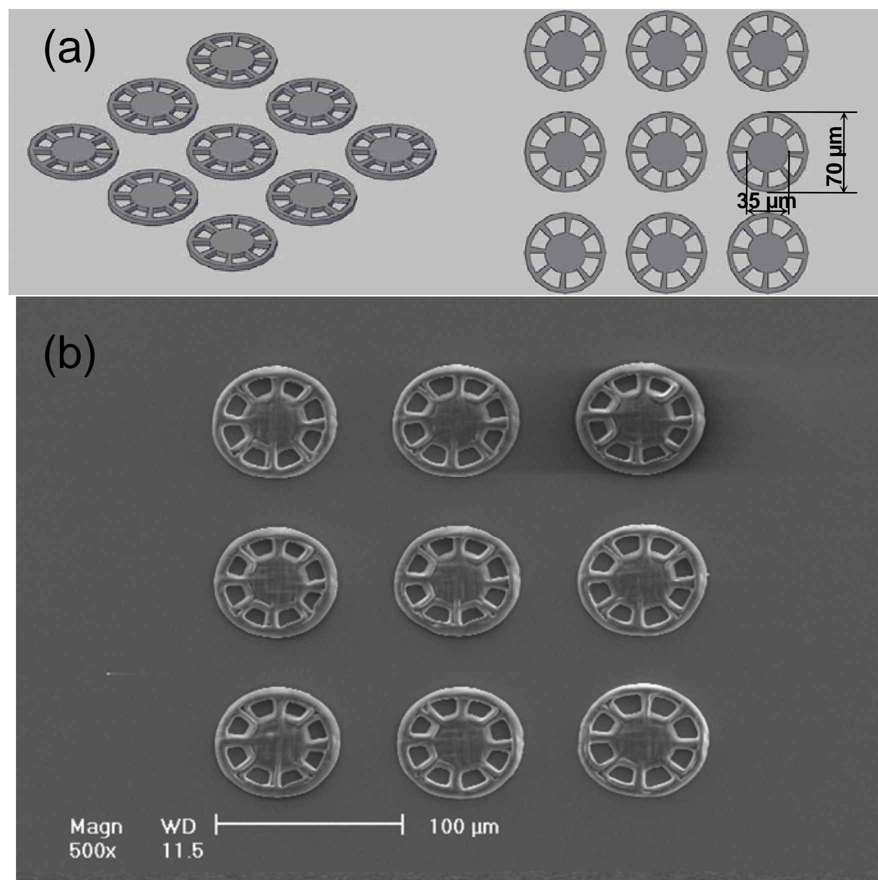

Figure 3.24 Direct-write fabrication of multiple-layer circular-cellular structures, laser power 70nw, scanning speed: 100μm/s.

3.5.3 Direct-writing of biocompatible photo-crosslinkable hydrogels

Poly (ethylene glycol) diacrylate (PEG-DA) is an exceptional polymer with excellent properties and widespread use in biomaterials, biotechnology, and medicine [139]. It is biocompatible, nontoxic, non-immunogenic, hydrophilic, and can be chemically cross-linked into hydrogel [140]. PEG-DA hydrogel cellular structures have been widely used for many applications [140]. One of these applications is their use as immunoprotective barriers in tissue engineering for therapeutic cell transplantation to prevent the rejection of transplanted cells by the immune system of the host. In order for an immunoprotective barrier to maintain cell viability and function, while at the same time prevent immune rejection, it must be permeable to small molecules (e.g., oxygen, nutrients, and waste products) and the therapeutic substance, but must exclude large molecules such as the components of the immune system. Two critical factors that determine the success of immunoprotective devices are the thickness and permeability of the wall of cellular structures.

Figure 3.25 shows biocompatible hydrogel square-cellular structures fabricated with PEG-DA (600), the thicknesses of the cellular wall and the input laser fluences are (a) 3μm, 18J/cm^2; (b) 4μm, 32 J/cm^2; (c) 5μm, 42 J/cm^2. Figure 3.26 shows PEG-DA hexagonal honeycomb structures fabricated with 70 J/cm^2 input laser fluence, the thickness of the cellular wall is 5.2μm.

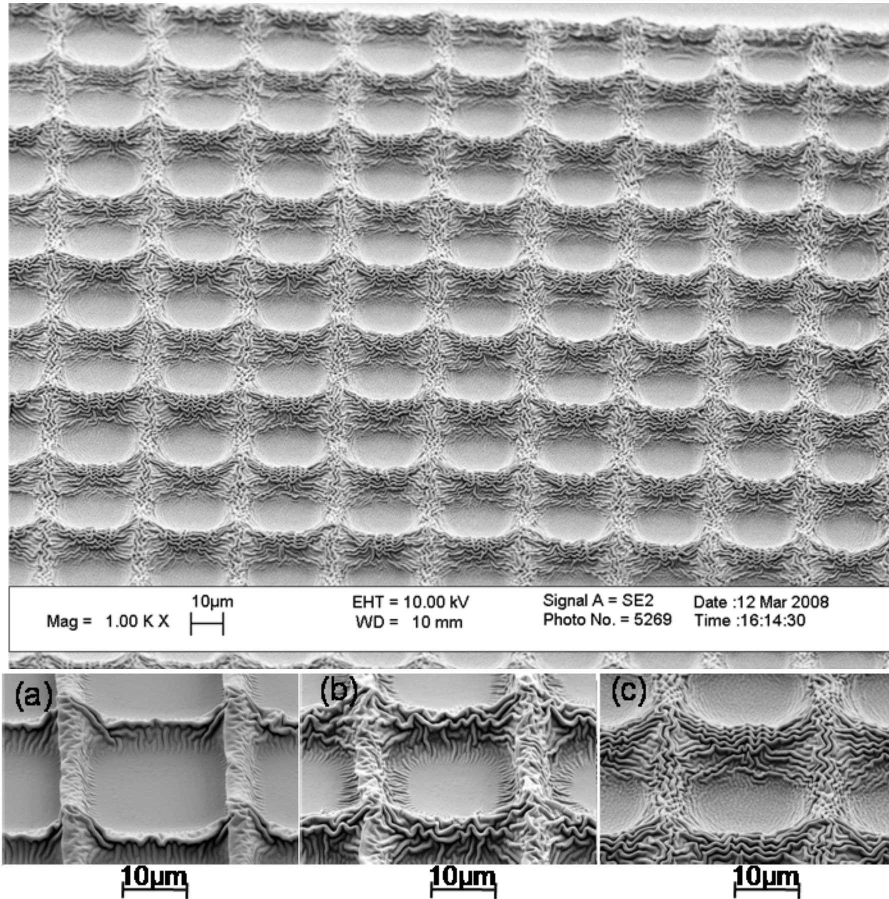

Figure 3.25 Direct-write fabrication of biocompatible hydrogel square-cellular structures with input laser fluence of (a) 18J/cm^2; (b) 32 J/cm^2; (c)42 J/cm^2.

From equation 3.44, the cure width C_w can be expressed as a function of the focused beam diameter w, the cure depth C_d, and penetration depth D_p. With working curve obtained in section 3.5.1.2, a theoretical model line can be achieved as shown in figure 3.27. By measuring the wall widths of these square-cellular and honeycomb structures, fabricated by different input laser fluence, we can compare these experimental data with the theoretical model.

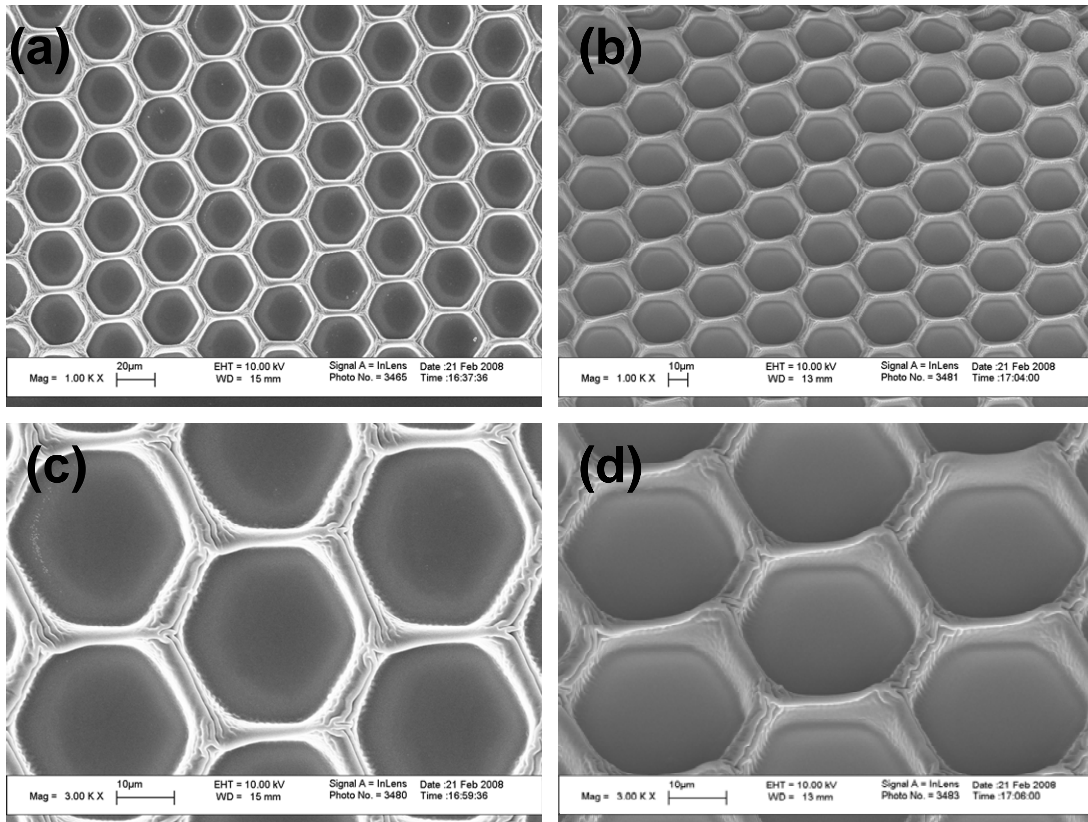

Figure 3.26 Direct-write fabrication of biocompatible hydrogel hexagonal honeycomb structures.

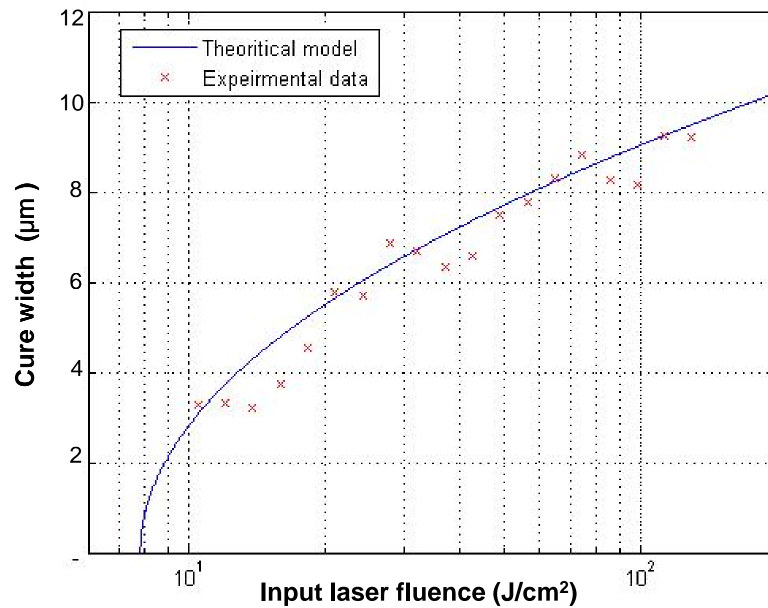

Figure 3.27 Experimentally measured cure width vs. laser fluence for PEG-DA (600) at 532nm laser exposure.

3.6 Summary and Conclusions

In this chapter, direct-write laser photopolymerization was investigated. A sub-micrometer resolution direct-write polymerization system was developed. This system included a frequency-doubled Nd:YAG laser, beam delivery system, optical shutter, three-dimensional nanostage, material recoating system, and monitoring system. Functional patterns were directly fabricated via a layer-by-layer approach. Physical models based on Monte Carlo method were conducted to understand the detailed microscale optical scattering, chemical reaction, polymerization, and their influence on critical fabrication parameters. The experimental data are in good agreement with the theoretical model, with a maximum deviation of approximately 10%.

CHAPTER IV

DIRECT LASER INTERFERENCE PATTERNING

Laser Interference patterning (LIP), a large-area maskless lithography (LAML) technique, involves the interference of two or more laser-beams permitting rapid fabrication with high design flexibility. This technique has been applied in the past not only to polymers but also to metals and ceramics [14]. In contrast with optical lithography and conventional laser interference lithography, in LIP no masks are needed and the shape and dimension of the interference patterns can be adjusted by controlling the number of laser beams as well as their geometrical configuration. The major advantage of LIP is that it is a relatively simple and fast process which consists of two steps: exposure and development. Common laser types open a wide field of possible process integration according to the work cycle due to the wide range of repetition rates and energy values available. Laser light can be easily guided from one place to another within the production line. Therefore, nearly all possible sample geometries can be structured and the system can be integrated in commonly used process cycles. Table 4.1 shows different processing times necessary to fabricate periodic arrays using both DLW and LIP. It can be seen that only some seconds are necessary for LIP while direct laser writing (DLW) requires many hours and even days in some cases.

Periodic pattern type	**Period (µm)**	**Patterned area (cm^2)**	**LIP time [a] (sec)**	**DLW time [b] (hours/days)**
Line-like	10	1	1	2. 8 / 0.12
Line-like	5	1	1	5.6 / 0.23
Cross-like	5	3	8 [c]	16.7 / 0.69
Corss-like	5	30	117 [c]	333.3 / 13.9

Table 4.1: Calculated processing times to fabricate different periodic arrays using LIP and DLW. [a] Q-switched Nd:YAG (Frequency 10 Hz, 3rd harmonic (355nm)) with a laser intensity of 200 mJ/cm² per pulse and 10 laser processing pulses (data from Spectra-physics). [b] Scanning speed: 1000 µm/s. [c] A time of 1 sec. was added for the translation stage considering that 1 cm^2 can be processed per time.

In this doctoral work, I report on the fabrication of periodic two- dimensional and three-dimensional structures in pentaerythritol triacrylate (PETIA), SU-8, and Shipley 1813 using Laser Interference Patterning with ns-laser pulses. Different periodic arrays, including line-, cross- and honeycomb-like structures were fabricated using two and three interfering laser beams. For PETIA, in order to reduce the laser fluence (energy per unit area) necessary to initiate photopolymerization, different weight fractions of a photoinitiator were utilized. Additionally, the effect of the PETIA layer thickness on the mechanical stability of the samples was investigated. For SU-8, 2.5 dimensional structures were achieved using a layer by layer method. To reduce the penetration depth, UV absorbers for SU-8 were also studied. Three-dimensional structures were successfully fabricated on large area with the use of UV absorbers.

4.1 Interference Theory

The simplest form of light is a monochromatic, linearly polarised plane wave. This is a sufficient approximation of a real laser beam. The electric field of a wave propagating in a homogeneous and non-absorbing medium can be represented as

$$E = E_0 e^{i(2\pi z/\lambda - \omega t)} \tag{4.1}$$

where z is the coordinate along the direction of propagation, ω is the angular frequency, and λ is the wavelength. The last two variables are related through the phase velocity c/n, c being the speed of light, and n the refractive index of medium.

Under the assumption of plane waves, the total electric field of the interference pattern can be obtained by the superposition of each individual beam:

$$E = \sum_{j=1}^{n} E_j = \sum_{j=1}^{n} E_{j0} e^{i(\bar{k}\cdot\bar{r} - \omega t)} \tag{4.2}$$

The product between the vectors $\bar{k}$ and $\bar{r}$ can be written in terms of α_j and β_j which are the angles of the beams with respect to the interference-plane as shown in figure 4.1:

$$\bar{k}\cdot\bar{r} = \begin{pmatrix} k\cdot\sin\alpha_j\cdot\cos\beta_j \\ k\cdot\sin\alpha_j\cdot\sin\beta_j \\ k\cdot\cos\alpha_j \end{pmatrix}\cdot\begin{pmatrix} x \\ y \\ z \end{pmatrix} \tag{4.3}$$

where k is the wave-number:

$$k = \frac{2\pi}{\lambda} \tag{4.4}$$

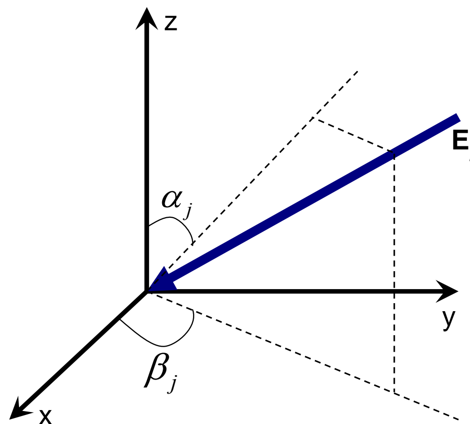

Figure 4.1 An input electric field of a wave.

Rewriting 4.2 in terms of α_j, β_j, x, y and considering ω=0:

$$E = \sum_{j=1}^{n} E_j = \sum_{j=1}^{n} E_{j0} e^{-ik(x\cos\beta_j - y\sin\beta_j)\sin\alpha_j} \tag{4.5}$$

which can also be written as:

$$E = \sum_{j=1}^{n} E_{j0}\left[\cos\left(-k\sin\alpha_j\left(x\cos\beta_j - y\sin\beta_j\right)\right) + i\sin\left(-k\sin\alpha_j\left(x\cos\beta_j - y\sin\beta_j\right)\right)\right] \tag{4.6}$$

An expression analogous to equation 4.1 also holds for the magnetic field B. The magnetic and electric field amplitudes are related by:

$$E_0 = cB_0 \tag{4.7}$$

The spatial intensity distribution is given by:

$$I = \frac{c\varepsilon_0}{2}\left|E\right|^2 \tag{4.8}$$

where c is the speed of light and ε_0 the permittivity of free space. With equation 4.6 and 4.8, the interference pattern of n-beams can be easily calculated.

If two laser beams are used, a one dimensional (1D) line-like interference pattern will be obtained (Figures 4.2 a and b).

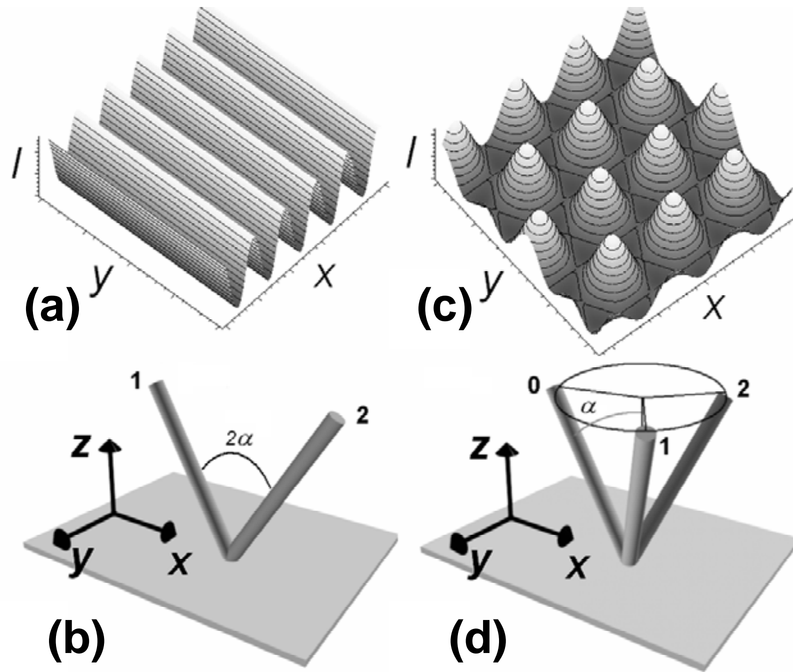

Figure 4.2 (a) line-like interference pattern resulting from (b) two laser beams; (c) hexagonal dot-like interference pattern from (d) three laser beams.

Assuming that:

$$E_{10} = E_{20} = E_0; \ \alpha_1 = \alpha_2 = \alpha\ ; \ \beta_1 = 0, \beta_2 = \pi \tag{4.9}$$

the intensity I(x) can be expressed as:

$$I = 2c\varepsilon_0 {E_0}^2 \cos^2(kx\sin\alpha) \tag{4.10}$$

with the period of (P):

$$P = \frac{\lambda}{2n\sin(\alpha)} \tag{4.11}$$

where α is the half angle between the laser beams, and n is the refractive index of the media through which the beams propagation.

Three-beam interference produces different 2-D arrays depending on the magnitude of the electric-field of each beam and the geometric configuration. For symmetric configuration (figures 4.2 c and d):

$$E_{10} = E_{20} = E_{30} = E_0; \ \alpha_1 = \alpha_2 = \alpha_3 = \alpha; \ \beta_1 = 0, \beta_2 = \frac{2}{3}\pi, \beta_3 = -\frac{2}{3}\pi \quad (4.12)$$

the intensity distribution I(x,y) is given by:

$$I = \frac{9}{2} c\varepsilon_0 E_0{}^2 [(-\cos(kx\sin\alpha) - \cos(kx(-\frac{x}{2} - y\frac{\sqrt{3}}{2})\sin\alpha) - \cos(kx(-\frac{x}{2} + y\frac{\sqrt{3}}{2})\sin\alpha))^2$$
$$+ (-\sin(kx\sin\alpha) + \sin(kx(-\frac{x}{2} - y\frac{\sqrt{3}}{2})\sin\alpha) - \sin(kx(-\frac{x}{2} + y\frac{\sqrt{3}}{2})\sin\alpha))^2]$$

(4.13)

4.2 Experimental procedure

4.2.1 Materials and sample preparation

4.2.1.1 Materials

The first photopolymerizable system used in the experiments consisted of two components: (i) pentaerythritol triacrylate (PETIA), an acrylate monomer, the chemical structure is shown in figure 4.3a, and (ii) a photoinitiator, N-methyldiethanolamine (N-MDEA), the chemical structure is shown in figure 4.3b. The weight fraction of the photoinitiator was varied from 2 to 15% obtaining five different compositions. All products were purchased from Sigma-Aldrich.

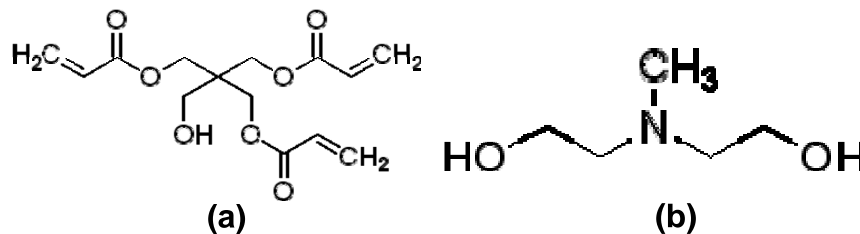

Figure 4.3 Chemical structures for (a) pentaerythritol triacrylate (PETIA) and (b) N-methyldiethanolamine (N-MDEA).

The second photopolymerizable system used in the experiments consisted of two components: (i) SU-8 5, a high contrast, epoxy based photoresist, purchased from

MicroChem, the absorbance spectrum is shown in figure 4.4 (ii) an absorber: (a) 95% Benzenepropanoic acid, 3-(2H-benzotriazol- 2-yl)-5-(1,1-dimethylethyl)-4-hydroxy-, C7-9- branched and linear alkyl esters and 5% 1-methoxy-2-propyl acetate (TINUVIN 384-2) as shown in figure 4.5 which was varied from 0.5% to 3%; (b) Phenol, 2-(2H-benzotriazol-2-yl)-6-dodecyl-4-methyl-, branched and linear (TINUVIN 171) as shown in figure 4.6, all absorbers were purchasedfrom Ciba.

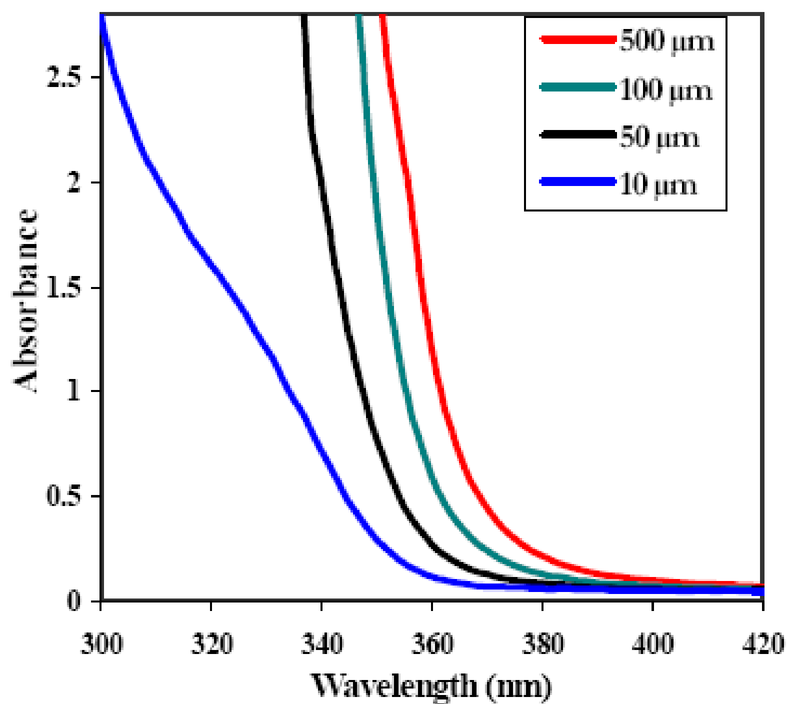

Figure 4.4 SU-8 absorbance vs. film thickness [141].

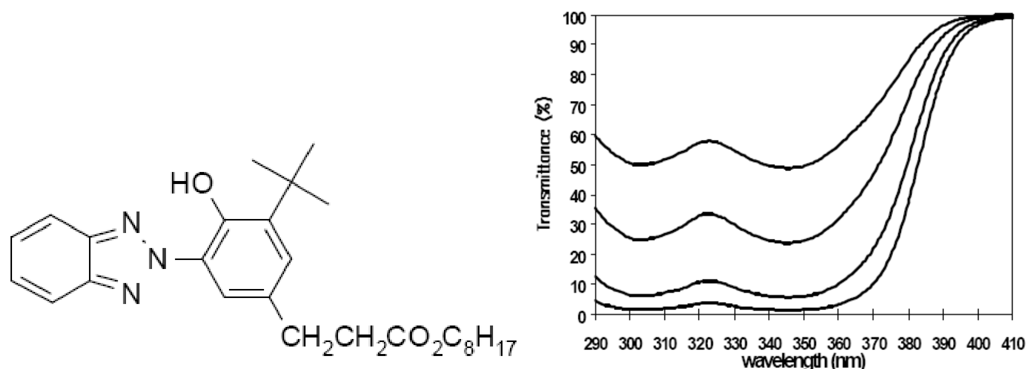

Figure 4.5 chemical structure and Transmittance Spectrum of TINUVIN 384-2 [142].

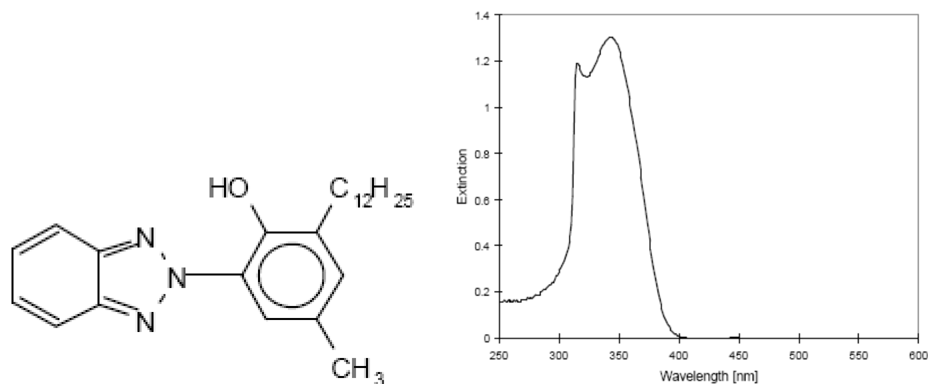

Figure 4.6 Chemical structure and absorption spectrum of TINUVIN 171 [143].

The third photopolymer is Shipley 1813 from MicroChem, the absorbance spectrum is shown in figure 4.7.

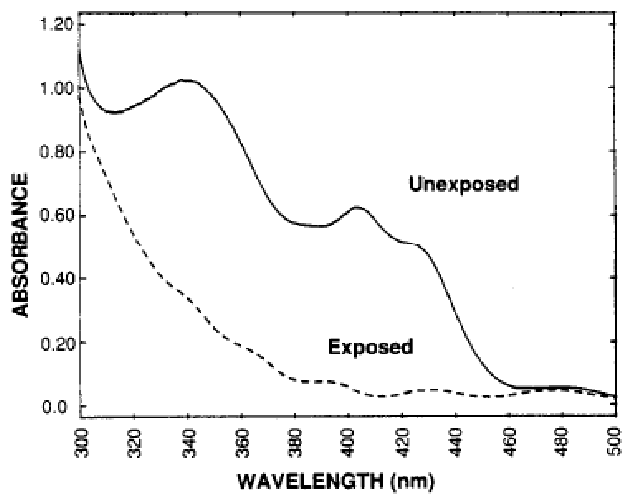

Figure 4.7 Absorbance spectrum of Shipley 1813 [144].

4.2.1.2 Sample preparation

To obtain maximum process reliability, cover glass substrates (18mm x 18mm purchased from Sigma Aldrich) and silicon wafers should be clean and dry prior to applying photopolymerizable systems. Substrates were rinsed with dilute acid (H_2SO_4 & H_2O_2) followed by a solvent (methanol or acetone) cleaning, followed by a DI water rinse. To dehydrate the surface, substrates were baked at 200°C for 5 minutes on a hot plate. All

material preparation and subsequent laser processing was done in an ambient UV-light free area.

The photopolymerizable solutions of PETIA were obtained by blending the monomer and photoinitiator. The weight fraction of the photoinitiator was varied from 2 to 15% resulting in five different compositions. Prepared solutions were stored in dark glass containers for subsequent use. Two different thicknesses of photopolymerizable PETIA films were used for the laser interference experiments. These films were produced by spin coating at 500 and 2000 rpm for 30 seconds onto cover glass substrates (18 mm x 18 mm). After the laser exposure, the samples were washed for 30 seconds using analytical quality acetone (Sigma Aldrich) and allowed to dry in air at ambient conditions of pressure and temperature.

For SU-8, two different spinning speeds, 2000 rpm and 3000 rpm, were used to prepare samples on cleaned silicon wafers. From figure 4.8, the thicknesses of these samples were 7μm and 5μm separately. Following spin coating, a series of steps were followed: (a) The samples were first soft baked at 95°C for 5 minutes to evaporate the solvent and densify the film on a level hot plate; (b) Then they were exposed with the interference laser beam; (c) After exposure, the samples were post baked at 95°C for 1 minute to selectively cross-link the exposed portions of the film on a level hot plate; (d) Finally, the samples were developed with a specially designed SU-8 developer from MicroChem for 1 minute and then dipped in ethyl lactate alcohol for 5 seconds to stop the development process. For three-dimensional patterning, different amount of absorbers were added to SU-8. The same processing procedures were taken to prepare samples for the mixed photopolymerizable systems as pure SU-8 and the same film thicknesses were

achieved due to the amount of the absorbers bing very small (0.5%-3%) and the viscosity of the absorbers being very close to SU-8.

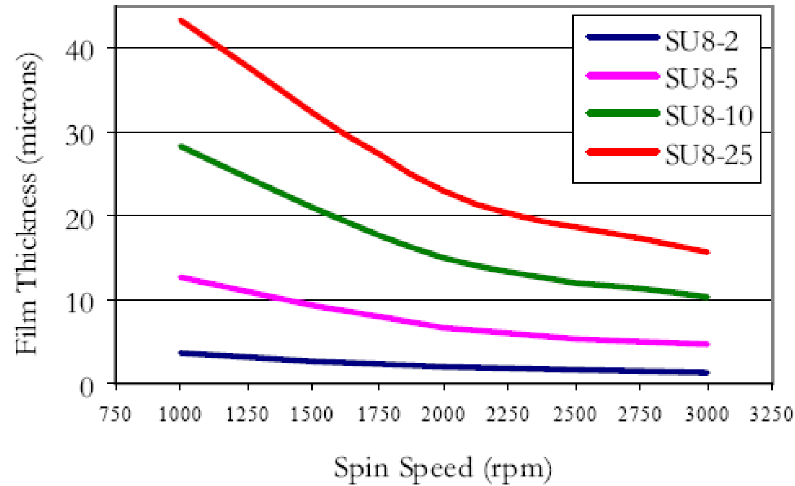

Figure 4.8 Spin speed vs. thickness curves for selected SU-8 resists [141].

Samples of Shipley 1813 film were prepared by spin coating at 2000rpm for 30 seconds onto cover glass substrates (18 mm x 18 mm). From figure 4.9, the films were around 2μm thick. The samples were soft baked at 115°C for 4 minutes and post baked at 115°C for 1 minute before and after laser exposure. Post baked samples were washed in developer Shipley 351 (MicroChem) for 1 minute and then dipped into water to stop the development process.

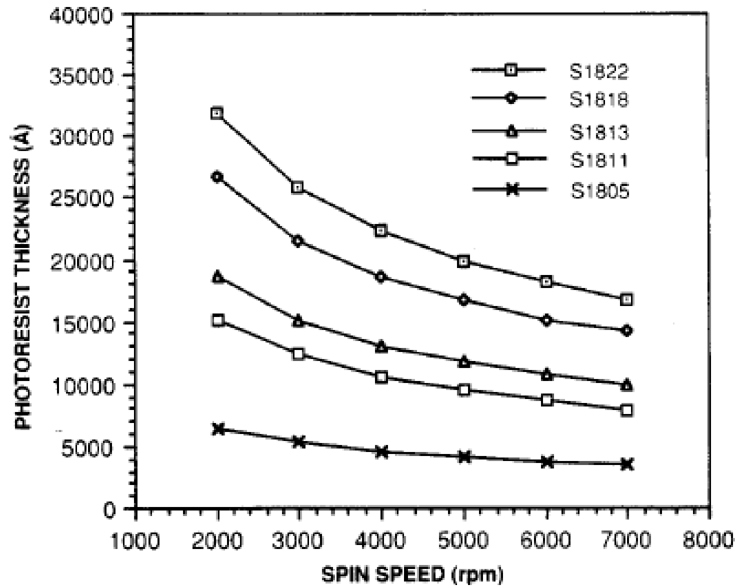

Figure 4.9 Spin speed vs. thickness curves for Shipley 1800 resists [144].

4.2.2 Laser interference experimental setup and sample characterization

4.2.2.1 Experimental setup

A schematic of the experimental setup is shown in Figure 4.10. A high-power pulsed Nd:YAG laser (Quanta-Ray PRO 290, Spectra Physics) was employed for the LIP experiments. The fundamental wavelength of the Nd:YAG laser is 1064 nm from which shorter wavelengths (532, 355 and 266 nm) can be generated by harmonic generation. For our experiments, the samples were irradiated at 355 nm with pulses lasting 10 ns. Laser light of 355 nm wavelength was selected because the materials utilized in our experiments presents an absorption band centered at about 350 nm. Absorption at 266 nm or 532 nm for these materials is relatively low. The frequency of the laser was 10 Hz and the beam was linearly polarized. Since the polarized beam is perpendicular to the plane of incidence, the direction of the polarization vector is the same after reflection and thus we obtain p-linear polarized beams on the sample. The number of laser pulses incident on the

sample was controlled using a mechanical shutter (VS25S2ZMO Uniblitz Electronic). The angles between the laser beams were changed in order to produce different periodical structures. All the samples were irradiated at ambient conditions of temperature and pressure.

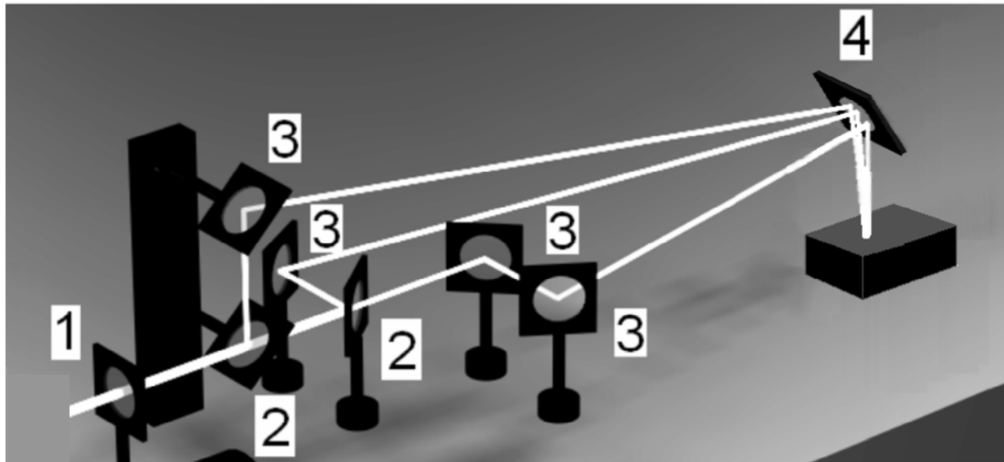

Figure 4.10: Schematic set-up for the three beam laser interference system: (1) lens, (2) beam-splitters, (3) mirrors, (4) sample. Note that the primary beam is divided into 3 sub-beams which are overlapped at the sample surface.

4.2.2.2 Samples characterization

The patterned samples were imaged using a high-resolution scanning electron microscope (SEM) with an operating voltage of 10 kV (LEO 1530 Thermally-Assisted Field Emission microscope). All samples were coated with 2 nm gold/palladium layer to improve the electrical conductivity, prior to imaging.

4.3 Results and discussion

4.3.1 Laser interference patterning of PETIA

The influence of the photoinitiator (N-MDEA) on the threshold laser fluence necessary to photopolymerize the PETIA was investigated. Two laser beams were used to produce line-like interference patterns with a period of 7.80 μm (Figure 4.11 a, b). For this set of experiments, PETIA films with a thickness of about 2-3 μm on glass substrates were utilized. It is well known that for this photosensitive PETIA solution, the photopolymerization reaction is initiated through a radical-based process [145]. In particular, N-MDEA is involved in radical formation, and once the UV-radiation is absorbed, the amine can be oxidized, allowing the PETIA monomer to cross link [146]. Because a UV light source was utilized (355 nm), the use of a sensitizer dye (like 2, 4, 5, 7-tetrabromofluorescein disodium salt, Eosin Y) was not necessary to increase absorption.

Figure 4.11 shows both the effect of the number of laser pulses and the photoinitiatior concentration on the threshold fluence. As can be observed, for a fixed number of laser pulses, an increase in the photoinitiator concentration results in a lower laser intensity necessary to initiate the photopolymerization process up to 10 w/w %. Beyond this value, increasing the photoinitiator concentration becomes unfavorable for the polymerization reaction. Normally, an increase of photoinitiator concentration should increase the polymerization rate. However, at high concentrations it is reasonable to consider that the quantum yield associated with the photoinitiator efficiency can decrease when the photoinitiator increases [147], thus explaining this behavior. A concentration of N-MDEA between 10 to 15 % w/w may seem high, however this formulation is less sensitive to side reactions due to oxygen [148].

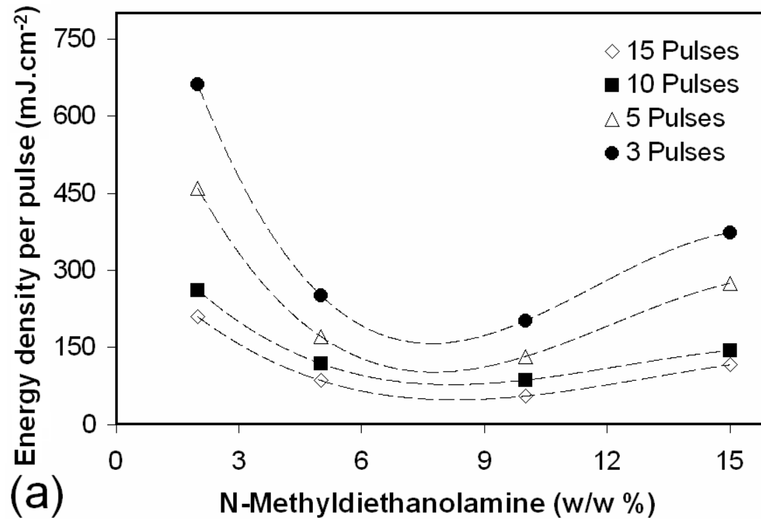

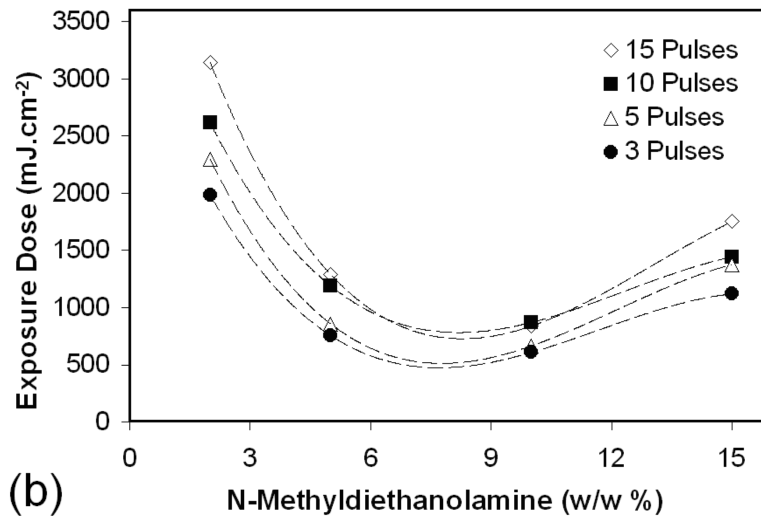

4.11: (a) Energy density per pulse and (b) Exposure Dose (mJ.cm^{-2}) necessary to photopolymerize the PETIA solution (with an interference pattern with period of 7.80 µm) as function of N-MDEA photoinitiator weight fraction.

It can also be observed that if fewer laser pulses are used (3-5), a lower exposure dose (laser fluence · number of pulses) is necessary to cross-link the polymer (Figure 4.11b). For example, at an N-MDEA concentration of 2 % w/w, the exposure doses are 3.15 and 1.98 J.cm^{-2} for 3 and 15 pulses, respectively. Considering that after the first laser pulses hit the sample, some surface modification is induced, a different behavior can be expected for the subsequent pulses. This implies that as the number of laser pulses increases, part of the energy given to the polymer is lost, likely due to light scattering

from polymerized surfaces. Despite the fact that few laser pulses are energetically more efficient to produce the periodic arrays (considering the total dose as shown in 14.11b), laser systems with higher intensities would be necessary or smaller patterning speeds could be achieved. Consequently, a compromise between number of pulses and laser power must be found to get the best performance (patterned area over time). This effect is stronger at low concentrations (2-5 % w/w) of the photoinitiator.

Figure 4.12 shows different periodic arrays produced using 10μm thick PETIA films (N-MDEA 15 % w/w) on glass substrates irradiated with 10 laser pulses and 244 $mJ.cm^{-2}$ of laser fluence (per pulse). Using this laser intensity, a total area of about 3.6 cm^2 could be patterned in 1 second. The period of the corresponding line-like pattern was 7.80 μm.

In the case of the line-like structures (Figure 4.12a), relatively thicker lines (about 7 μm height) could be fabricated. However, due to the poor mechanical stability of the polymer, the lines fell over sideways during the development process. If now a double exposure process is performed (irradiation of the sample with the line-like interference pattern, 90° rotation of the sample, second irradiation of the sample with the same pattern), cross-like structures could be fabricated (Figure 4.12b-c). Due to the cross-linked geometry of the pattern, the resulting structure is more stable and remains upright during the development process. As shown in Figure 4.12c, the periodic arrays were fabricated on a macroscopic area in only 3 seconds.

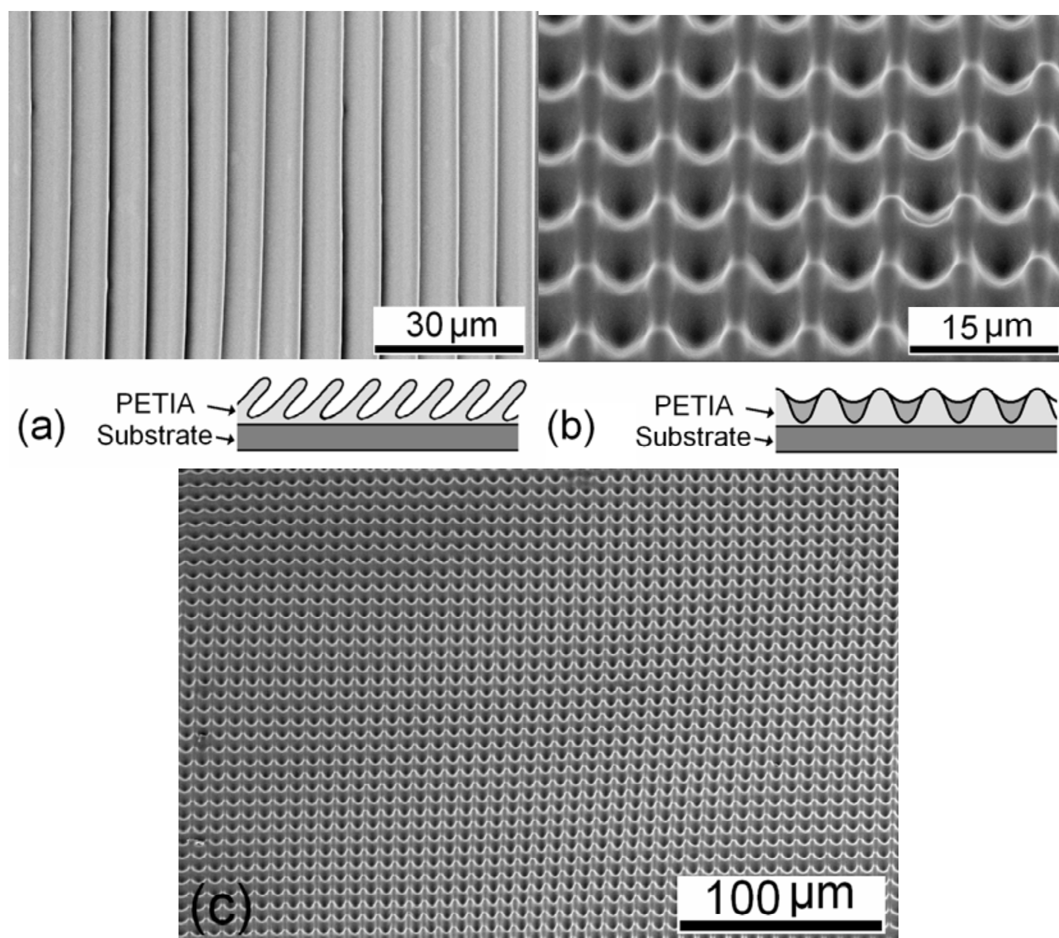

Figure 4.12: (a) Line-like and (b, c) cross-like periodic patterns (period 7.8 µm) after development of the thicker PETIA layer. In (c), a macroscopic area with a cross-like structure is shown. The laser fluence (per pulse) was 244 mJ.cm^{-2} and 10 laser pulses were used (scanning electron micrographs, tilt: 45°).

Since thicker PETIA films irradiated with line-like interference patterns also produce thicker lines that are structurally not stable, irradiation of thin layers of the photosentive PETIA solution should solve the mechanical stability problem. Figures 4.13a and b show different line-like arrays on the thin PETIA films (2-3 µm) produced using 5 laser pulses and fluences of 174 and 229 mJ.cm^{-2}, respectively. In this case, the total patterned area was approximately 0.80 cm². As can be observed, lower laser fluences permit fabrication of isolated PETIA lines (about 4.9 µm width, see Figure 4.13a) while higher laser intensities (or a larger number of laser pulses) results in interconnected wider lines

(Figure 4.13b). Additionally, if larger angles between the laser beams (Figure 4.11a) are utilized, sub-micrometer arrays can be obtained as shown in Figure 4.13c. In the last case, the angle between the laser beams was approximately 21.4° resulting in a period of 811 nm (with n = 1.17, see Equation 4.11).

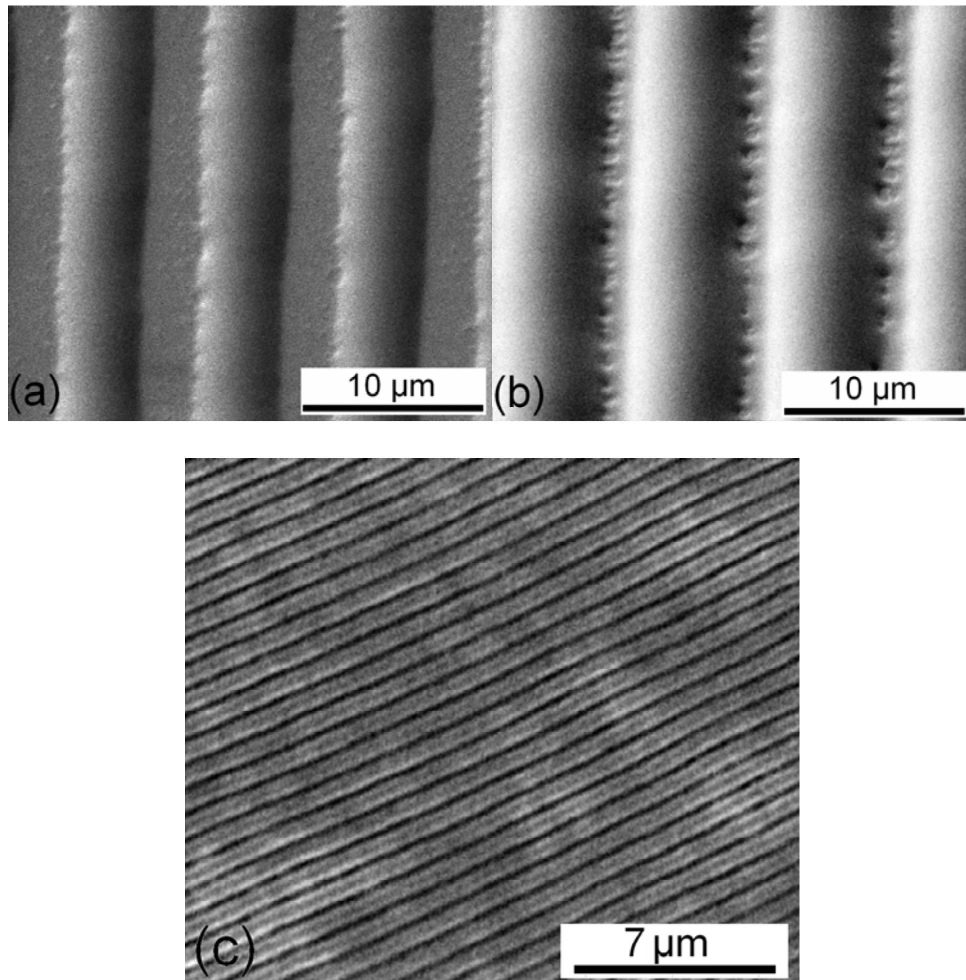

Figure 4.13: Line-like periodic structures after development of the thin PETIA layers obtained using 5 laser pulses and (a) 174 , (b) 229, and (c) 210 mJ.cm^{-2} of laser fluence (per pulse). Notice that the lines in (a) are isolated. The period in (a) and (b) was 7.80 µm while in (c) was 0.81 µm (scanning electron micrographs, Tilt: 30°).

Using the same approach described above to fabricate the cross-like structures, the thin PETIA films were irradiated with lower laser intensities (174 mJ.cm^{-2}) and 5 laser pulses (Figure 4.14a). As is shown in the figure, at the positions where the sample was

irradiated twice (at the interceptions), wider photopolymerized regions are observed. Additionally, due to the shrinkage of the polymer, the width of the lines decreases at the zones between two consecutive intersecting positions. Using a similar procedure, honeycomb-like structures were fabricated by rotating the sample 45° between successive irradiation steps (Figure 4.14b). The lines plotted in Figure 4.14c indicated the direction of the interfering lines in both processing steps. As can be observed in Figure 4.14b, individual lines of the line-like interference patterns cannot be observed after the development process. Instead, the structures show some degree of self-organization in order to achieve a more mechanically stable shape such as the honeycomb structure [149]. The same effect is observed for a PETIA sample irradiated with laser interference patterns with a period of 15.12 µm (Figure 4.14d).

If three laser beams arranged with a symmetrical configuration are used ($\beta_1 = 0$, $\beta_2 = 120$, and $\beta_3 = -120°$, see Equation 4.5), a dot-like array as shown in Figure 4.11c is obtained. For this configuration, the period of the interference pattern is given by:

$$P = \frac{\lambda}{\sqrt{3}\, n \sin(\alpha)} \tag{6}$$

For our experiments, the angle α (see Figure 4.11d) was approximately 2.1° which results in a period of 4.8 µm (with $n = 1.17$). Figure 4.15 shows the surface topographies of thin PETIA samples (10 % w/w N-MDEA) irradiated with 3 laser beams (symmetrical configuration) under different laser intensities as well as number of laser pulses. The total patterned area was approximately 0.80 cm² in this case as well.

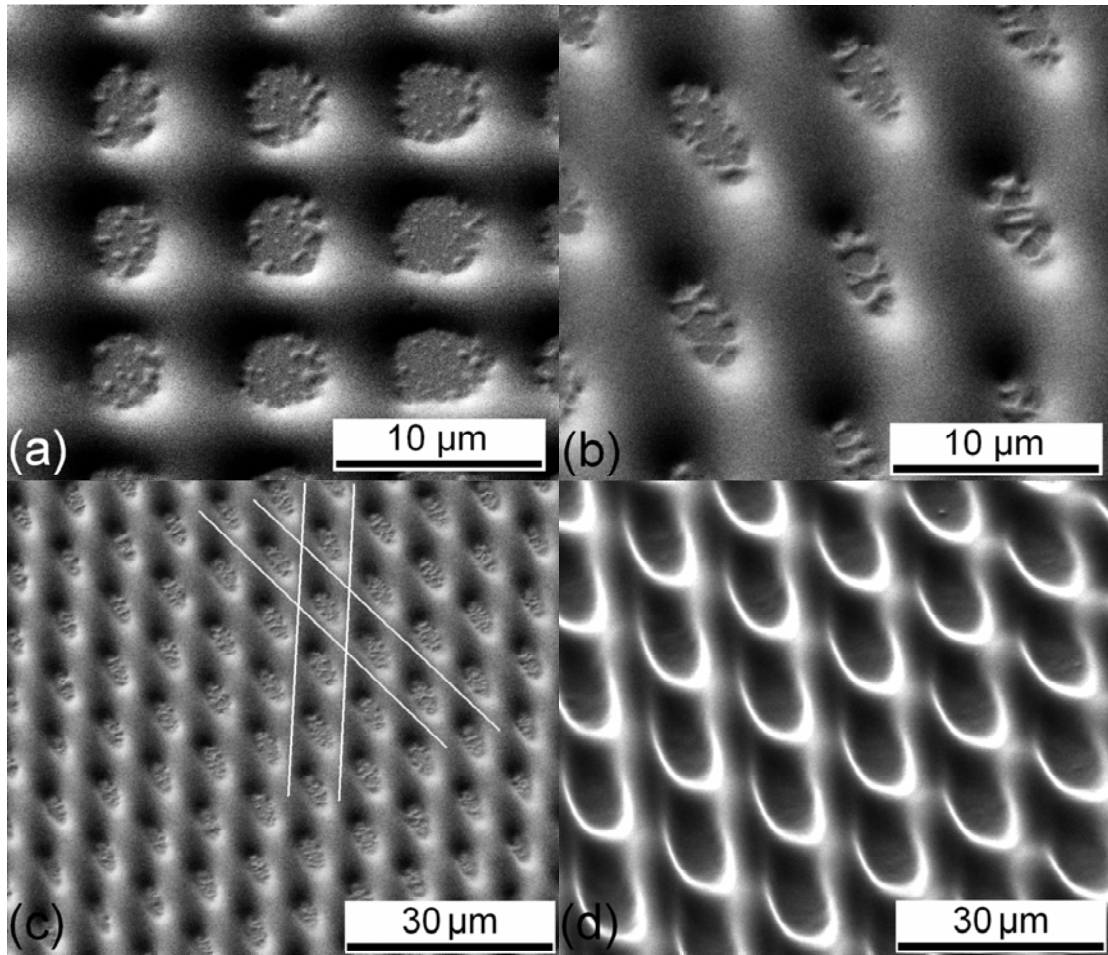

Figure 4.14: (a) Cross- and honeycomb-like periodic structures after development of the PETIA solution. In (a, b and c), the period was 7.80 μm while in (d) was 15.12 μm. The lines in (c) indicate the direction of the interference pattern of both exposure processes. In (a), the sample was rotated 90° between the exposure procedures, while in (b, c and d) the angle was 45° (scanning electron micrographs, Tilt: 30°). The laser fluence (per pulse) in (a, b and c) was 244 $mJ.cm^{-2}$ while in (d) was 320 $mJ.cm^{-2}$.

At lower laser intensities (Figure 4.15a), isolated dots arranged in a hexagonal pattern can be observed [150, 151]. The calculated intensity distribution of the interference pattern is shown in the insert of Figure 4.15a for this laser beam configuration. As the laser intensity increases, the isolated dots grow increasing their height (Figures 4.15b) and building bridges between the interference maxima positions (Figure 4.15c) obtaining a structure similar to the brittelstar microlens array [150, 152].

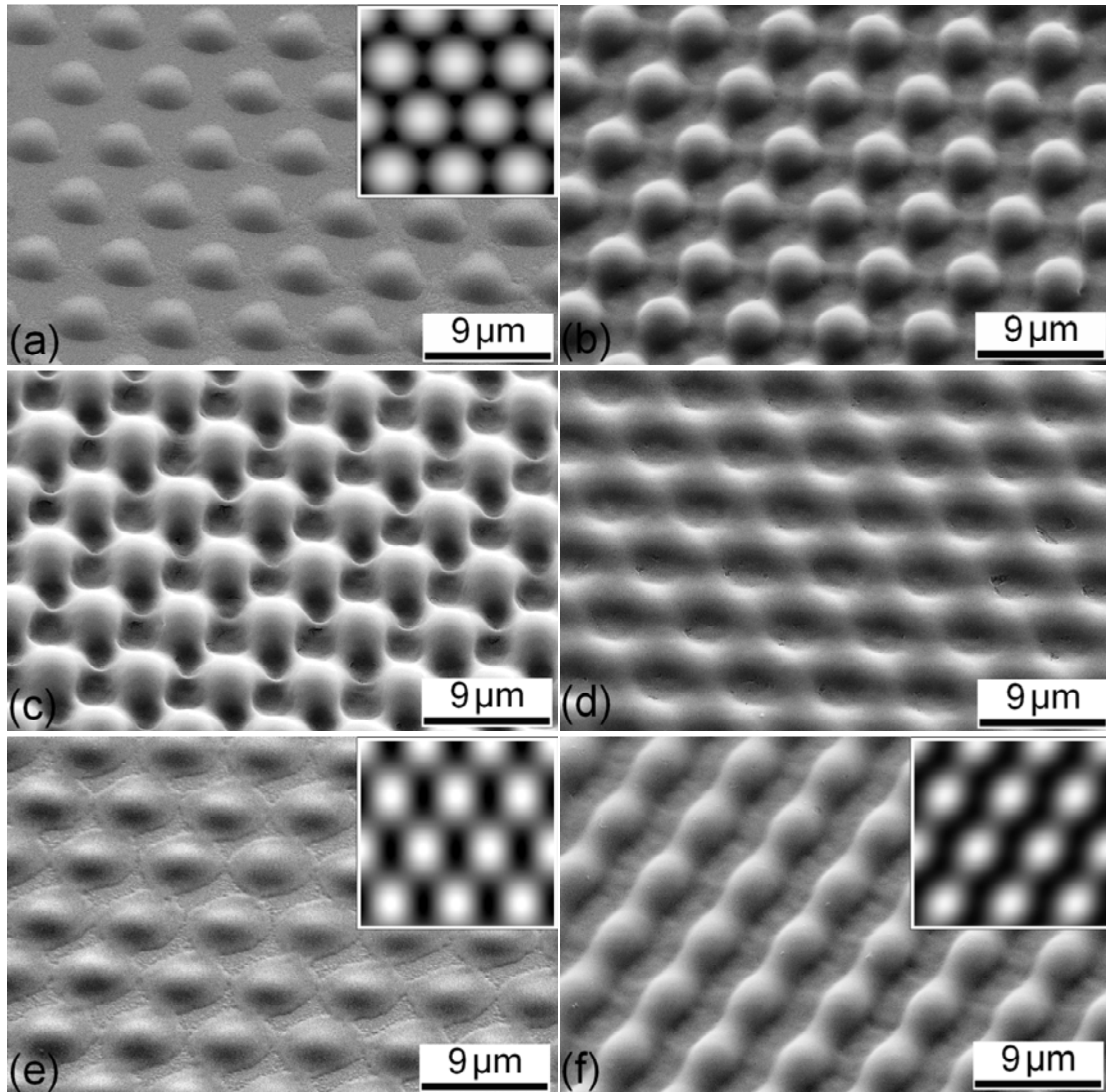

Figure 4.15: Two dimensional periodic structures fabricated using 3 laser beams with symmetrical configuration. For (a-d), the laser intensity of each individual laser beam was the same ($E_{01} = E_{02} = E_{03}$), while for (e) and (f) different intensities were utilized. (a) 10 pulses, 176 mJ.cm^{-2}; (b) 3 pulses, 273 mJ.cm^{-2}; (c) 5 pulses, 273 mJ.cm^{-2}; (d) 10 pulses, 273 mJ.cm^{-2}; (e) $E_{02} = E_{03} = 1/3 \cdot E_{01}$; (f) $E_{02} = 2/3 \cdot E_{01}$; $E_{03} = 1/3 \cdot E_{01}$. The period of the structure was 4.8 µm. The inserts in (a), (e) and (f) correspond to the calculated intensity distributions of the interference patterns (scanning electron micrographs, Tilt: 30°).

As the number of laser pulses (or laser intensity) increases, the thickness of the photopolymerizable solution allows the bridges to grow, closing the structure and thus forming a symmetrical honeycomb like structure (Figures 4.15d). Additionally, due to the high laser intensity as well as the large number of laser pulses, the PETIA solution was polymerized also at the interference minima positions (holes). Considering that the cure

depth is proportional to the natural logarithm of the exposure dose, the evolution of the topography as a function of the laser intensity was calculated, in an accordance with equation 3.12 (Figure 4.16). As can be observed, at lower intensities isolated dots are obtained, while at higher intensities, structures such as those shown in Figures 4.15c and d are obtained, confirming the experimental results.

In addition, if the laser intensity of each beam is not the same, a different modulation of the interference patterns is achieved. For example, if $E_{02} = E_{03} = 1/3 \cdot E_{01}$, the periodic structure shown in Figure 4.15e is obtained, while for $E_{02} = 2/3 \cdot E_{01}$; $E_{03} = 1/3 \cdot E_{01}$, a ripple-like structure can be fabricated (Figure 4.15f). Notice that in each case, the calculated intensity distribution of the interference pattern using Equation 4.8 (see insert in Figure 4.15e and f) corresponds to the polymerized periodic array. Similarly, many other interesting topographical features can be obtained with different intensity ratios. These are being investigated at present.

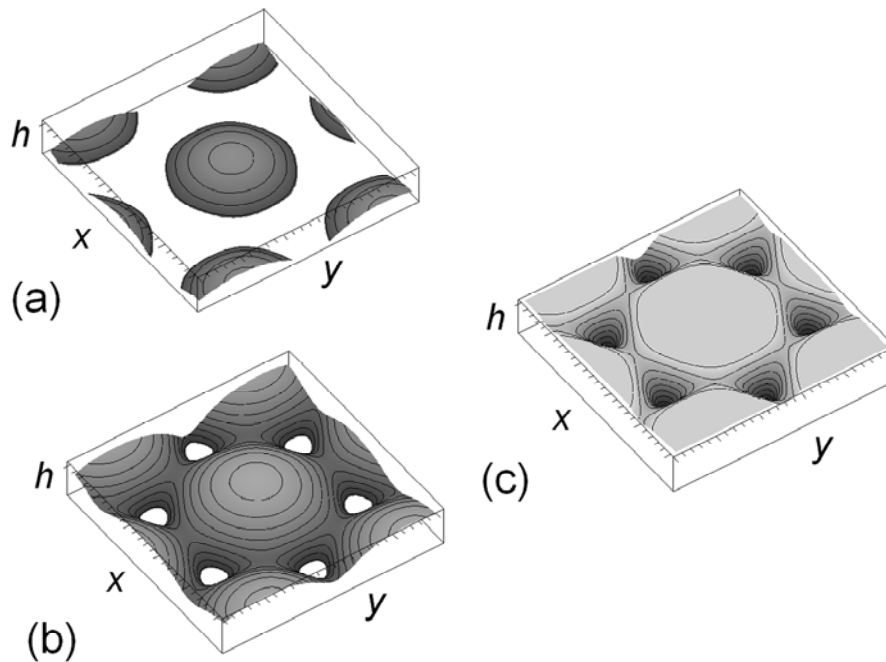

Figure 4.16: Calculated cure depth (h) at three dosages level (E_{max}) for a symmetrical three beams interference pattern. (a) E_{max} = E; (b) E_{max} = 1.75 E; (c) E_{max} = 3.75 E.

4.3.2 2.5 and 3 dimensional laser interference patterning of SU-8

SU-8 is a commonly used negative photoresist, it can be used to pattern high aspect ratio (>20) structures. Figure 4.17 shows the line-like periodic structures patterned with SU-8 using two beam laser interference. The period of the structures is 5μm and the line width is 2.5μm.

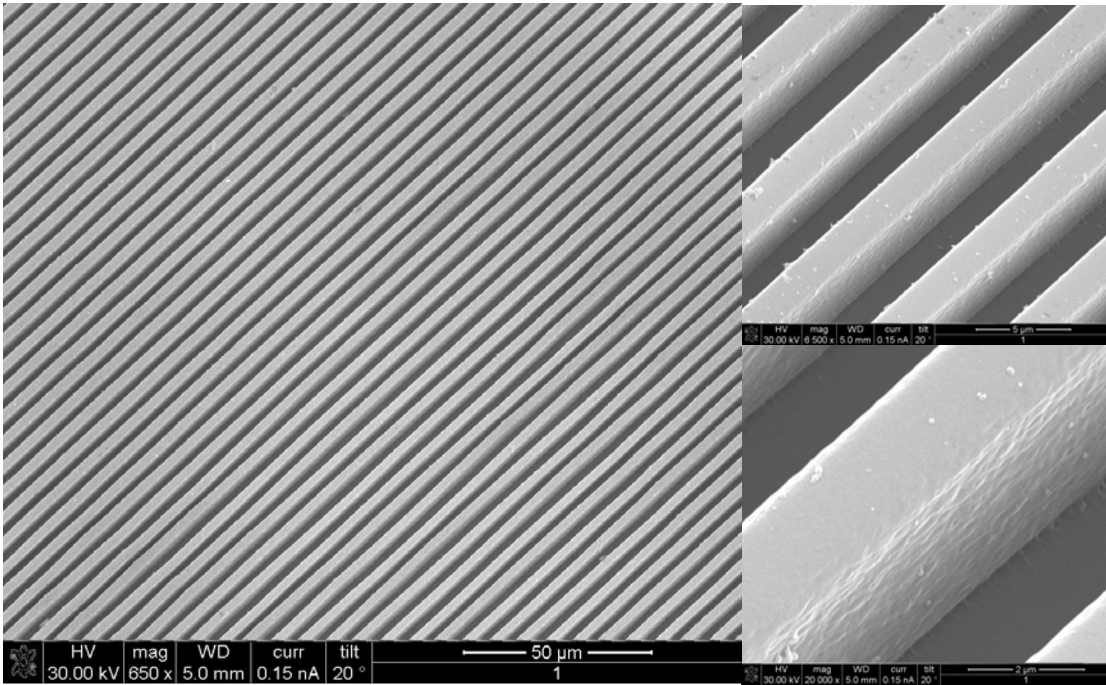

Figure 4.17 SEM images of line-like periodic structures after development of the thin SU-8 layer.

SU-8 has very low shrinkage rate (7.5%) and very high mechanical property after hard exposure. Three-dimensional fabrication using laser interference patterning was investigated with SU-8. The experimental procedure was as follow: (a) thin films of SU-8 were applied on to silicon substrates, patterned and developed as described in section 4.2.1; (b) another layer of SU-8 was spin-coated on the top of the pattern with 2000rpm; (c) procedure (a) was repeated with the sample a 90° rotation with respect to the first pattern prior to patterning with interference laser beams.

At first, SU-8 was directly used for 3D patterning. Due to the high penetration depth

of SU-8, 2.5D structures were patterned, as shown in figure 4.18. From higher magnification SEM images, it was evident that the second exposure cured both first layer and second layer, which is indicated by the red arrow, the second layer was cured through the first layer.

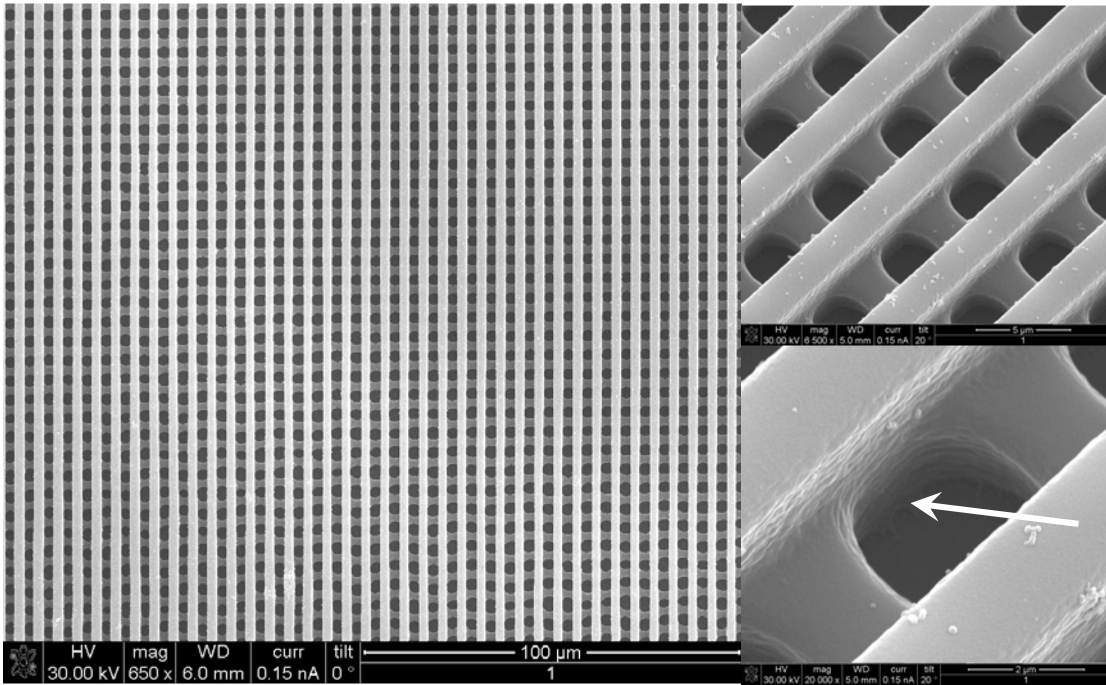

Figure 4.18 SEM images of 2.5D periodic structures patterned with SU-8.

To reduce the penetration depth of SU-8, a UV absorber was employed. The UV absorber has the primary function of absorbing ultraviolet and emitting it as thermal energy, and the secondary function of terminating creation of free radicals which decrease its own capability of absorbing ultraviolet. Figure 4.19 shows 3D patterning of SU-8 with 1.5% (w/w) absorber (TINUVIN 384-2). By reducing the penetration depth, the second exposure only cured the second layer. To study the effect of the percentage of absorber in SU-8, a sequence of 3D patterns were fabricated with different amounts of absorber, as shown in figure 4.20.

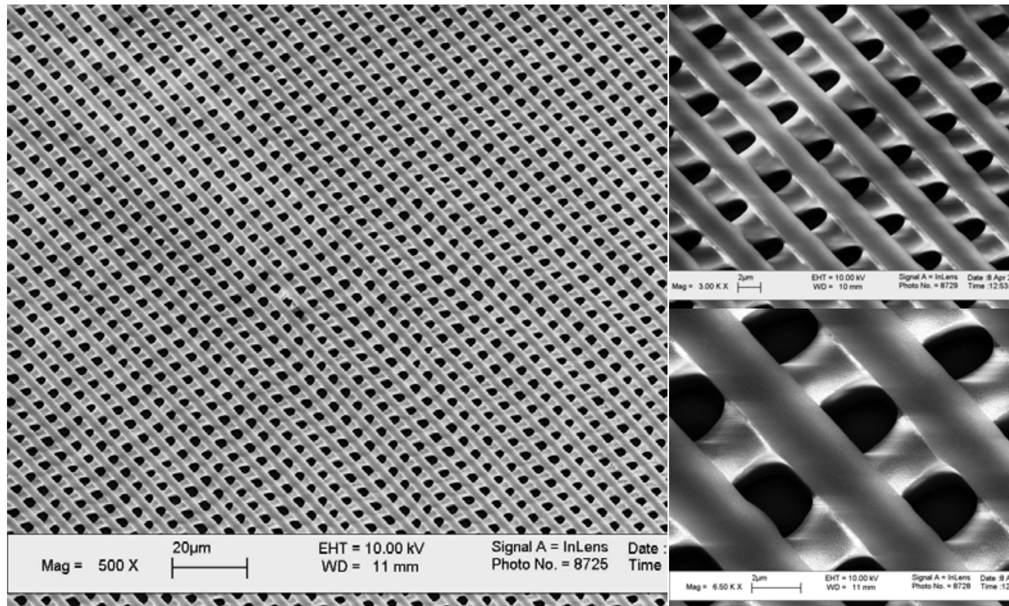

Figure 4.19 3D periodic structures of SU-8 with 1.5% (w/w) absorber.

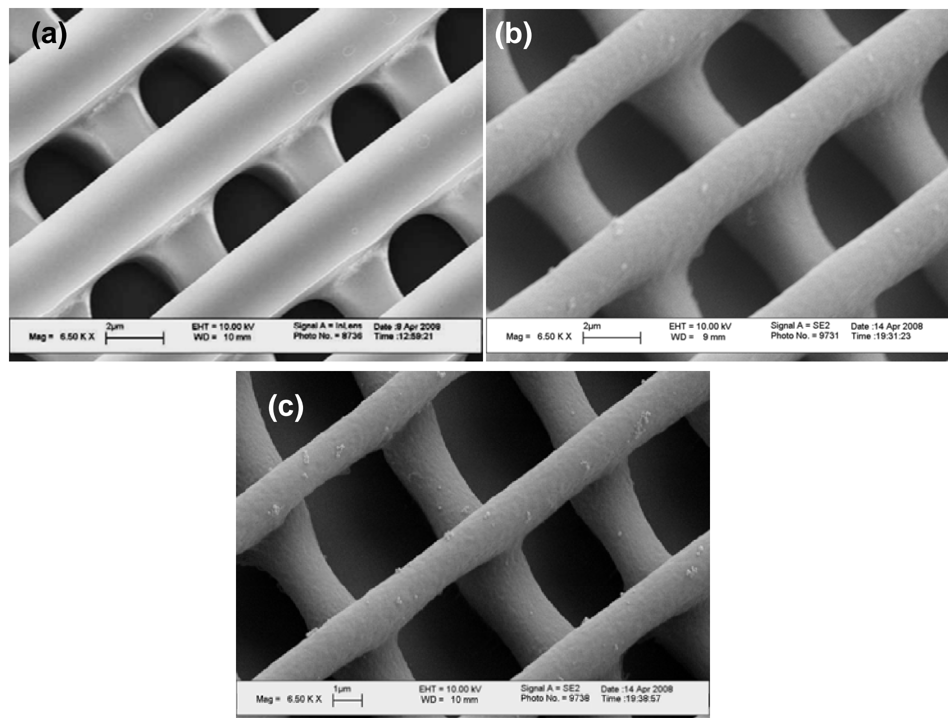

Figure 4.20 3D periodic structures of SU-8 with different percentage of absorber (a) 1% (w/w), (b) 2% (w/w), (c) 3% (w/w).

From the lower magnification SEM image of figure 4.20, it can be seen that when the concentration of absorber was larger than 2%, due to less overlap between the two

layers, the second layer was not stable. Distortion occurred in some areas after development.

4.3.3 Laser interference nanopatterning of Shipley 1813

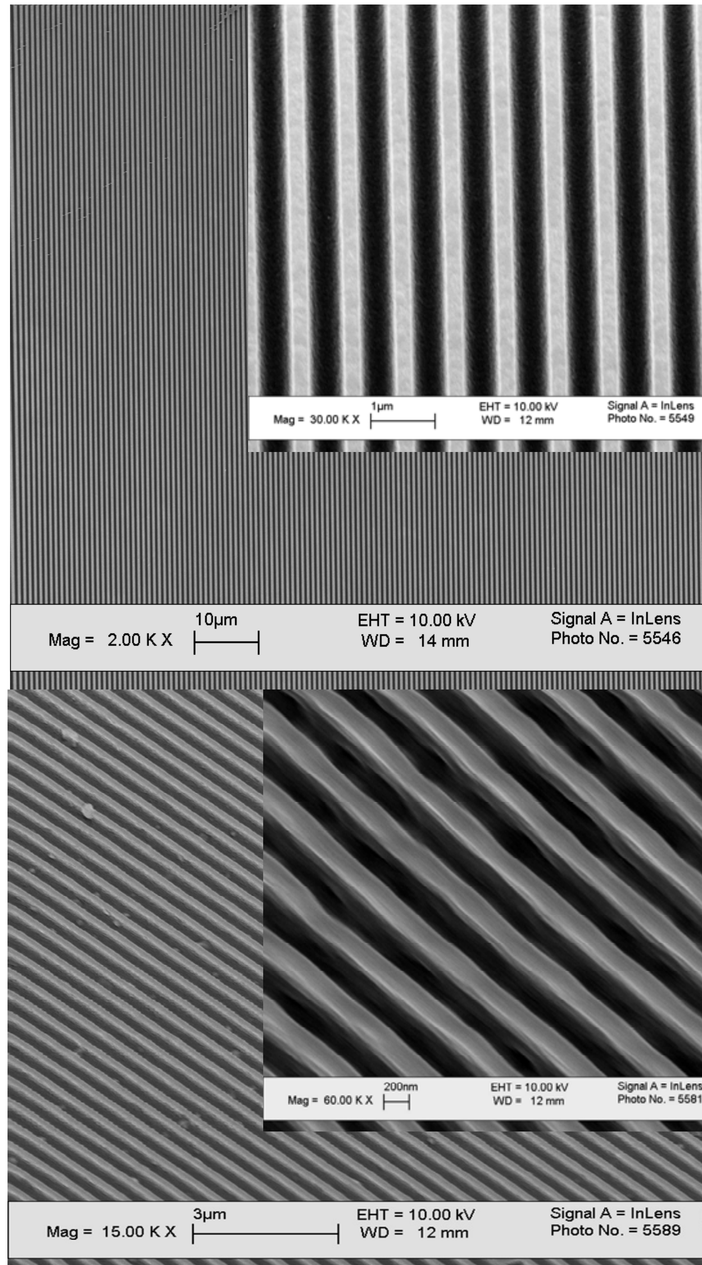

Figure 4.21 SEM images of nano periodic structures with Shipley 1813, period: 830nm, line width: 410 nm, patterning area: 1.5cm^2.

Shipley 1800 series is another commonly used positive photoresist, designed for

advanced IC device fabrication in high resolution. To demonstrate the nanopatterning ability of our laser interference system, the experimental configuration was adjusted to pattern line-like structures with a nanoscale period in Shipley 1813. The angle between two interference beams was changed to 25°.

From section 4.1, for two beam interference, the period of the line-like structures can be expressed as: $P=\lambda/(2n\sin\alpha)$ where α is the half angle between the laser beams, and n is the refractive index of the media around the interference beam. With a 25° separation angle, the period of the line-like structures is 830nm with $1.5cm^2$ fabrication area, as shown in figure 4.21.

4.4 Summary and Conclusions

In this chapter, direct laser interference on photopolymerizable materials was investigated. A patterning system, with a frequency-tripled Nd:YAG laser, beam delivery system, and optical shutter, was designed and realized. Three photopolymerizable materials were used. PETIA with different concentrations of photoinitiator (N-MDEA) was used to investigate the relationship between laser exposure and the percentage of photoinitiator. Different periodic structures, such as line-, cross-, honeycomb- and dot-like structures, were fabricated using PETIA. SU-8 with absorber TINUVIN 384-2 was used to investigate three-dimensional patterning. Concentrations of 0.5%-3% (w/w) of absorber were used, and 1%-2% were found to be appropriate to achieve massive stable three-dimensional structures. Shipley 1813 was used to realize sub-microm line-like patterns. Patterns with line width of 420nm were fabricated.

CHAPTER V

LASER-INDUCED NEAR-FIELD PATTEIRNG

As industry demands smaller and smaller structures, the production of micro- and nanostructures has attracted much attention in the last decade and still is a progressing field. To overcome the diffraction limit in focusing light and to spatially control matter on a nanometer scale, several fabrication techniques based on near-field optics have been employed. One such technique for creating structures utilizes the near-field radiation created around a microsphere by laser radiation. The accidental discovery of particle induced damage during dry laser cleaning of irregularly shaped Al_2O_3 particles on glass [79] has led to this exciting yet simple technique. When spherical colloidal particles such as silica were used as contaminants on a conjugated polymer surface, features with diameters of 200–400 nm with depths of 10–80 nm depending on the irradiation conditions, were found at the former position of the particles. Instead of using colloidal particles, if microspheres are arranged in a periodic monolayer on the substrate, massively parallel nanostructuring could be realized.

Conducting polymers have become attractive for applications in microelectronics over the last decade. Among them, poly(3,4-ethylene dioxythiophene) poly(4-styrene sulfonic acid) (PEDOT-PSS) is one of the most widely used materials in the field of organic electronics. PEDOT-PSS has been used to fabricate neural electrodes [153],

flexible photovoltaics [154] as well as batteries [155].

To pattern π-conjugated polymers, different methods have been previously explored and can be broadly divided into either reactive or non-reactive processes [156]. Reactive methods usually involve radiation to locally initiate a chemical reaction in a polymer or precursor–polymer film [35], while non-reactive patterning methods involve lithographic techniques [157] to pattern a polymer in its final form without the requirement of further chemical or thermal treatments. The availability of powerful lasers operating in both the visible and UV wavelengths has made it technically feasible to structure electrically conducting polymers with high resolution.

A massively parallel nano-patterning procedure based on the laser-induced near-field effect was developed using a single laser beam and two interfering laser beams from a ns-laser pulsed laser. This technique was investigated for nanopatterning films PEDOT-PSS, over a metallic gold/palladium layer.

This chapter describes two aspects of this work: (a) nanosphere self-assembly and (b) laser induced near-field patterning.

5.1 Nanosphere self-assembly

5.1.1 Theory of 2D self-assembly

The experiments carried out by Nagayama and coworkers [158] revealed for the first time the mechanism of the self-assembly process that eventually leads to hexagonally close packed arrays of colloidal particles. Following their argument, array formation proceeds in two steps. At the first stage a "nucleus" of an ordered phase appears when the upper surface of the thinning aqueous layer in the wetting film presses the latex particles

toward the water-glass interface. As shown theoretically by Kralchevsky et al when spherical particles are partially immersed in a liquid layer on a horizontal solid substrate, the deformations of the liquid-gas interface give rise to strong and long-range interparticle capillary forces. The physical nature of these forces can be explained as follows. Considering two particles of radius R, partially immersed in a liquid layer, whose thickness tends to a constant value l_0 at a large distance from the two particles (see Figure 5.1).

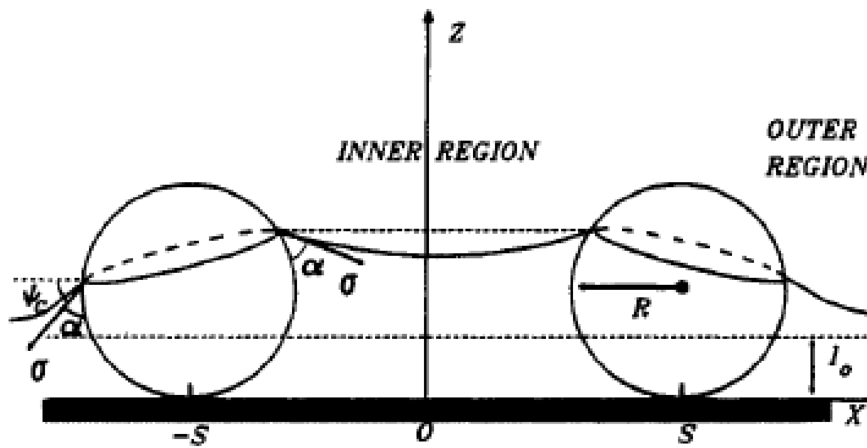

Figure 5.1. Two spheres partially immersed in a liquid layer on a horizontal solid substrate. The deformation of the liquid meniscus gives rise to interparticle attraction [158].

The shape of the meniscus obeys the Laplace equation of capillarity and is determined by the distance L = 2S between the particles, the layer thickness l_0**,** and the value of the contact angle α**,** which characterizes the particle wettability. The water level in the inner region (between the particles) is higher than in the outer region. The ensuing inclination of the three-phase contact lines at the particle surfaces gives rise to two capillary effects, both leading to attraction: (i) pressure effect, caused by the higher hydrostatic pressure in the gas phase than the pressure in the liquid at $z > l_0$ (especially in the inner region), this pressure difference pushes the particles toward each other; (ii)

surface force effect due to the fact that the slope (with respect to the horizontal) of the liquid surface, and hence the x component σ_x of the surface tension force σ, varies along the contact line. The developed theory [159-161] shows that for micrometer-size and smaller particles the surface tension effect exceeds the pressure effect by many orders of magnitude. With high accuracy the attractive capillary force (more precisely its horizontal projection F_x) can be expressed as [160] :

$$F_x \approx 2\pi\sigma r_c^2 (\sin^2 \Psi_c)(1/L) \quad r_c << L << (\sigma/(\Delta\rho)g)^{1/2} \qquad (5.1)$$

where σ is the surface tension of the liquid, r_c is the radius of the three-phase contact line at the particle surface, Ψ_c is the mean meniscus slope angle at the contact line, g is the gravitational acceleration, and $\Delta\rho$ is the difference between the mass densities of the liquid and gas phases.

It is worth noting that the capillary forces between particles partially immersed in a liquid layer on a solid substrate are many orders of magnitude greater than the capillary forces between similar particles floating attached to a single interface, which are sometimes called "flotation capillary forces" [162]. The immersion forces are so strong that the respective energy of capillary attraction can be much larger than the thermal energy, k_BT, even with submicrometer particles. On the contrary, the flotation forces are negligible for particles smaller than 10 μm. The drastic difference between the two types of capillary forces is due to the different deformation of the water-air interface, which in turn is determined by the force exerted on the three-phase contact line. The small floating particles are too light to create substantial deformation of the liquid surface. In the case of immersion forces, the particles are restricted in the vertical direction by the solid substrate. Then, as the film becomes thinner, the liquid surface deformation increases,

thus giving rise to a strong interparticle attraction. The deformation in this case is much larger than the one caused by the particle weight for similar floating particles.

Once the nucleus is formed, the second stage of crystal growth starts through directional motion of particles toward an ordered array. Evaporation of the solvent from within the micromenisci between the spheres causes water influx from outside, which is related to convective particle transport towards the nucleus.

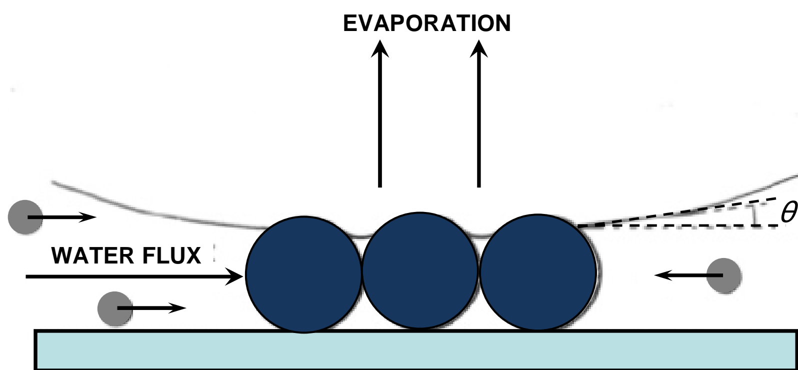

Figure 5.2 Convective flux toward the ordered phase due to the water evaporation from the menisci between the particles in the 2D array.

5.1.2 Self-assembly methods

Numerous methods for the production of colloid monolayers have been proposed in the literature, so only the most promising ones will be discussed.

5.1.2.1 Self-assembly nanospheres with spin-coating

Hulteen and Van Duyne [162] used a spin-coating procedure. The nanosphere lithography (NSL) masks were created by spin coating 264 nm polystyrene nanospheres onto the substrate of interest at 3600 rpm on a custom-built spin coater. The physical dimensions of the substrate were chosen to be in the range 0.25–1.0 cm^2 and the entire substrate is spin coated with nanospheres. The nanospheres were received from the manufacturer as a suspension in water, and then further diluted in a solution of the

surfactant Triton X-100/methanol (1:400 by volume) before spin coating. The surfactant was used to assist the solutions in wetting the substrate. Double-layer masks were created by increasing the nanosphere concentration in the spin coating solution as compared to the single-layer mask concentration. The specimen-to-specimen reproducibility of self-assembly layers mask preparation is excellent. For the D=264 nm nanospheres, 90% of the specimens were successfully coated with large domains of defect-free packing over the entire substrate surface reported by their paper.

5.1.2.2 Self-assembly nanospheres by tilting method

Self-assembly with the titling method was introduced by Micheletto et al [163]. In this method, adroplet of the colloid is applied to a carefully cleaned glass plate and the whole plate is enclosed in an airtight box. The evaporation rate is determined by a control circuit for temperature and ambient humidity. A nucleus is defined just by tilting the glass plate such that array formation starts at the upper edge and proceeds downwards. Monolayers consisting of particles down to 50 nm in size were successfully fabricated. Their depositions covered an area of about 1 cm^2, but in any sample only around half of the area was covered by monolayers. In the other half of the plate, evaporation takes place last, at the bottom of the sample. It is believed that in such regions the remaining water concentrates impurities and the excess particles, creating multilayers and clusters.

5.1.2.3 Continuous convective self-assembly nanospheres

Dimitrov and Nagayama [161] provided an approach for self-assembly of nanospheres which is more suitable for industrial applications. It works as follows: a glass plate is vertically dipped into a colloidal suspension and afterwards very slowly

withdrawn, as shown in figure 5.3.

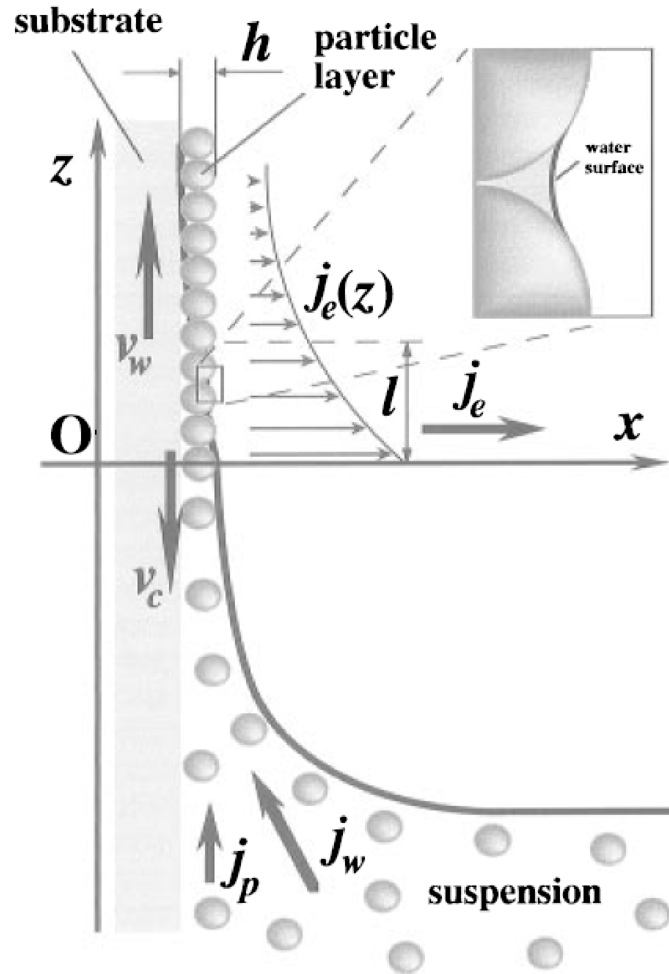

Figure 5.3 Sketch of the particle and water fluxes in the vicinity of monolayer particle arrays growing on a substrate plate that is being withdrawn from a suspension [161]

The inset shows the menisci shape between neighboring particles. Here, v_w is the substrate withdrawal rate, v_c is the array growth rate, j_w is the water influx, j_p is the respective particle influx, j_e is the water evaporation flux, and h is the thickness of the array. Again, temperature and ambient humidity are controlled. The thickness of the drying film, which is formed in a similar manner to one in a sol-gel process, could be adjusted to single, double, or triple layers, etc., just by measuring the optical transmission of the film and adapting the withdrawal speed accordingly. In this way, square-

centimeter-sized arrays were reproducibly obtained.

5.1.3 Experimental results on nanospheres self-assembly

The first two self-assembly methods, spin-coating and tilting, were used in this doctoral work. Both deposition methods require that the nanospheres are able to freely diffuse across the substrate, seeking their lowest-energy configuration. Therefore, before assembly, some additional preparations are needed. (1) Surfactant treatment: the nanosphere suspensions, from Bangs laboratories, Inc, has a solid percentage of 10% suspended in water, and then further diluted in a solution of the surfactant Triton X-100/methanol 1:400 by volume before used. The surfactant was used to assist the solutions in wetting the substrate; (2) Sample surface treatment: for hydrophobic cover glass slides, surface treatment is necessary to obtain mono layer self-assembly over large areas, the procedures are as follows: first, substrates were cleaned by immersion in 20% hydrochloric acid in ethanol for 30 minutes; second, the slides (or substrates) to be coated were dipped in a 2% 3-aminopropyltriethoxysilane (3APT) in acetone solution for 1 minute; then slides were dipped in water for 1minute and air dried.

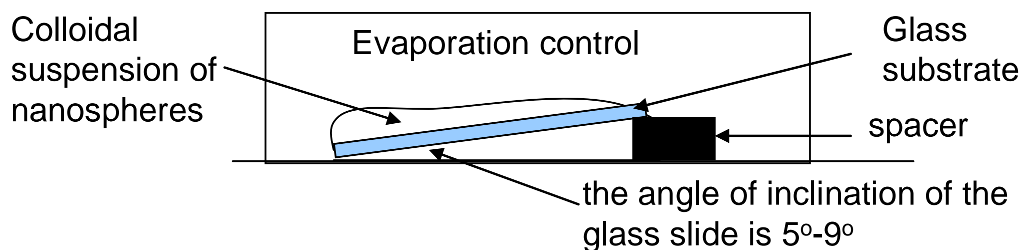

Figure 5.4 Sketch of nanospheres self-assembly by tilting.

Self-assembly by tilting method was firstly used as shown in figure 5.4. Cover lass

slides (18mm x18mm) were used as substrates. The substrates were tilted about 9° with respect to the horizontal. In this manner, the evaporation starts from the top of the sample on a horizontal border where evaporation takes place. This border then moves to the bottom of the sample until it is completely dry. The whole system was enclosed in a small plastic box (around 500 cm^3). From several experimental results, it was determined that the small volume helps to slow down the evaporation process, which takes approximately 4 hours to take place completely. The box also protects the surface from the external air flow, which can disturb the self-assembly process.

Figure 5.5 shows a series of microscopy images taken in different parts of self-assembly layer on glass substrate. The area about 2-3mm wide from top edge of the substrate (Part A) where the evaporation took place firstly was not fully covered by monolayer of nanospheres. A large grid of long stripes was formed because that the evaporation took place before enough nanosperes diffused across the substrate; on the center part of the substrate (Part B), a large and uniform monolayer was achieved by forming a sequence of crystal lattice shape pattern; on the bottom part of the substrate (Part C) where the evaporation took place last, multiple layers and clusters were formed due to concentration of excess nanospheres the remaining water.

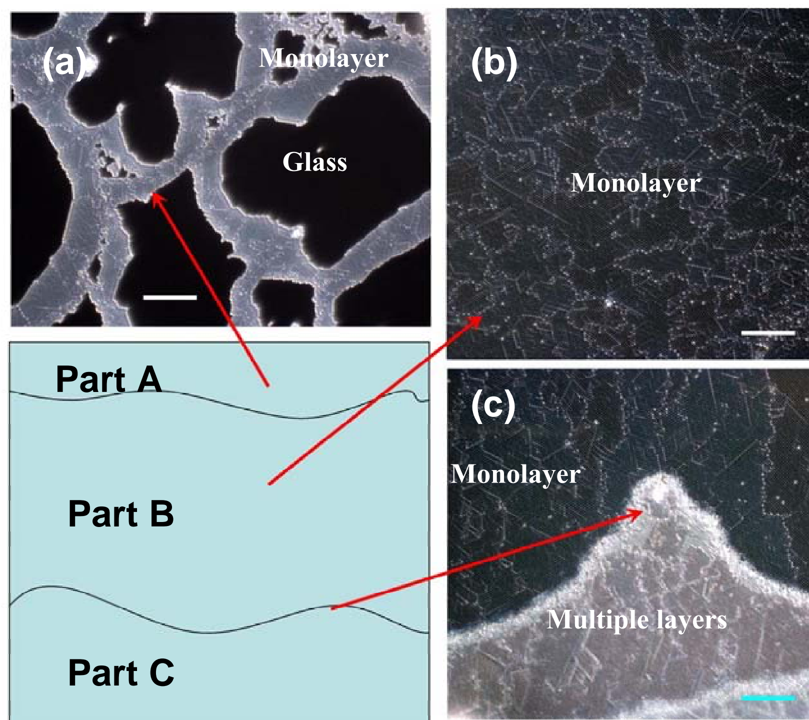

Figure 5.5 Microscopy images of different parts of self-assembly nanospheres layer on glass substrate by tilting method, scale bar is 20 μm.

Creating monolayers of nanospheres by spin-coating is simpler and faster than tilting method. For example, after 2 minutes spin-coating, the samples can be directly used for laser patterning. From a sequence of experiments, to create monolayer on cleaned glass or silicon surface, the spinning speed was determined to be 950-1000 rpm. For self-assembly of nanospheres on conductive films such as Poly(3,4-ethylenedioxy-thiophene)/poly(4-styrenesulfonic acid) (PEDOT-PSS) film, which were used for patterning in next part of this chapter, the spinning speed was 2200-2500 rpm.

Figure 5.6 shows the schematic of self-assembly sample by spin-coating. The entire substrate was covered by well assembled monolayer mixed randomly with a small amount of islands of multiple layers or particle clusters.

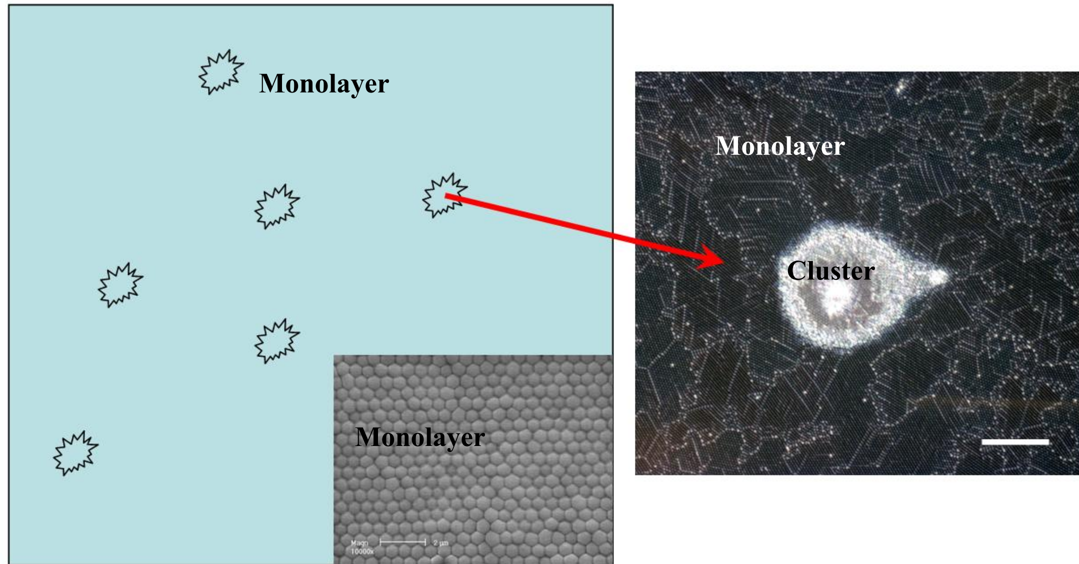

Figure 5.6 Microscopy images for the areas of interest on the glass substrate by spin-coating, scale bar is 20 μm.

Monolayers of nanospheres with diameters of 730nm, 550nm, 420nm were successfully created by both tilting and spin-coating methods as shown in Figure 5.7.

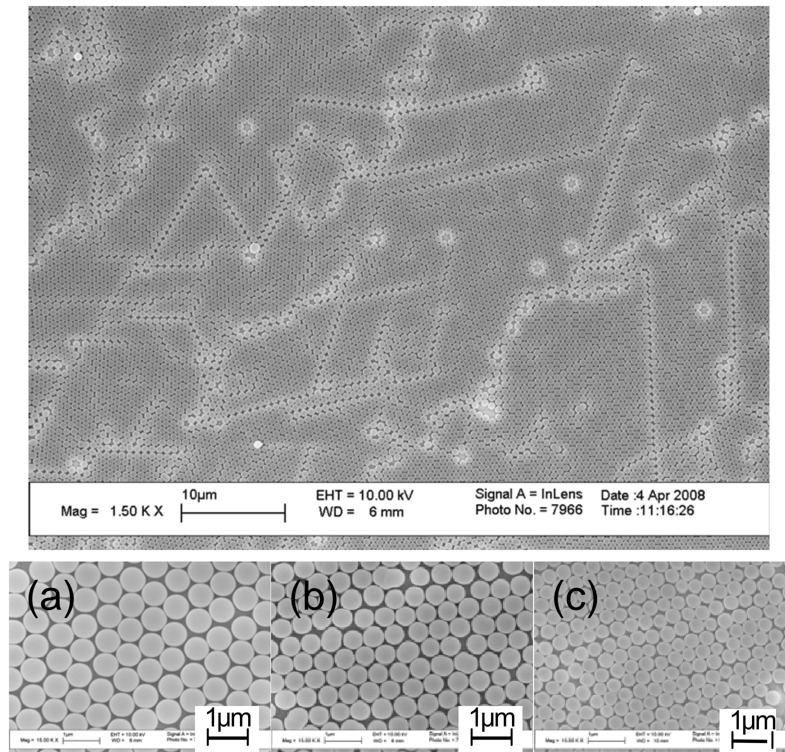

Figure 5.7 SEM micrograph of the monolayer of silica spheres with a diameter of (a)730nm, (b)550nm, (c)420nm.

5.2 Mie theory of laser-microsphere interaction for nanoscale Surface Modification

Mie theory, also called Lorenz-Mie theory or Lorenz-Mie-Debye theory is a complete analytical solution of Maxwell's equations for the scattering of electromagnetic radiation by spherical particles. The following section presents the typical situation for Mie theory of scattering, as shown in figure 5.8.

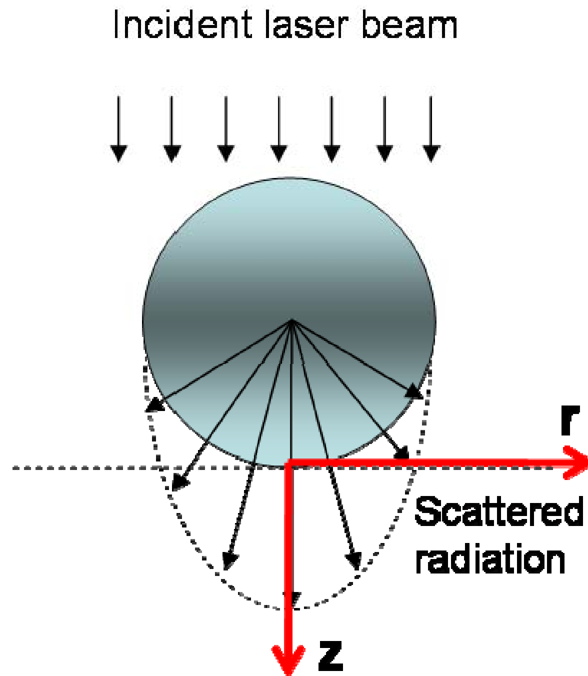

Figure 5.8 Schematic for particle scattering within the Mie theory.

The state of excitation which is established in space by the presence of electric charges is said to constitute an electromagnetic field. It is represented by two vectors, **E** and **B**, called electric vector and magnetic induction [164]. To describe the effect of the field on material objects, it is necessary to introduce a second set of vectors, the electric current density **j**, the electric displacement **D**, and the magnetic vector **H**.

Mie theory presents the solution of Maxwell equations for the scattering of a monochromatic electromagnetic wave with frequency ω by a sphere with radius α,

dielectric permittivity ε and magnetic permittivity μ, as follows:

$$\sqrt{\varepsilon} = n + i\kappa \tag{5.2}$$

where n is the real part of refractive index and κ is the complex part of refractive index. Equation 5.2 holds for the complex refractive index. Further we use indices "m" and "s" for quantities, which refer to the sphere and the surrounding media, respectively, so that:

$$\sqrt{\varepsilon_s} = n_s + i\kappa_s, \sqrt{\varepsilon_m} = n_m + i\kappa_m. \tag{5.3}$$

The electric and magnetic fields inside the sphere satisfy the vector Helmholtz equation:

$$\Delta \mathbf{E} + k^2\mathbf{E} = 0,\ \Delta \mathbf{H} + k^2\mathbf{H} = 0 \tag{5.4}$$

where $k = \frac{\omega}{c}\sqrt{\varepsilon}$ is the wave vector and Δ is 3D Laplacian. Similar equations with the wave vector $k_m = \frac{\omega}{c}\sqrt{\varepsilon_m}$ hold for the surrounding media. The boundary conditions on the surface include continuity of tangential components of **E** and **H**, and normal components of **D**=ε**E** and **B**=μ**H**.

Considering that the amplitude of the electric fileld vector of the incident plane wave is normalized to a unit, the wave propagates along the z-coordinate, the electric vector is directed along the x-coordinate, and the magnetic vector along the y-coordinate, in the spherical coordinate system with the origin situated at the sphere center, this plane wave can be expressed as:

$$\begin{aligned} &E_r = e^{ik_m r\cos\theta}\sin\theta\cos\varphi, E_\theta = e^{ik_m r\cos\theta}\cos\theta\sin\varphi, E_\varphi = e^{ik_m r\cos\theta}\sin\varphi, \\ &H_r = \sqrt{\varepsilon_m}e^{ik_m r\cos\theta}\sin\theta\cos\phi, H_\theta = \sqrt{\varepsilon_m}e^{ik_m r\cos\theta}\sin\theta\cos\phi, H_r = \sqrt{\varepsilon_m}e^{ik_m r\cos\theta}\sin\theta\cos\phi \end{aligned} \tag{5.5}$$

In terms of the spherical waves, the fields (5.5) are expressed as follows (index (i) indicates the incident wave):

$$
\begin{aligned}
E_r^{(i)} &= \frac{\cos\varphi}{(k_m r)^2}\sum_{l=1}^{\infty} i^{l-1}(2l-1)\psi_l(k_m r)P_l^{(1)}(\cos\theta),\\
E_\theta^{(i)} &= -\frac{\cos\varphi}{k_m r}\sum_{l=1}^{\infty} i^{l-1}\frac{(2l-1)}{l(l+1)}\left[\psi_l'(k_m r)P_l^{(1)'}(\cos\theta)\sin\theta - i\psi_l(k_m r)\frac{P_l^{(1)}(\cos\theta)}{\sin\theta}\right],\\
E_\varphi^{(i)} &= -\frac{\sin\varphi}{k_m r}\sum_{l=1}^{\infty} i^{l-1}\frac{(2l-1)}{l(l+1)}\left[\psi_l'(k_m r)\frac{P_l^{(1)}(\cos\theta)}{\sin\theta} - i\psi_l(k_m r)P_l^{(1)'}(\cos\theta)\sin\theta\right],\\
H_r^{(i)} &= \frac{\sqrt{\varepsilon_m}\sin\varphi}{(k_m r)^2}\sum_{l=1}^{\infty} i^{l-1}(2l-1)\psi_l(k_m r)P_l^{(1)}(\cos\theta),\\
H_\theta^{(i)} &= i\frac{\sin\varphi}{k_m r}\sum_{l=1}^{\infty} i^{l-1}\frac{(2l-1)}{l(l+1)}\left[\psi_l(k_m r)\frac{P_l^{(1)}(\cos\theta)}{\sin\theta} - i\psi_l'(k_m r)P_l^{(1)'}(\cos\theta)\sin\theta\right],\\
H_\varphi^{(i)} &= -i\frac{\sin\varphi}{k_m r}\sum_{l=1}^{\infty} i^{l-1}\frac{(2l-1)}{l(l+1)}\left[\psi_l(k_m r)P_l^{(1)'}(\cos\theta)\sin\theta - i\psi_l'(k_m r)\frac{P_l^{(1)}(\cos\theta)}{\sin\theta}\right]
\end{aligned}
\tag{5.6}
$$

where the radial dependence is expressed through the Bessel function (regular at $\rho = 0$) and prime indicates differentiation:

$$
\psi_l(\rho) = \sqrt{\frac{\pi\rho}{2}}J_{l+\frac{1}{2}}(\rho),\ \ \psi_l'(\rho) = \frac{\partial\psi_l(\rho)}{\partial\rho}
\tag{5.7}
$$

The angular dependence in (5.6) is related to spherical functions, where $P_n^m(x)$ are associated Legendre polynomials.

The Mie solution of scattering results in the rigorous solution to Maxwell's equations describing the scattered electromagnetic field components (indication index (s)) as follows:

$$
\begin{aligned}
E_r^{(s)} &= \frac{\cos\varphi}{(k_m r)^2}\sum_{l=1}^{\infty} l(l+1)\ {}^{e}B_l \zeta_l(k_m r) P_l^{(1)}(\cos\theta), \\
E_\theta^{(s)} &= -\frac{\cos\varphi}{k_m r}\sum_{l=1}^{\infty} i^{l-1}\left[{}^{e}B_l \zeta_l'(k_m r) P_l^{(1)}{}'(\cos\theta)\sin\theta - i\ {}^{m}B_l \zeta_l(k_m r)\frac{P_l^{(1)}(\cos\theta)}{\sin\theta}\right], \\
E_\varphi^{(s)} &= -\frac{\sin\varphi}{k_m r}\sum_{l=1}^{\infty} i^{l-1}\left[{}^{e}B_l \zeta_l'(k_m r)\frac{P_l^{(1)}(\cos\theta)}{\sin\theta} - i\ {}^{m}B_l \zeta_l(k_m r) P_l^{(1)}{}'(\cos\theta)\sin\theta\right], \\
H_r^{(s)} &= \frac{\sqrt{\varepsilon_m}\sin\varphi}{(k_m r)^2}\sum_{l=1}^{\infty} l(l+1)\ {}^{m}B_l \zeta_l(k_m r) P_l^{(1)}(\cos\theta), \\
H_\theta^{(s)} &= i\frac{\sin\varphi}{k_m r}\sum_{l=1}^{\infty} i^{l-1}\left[{}^{e}B_l \zeta_l(k_m r)\frac{P_l^{(1)}(\cos\theta)}{\sin\theta} - i\ {}^{m}B_l \zeta_l'(k_m r) P_l^{(1)}{}'(\cos\theta)\sin\theta\right], \\
H_\varphi^{(s)} &= -i\frac{\sin\varphi}{k_m r}\sum_{l=1}^{\infty} i^{l-1}\left[{}^{e}B_l \zeta_l(k_m r) P_l^{(1)}{}'(\cos\theta)\sin\theta - i\ {}^{m}B_l \zeta_l'(k_m r)\frac{P_l^{(1)}(\cos\theta)}{\sin\theta}\right]
\end{aligned}
\tag{5.8}
$$

where

$$
\zeta_l(\rho) = \rho h_l^{(1)}(\rho), \zeta_l'(\rho) = \frac{\partial \zeta_l(\rho)}{\partial \rho} \tag{5.9}
$$

$$
\begin{aligned}
{}^{e}B_l &= il+1\frac{2l+1}{l(l+1)}\frac{\psi_l'(y)\psi_l(x) - m\psi_l(y)\psi_l'(x)}{\psi_l'(y)\varsigma_l(x) - m\psi_l(y)\varsigma_l'(x)}, \\
{}^{m}B_l &= il+1\frac{2l+1}{l(l+1)}\frac{m\psi_l'(y)\psi_l(x) - \psi_l(y)\psi_l'(x)}{m\psi_l'(y)\varsigma_l(x) - \psi_l(y)\varsigma_l'(x)}
\end{aligned}
\tag{5.10}
$$

There is a well-known problem for computer calculations and related to the cutting of sums in (5.6) by value $l \le l_{\max}$. The recommended values in [165] are given by:

$$
l_{cutoff} = \frac{2\pi a n}{\lambda} + 4 \tag{5.11}
$$

The time-averaged Poynting vector, **S**, which is the energy density, is defined as:

$$
\mathbf{S} = \frac{c}{8\pi}\mathrm{Re}\,[\mathbf{E}\times\mathbf{H}^*] \tag{5.12}
$$

where the star indicates the complex conjugate. The incident wave (5.5) produces a constant vector field, directed along the z-axes. This flux is characterized by intensity I_o = Abs[$\mathbf{S}^i$]=c/8π. This value is used further for normalization. The energy field can be

presented by calculating the spherical components of the time-averaged Poynting vector:

$$
\begin{aligned}
S_r &= \frac{c}{8\pi}\mathrm{Re}[E_\theta H_\varphi * - E_\varphi H_\theta *] = I_0 \,\mathrm{Re}[E_\theta H_\varphi * - E_\varphi H_\theta *], \\
S_\theta &= \frac{c}{8\pi}\mathrm{Re}[E_\varphi H_r * - E_r H_\varphi *] = I_0 \,\mathrm{Re}[E_\varphi H_r * - E_r H_\varphi *], \\
S_\varphi &= \frac{c}{8\pi}\mathrm{Re}[E_r H_\theta * - E_\theta H_r *] = I_0 \,\mathrm{Re}[E_r H_\theta * - E_\theta H_r *],
\end{aligned} \tag{5.13}
$$

The z-direction is taken longitudinal to the incident laser and normal to the substrate lying beneath the particle. The z-component of the Poynting vector is therefore a description of the energy incident upon the substrate surface due to the laser and the presence of the microsphere. The coordinate convention used dictates the z-component equal to

$$S_z = \cos\theta \, S_r - \sin\theta \, S_\theta \tag{5.14}$$

So the relative intensity can be expressed as

$$R = \frac{S_z}{I_0} = \cos\theta \frac{S_r}{I_0} - \sin\theta \frac{S_\theta}{I_0} \tag{5.15}$$

Equation 5.15 shows the near-field enhancement due to the spheres compared with the incident laser energy.

Figure 5.9 shows the intensity distribution on the substrate with parameters: diameter of silica spheres 2α=800nm, refraction index of the sphere n=1.37, incident laser wavelength λ=532nm, 355nm and 266nm. The resulting peak intensities predicted is 11.97, 8.03, and 3.92 times the incident intensities. Figure 5.10 shows the intensity distribution incident by 355nm laser. Three different sizes of spheres were used to simulate. From the calculation, the intensity enhancement is a radially symmetric distribution.

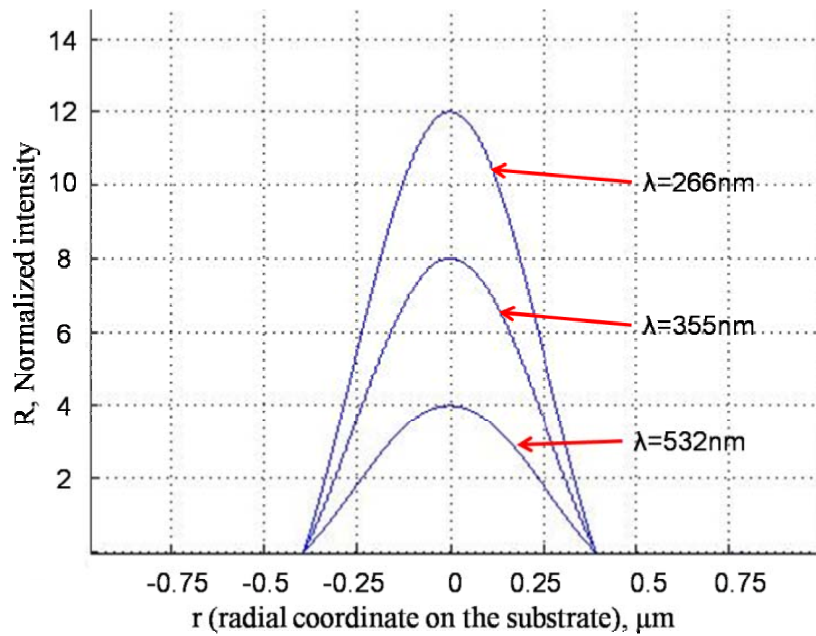

Figure 5.9 The light intensity distributions on the surface under 800nm silica spheres. Three wavelength were used to simulate: 532nm, 355nm, and 266nm.

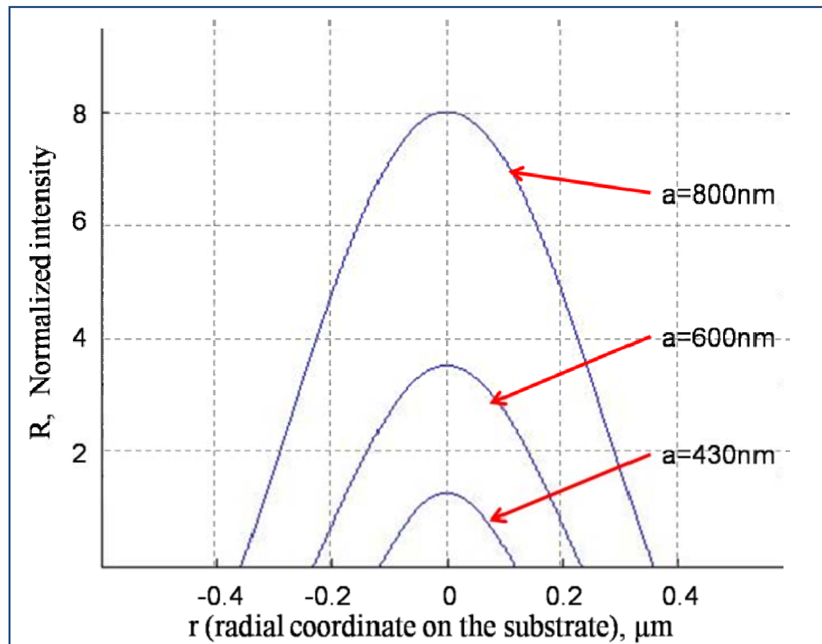

Figure 5.10 The light intensity distributions on the surface incident by 355nm laser under silica spheres with diameters of 800nm, 600nm and 430nm.

5.3 Experimental procedure

5.3.1 Materials and sample preparation

Thin films of Poly(3,4-ethylene dioxythiophene)-poly(styrenesulfonate) (PEDOT-PSS) were used as substrates for patterning. Gold-palladium thin films were sputtered on tin-doped indium oxide (ITO) substrates (5 x 10 mm2). Subsequently, PEDOT-PSS conducting polymers were electrochemically deposited using PSS (0.2% w/v) and ethylene dioxythiophene (EDOT) (0.1% w/v) solutions. The polymerization was carried out galvanostatically by applying a 100 μA current using a potentiostat. By varying the deposition time, and thus the total deposition charge, PEDOT-PSS films of different thicknesses were fabricated. Films with thickness of 60nm, 300nm, 600nm and 3μm were used in the experiments

Three different sizes of silica nanospheres suspensions (800nm, 600nm, 430nm Bangs Laboratories Inc.) to be used for inducing near-field enhancement effect were mixed with a surfactant (triton-X: methanol =1:400) in a 2:1 volume ratio. The suspensions have a solid percentage of 10% suspended in water.

5.3.2 Laser-induced near-field patterning experimental setup and sample characterization

5.3.2.1 Experimental setup

A schematic of the experimental setup is shown in Figure 5.11. A commercial Nd:YAG laser (Quanta-Ray PRO 290, Spectra Physics) was used the laser near-field patterning experiments. The samples were irradiated at 355 nm with pulses lasting 10 ns at normal incidence. Because the laser beam was not focused, the patterning area was

approximately 1.5 cm^2. All the samples were irradiated at ambient conditions of temperature and pressure. The frequency of the laser was 10 Hz. The single pulses incident on the sample were controlled using an optical shutter (Uniblitz Electronic VS25S2ZMO) with time resolution of 10µs.

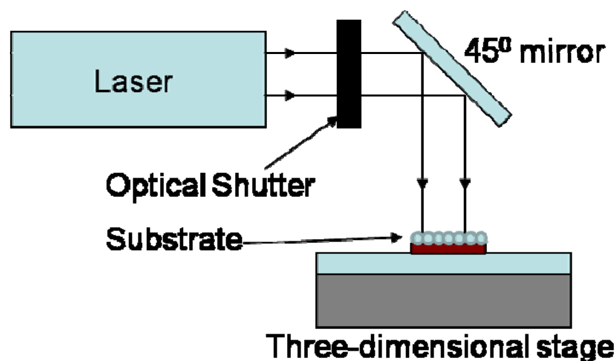

Figure 5.11 Schematic set-up for laser induced near-field patterning.

5.3.2.2 Sample characterization

The patterned samples were imaged using a high-resolution scanning electron microscope (SEM) with an operating voltage of 10 kV (LEO 1530 Thermally-Assisted Field Emission microscope). All samples were coated with 2 nm gold/palladium layer to improve the electrical conductivity, prior to imaging.

5.4 Results and discussion

Nanodent structures with sizes ranging from 400nm-200nm were patterned on PEDOT-PSS films by single pulse irradiation of the laser using self-assembly nonolayers of nanospheres 800nm, 600nm and 430nm in diameter. Both single laser beam and two interfering laser beams were used to conduct patterning, as shown in the following section.

5.4.1 Single beam incidence laser-induced near-field patterning

In these experiments, it was found that most of the silica nanospheres were removed from the substrate surface with single beam incidence. Figure 5.12 shows a SEM image of the film obtained following the irradiation with one pulse of 70mJ/cm^2 using 800nm nanospheres. An array of cavity nanostructures was formed on the film. At higher magnification, the SEM analysis reveals that the diameter of the cavities is about 350nm. In figure 5.12 (b), the seven cavities composed a hexagon with one cavity in the center, the distance between two adjacent cavities is 800nm, the diameter of the silica nanosphere used for near-field patterning. The entire patterned area is approximately 1.5cm^2.

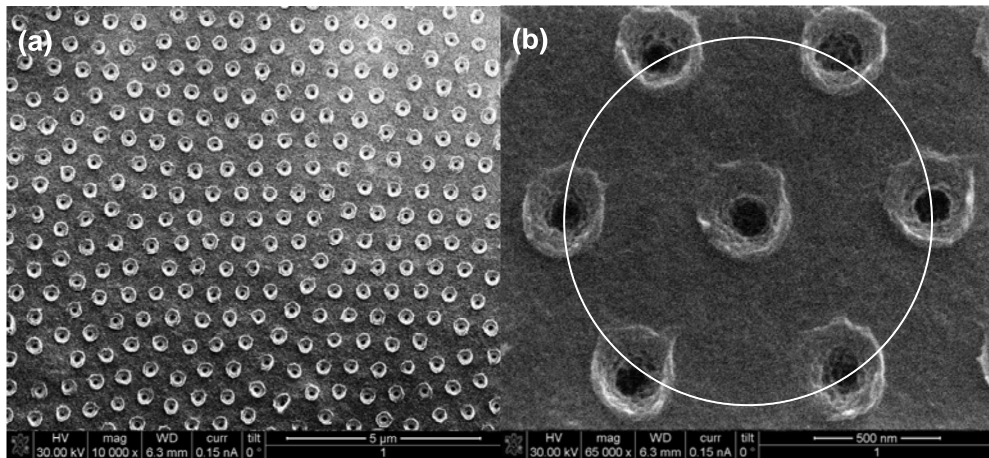

Figure 5.12 SEM images of cavity arrays formed after laser irradiation of 0.80 μm silica particles on a thin PEDOT film by a single laser pulse with a fluence of 70 mJ/cm^2.

Figure 5.13 shows the SEM images of the patterns formed on the PEDOT film at the same laser fluence but with different nanosphere sizes, e.g. laser fluence: 80 mJ/cm^2 and (a) 800nm, x (b) 600nm, and x (c) 430nm, respectively. From Figures 5.13 (a)–5.13 (c), it can be observed that the cavities sizes are proportional to the diameter of the nanospheres. For example with the same laser fluence, the diameters of cavities patterned with 800nm nanospheres are approximately 400nm, with 600nm nanospheres are

approximately 300nm, and with 430nm nanospheres are approximately 250nm.

Figure 5.14 and figure 5.15 show the SEM images of nanodent structures formed on the PEDOT-PSS film under the removed 800nm and 600nm particles, respectively, after one laser pulse irradiation at the following laser fluences: 5.14 (a) 110 mJ/cm^2, 5.14 (b) 86 mJ/cm^2, and 5.14 (c) 60 mJ/cm^2 and 5.15 (a) 84 mJ/cm^2, 5.15 (b70 mJ/cm^2, 5.15(c) 56 mJ/cm^2, and 5.15 (d) 29 mJ/cm^2.

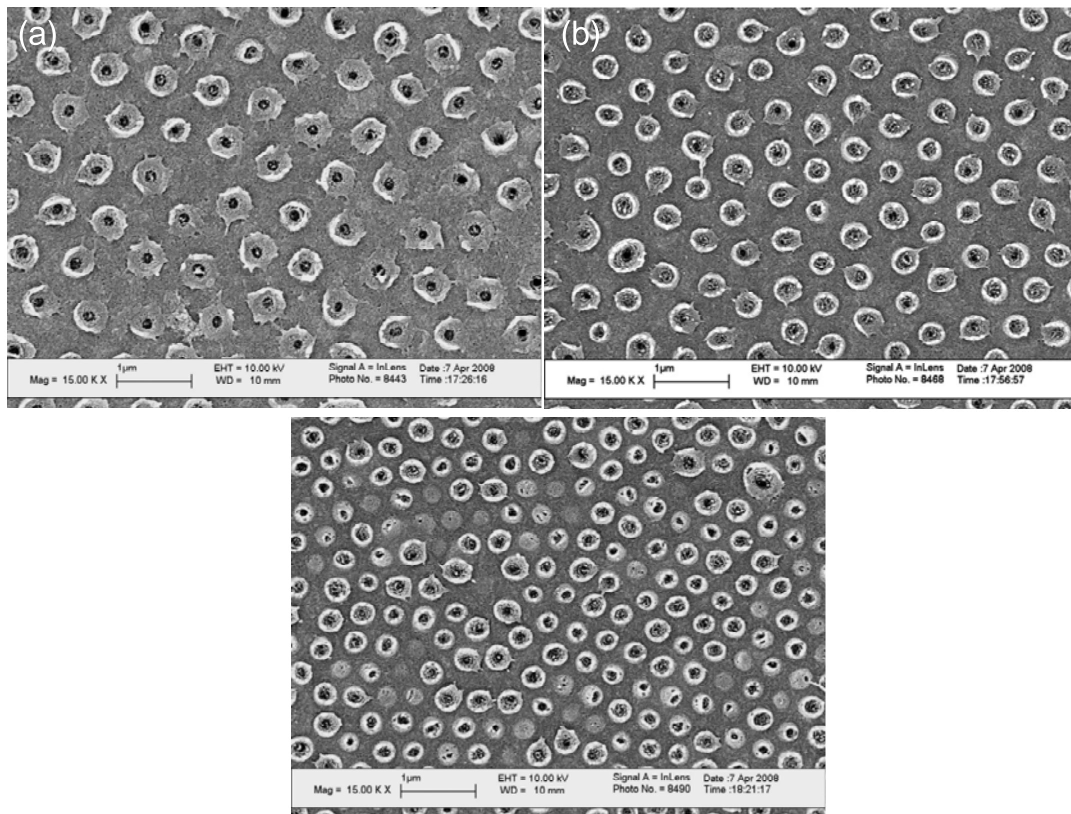

Figure 5.13 SEM images of cavity arrays formed at different sizes of nanospheres and the same laser fluences 80mJ/cm^2 (a) 800nm, (b) 600nm and (c) 430nm.

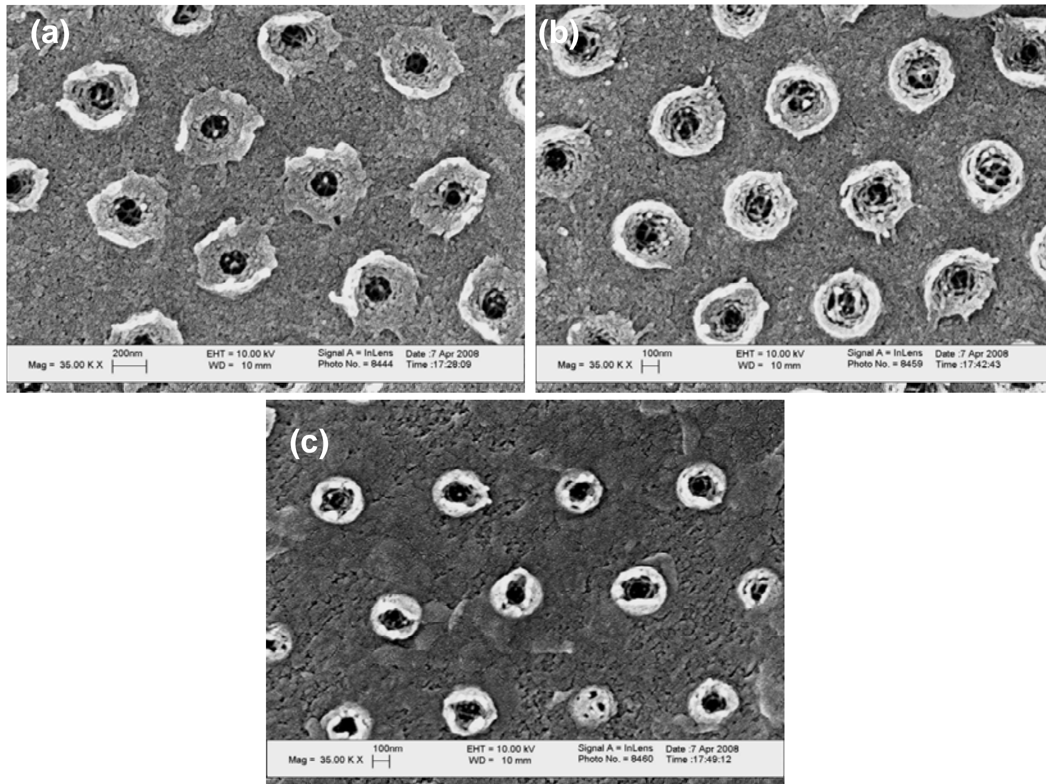

Figure 5.14 SEM images of cavity arrays formed by different laser fluences with 800nm nanospheres, (a) 110 mJ/cm^2, (b) 84mJ/cm^2 and (c) 60mJ/cm^2.

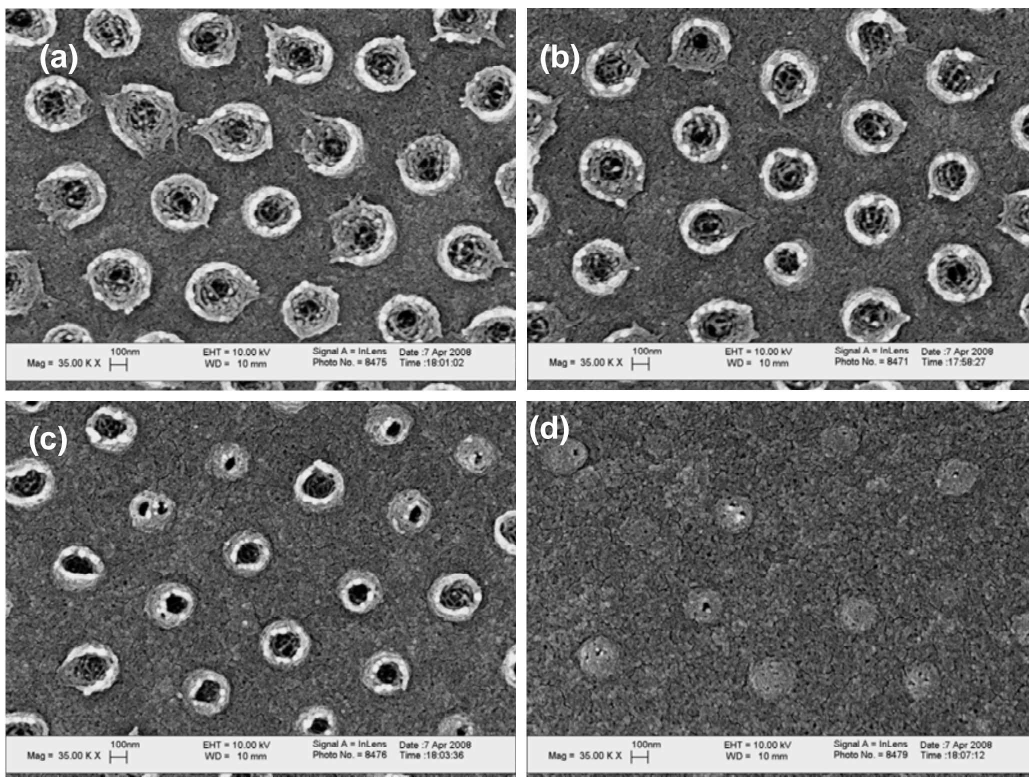

Figure 5.15 SEM images of cavity arrays formed by different laser fluences with 600nm nanospheres, (a) 84 mJ/cm^2, (b) 70mJ/cm^2, (c) 56mJ/cm^2 and (d) 29mJ/cm^2.

From figure 5.14 and 5.15, it can be seen that the sizes of the cavities are proportional to the laser fluences, which is coincident with the simulation in section 5.2. Figure 5.15 (d) shows the threshold laser fluence for 600nm patterning on PEDOT-PSS is 29mJ/cm^2.

5.4.2 laser-induced near-field patterning with interference beam

The intensity distribution of two interfering laser beams is given by equation 4.10, and the distribution pattern is shown in figure 4.2. When this periodic line-like pattern was used instead of single laser beam to irradiate the PEDOT-PSS film with a self-assembled monolayer of nanospheres on the top, linear periodic nanodent structures were created, as shown in figure 5.16.

Figure 5.17 and figure 5.18 shows SEM images of nanodent structures formed on the PEDOT-PSS film under the removed 800nm and 600nm particles, respectively, after one laser pulse irradiation at laser fluences of 5.17 (a) 52 mJ/cm^2, 5.17 (b) 38 mJ/cm^2, 5.17 (c) 18 mJ/cm^2, and 5.17 (d) 6 mJ/cm^2 and 5.18 (a) 110mJ/cm^2, 5.18 (b) 92mJ/cm^2, 5.18 (c) 76 mJ/cm^2, and 5.18 (d) 47 mJ/cm^2.

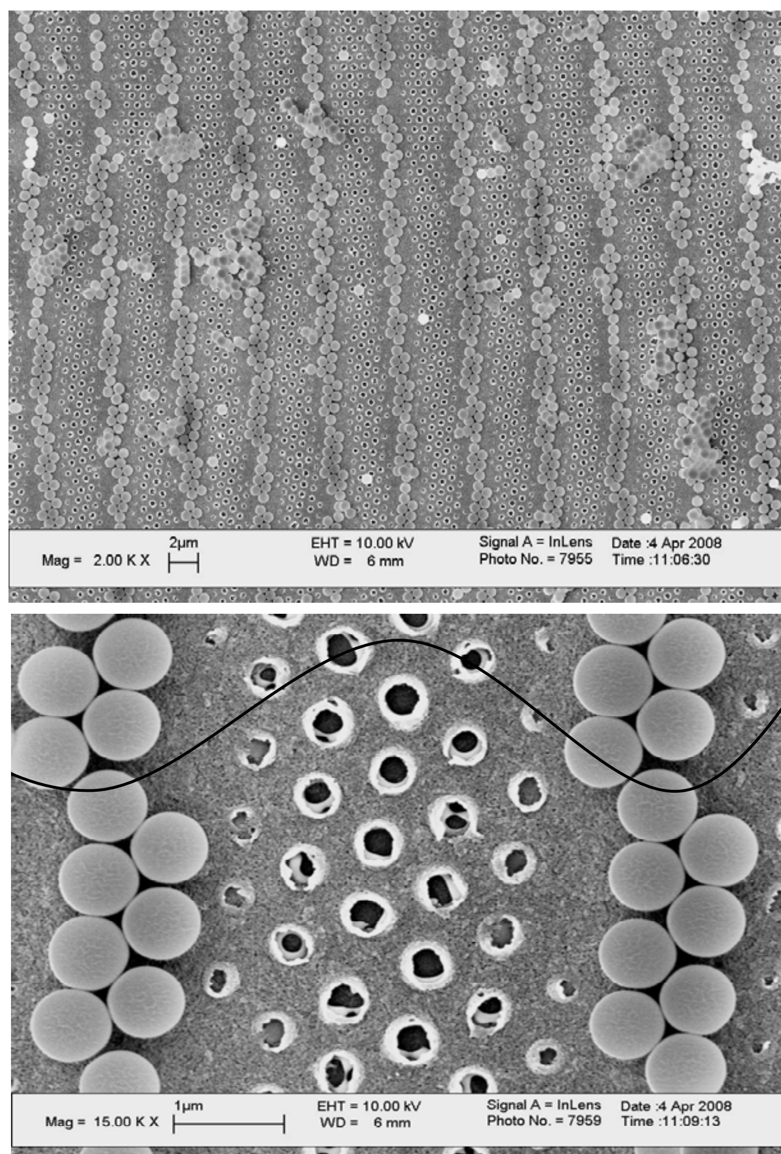

Figure 5.16 SEM images of periodic cavity arrays formed after laser irradiation of 0.80 μm silica particles on a thin PEDOT film by two interfered laser beam with single pulse of fluence: 18 mJ/cm^2.

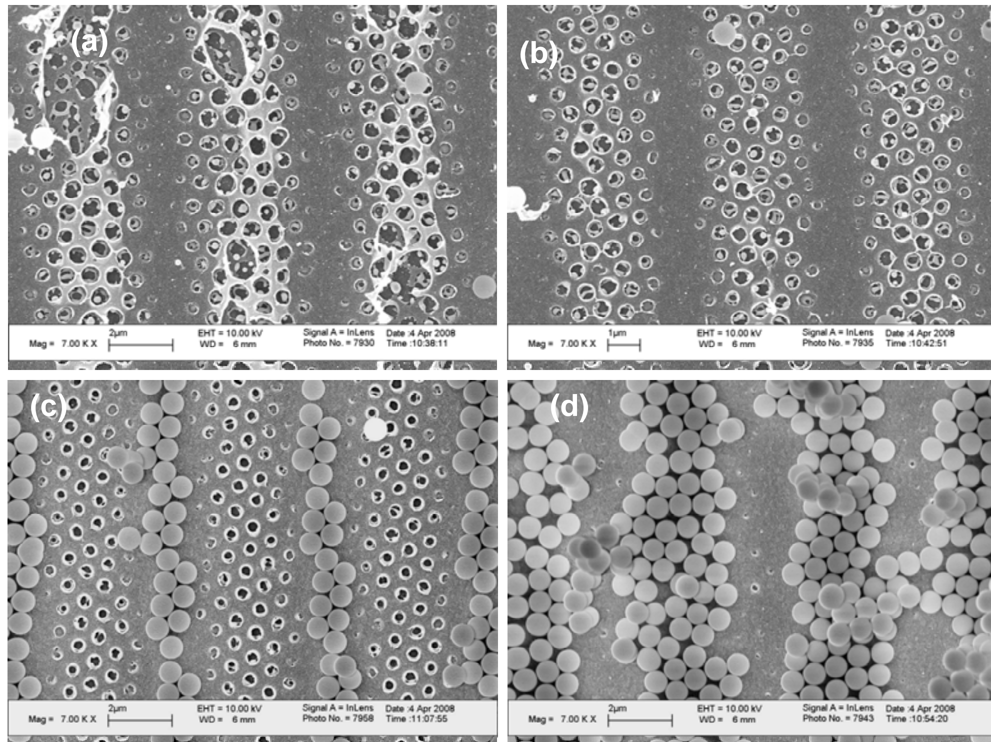

Figure 5.17 SEM images of periodic cavity arrays formed by different laser fluences with 800nm nanospheres, (a) 52mJ/cm^2, (b) 38mJ/cm^2, (c) 18mJ/cm^2, (d) 6mJ/cm^2.

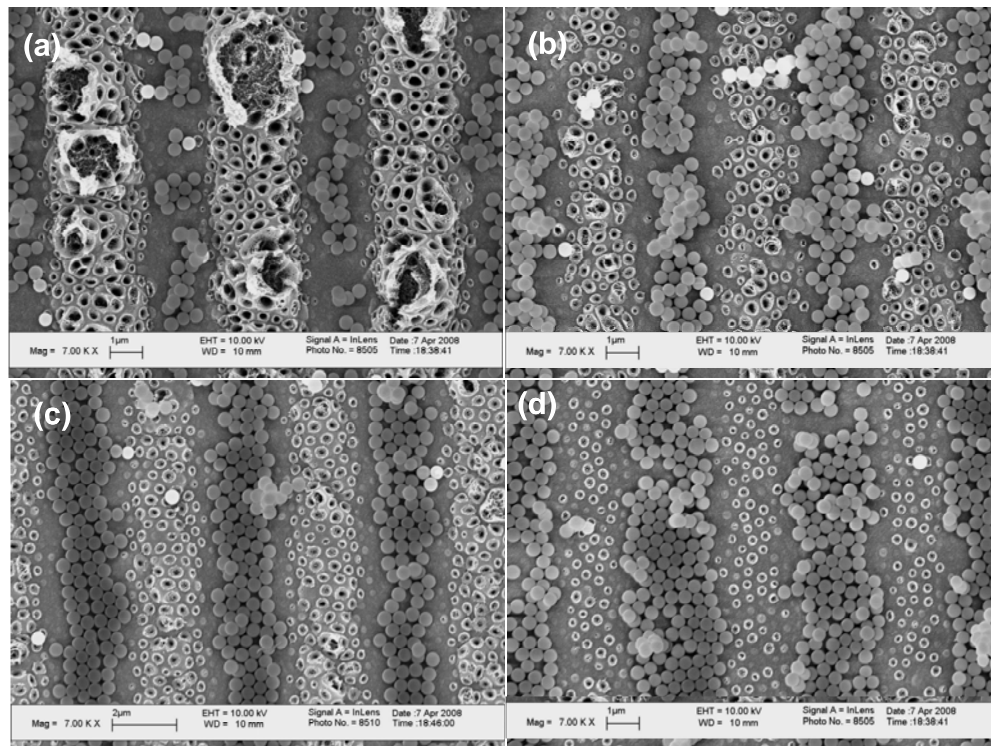

Figure 5.18 SEM images of periodic cavity arrays formed by different laser fluences with 430nm nanospheres, (a) 110 mJ/cm^2, (b) 92mJ/cm^2, (c) 76mJ/cm^2, (d) 47mJ/cm^2.

From figure 5.17 and 5.18, it can be observed that the width of patterned areas increased while increasing laser fluence. The laser fluence distribution for two beams interference patterning is shown in figure 4.2 in section 4.1, which can explain why the sizes of nano-cavity in the center of patterned areas are larger than those on the edge.

5.5 Summary and Conclusions

In this chapter, an analytical and experimental investigation on the features created on PEDOS-PSS thin films by the irradiation of nanospheres on the substrate surface with a pulsed laser is presented. A patterning system, with a frequency-tripled Nd:YAG laser (wavelength 355nm), beam delivery system, and optical shutter, was designed and realized. A monolayer of silica particles, with different diameters of 430nm, 600nm and 800nm, was deposited on a PEDOS-PSS film by self-assembly. Nanodent structures were patterned after laser irradiation on the nanospheres/PEDOS-PSS structure with a single shot. The features indicate an enhancement of the incident intensity in the near-field due to the presence of the sphere. The near field was calculated for a single sphere on a substrate using the results of Mie theory. From the calculations, the intensity enhancement can reach to 12 times for particle diameter 800nm and incident laser wavelength 355nm. Periodic nano-cavity arrays were patterned by combining direct laser interference technology and laser induced near-field technology.

CHAPTER VI

CONCLUSIONS

This doctoral dissertation investigated four techniques for enabling maskless and direct-write micro/nanofabrication. These are: (1) Direct-write laser micromachining of polymethyl methacrylate (PMMA) by CO_2 laser ablation; (2) Direct-write laser photopolymerization using a frequency-doubled Nd:YAG laser; (3) Direct laser interference patterning; and (4) Laser-induced near-field patterning. Microfabrication techniques utilizing masks or masters for replications have the drawbacks of high cost and long delay in making the template. In contrast, the four techniques described in this dissertation described in this dissertation are highly flexible with respect to the pattern types that can be written and the substrate types that can be patterned and processed. For example, these techniques are able to write patterns of arbitrary geometry on various polymeric substrates directly from a digital representation. The costs of the tools for these techniques are also comparatively low, especially for research applications.

6.1 Direct-write laser micromaching of polymethyl methacrylate (PMMA) by CO2 laser ablation

6.1.1 Summary and conclusions

Laser micromachining of channels in PMMA using a continuous wave CO_2 laser

was investigated experimentally and theoretically. Heat transfer models for the channel depth, channel profile, laser power and scanning speed were developed and applied in this work. These models, based on the heat balance in microchannel fabrication, are in excellent agreement with experimental results, with a maximum deviation of approximately 5% for the range of experimental parameters (laser power, scanning speed) tested. Within this range of parameters tested, these models can be used to accurately predict the micromachined channel depth and profile for a specific choice of laser power and scanning speed in PMMA. These models are also applicable to other polymers that have similar ablation characteristics, with the knowledge of their threshold fluence. Therefore, these models can eliminate the need for elaborate experimentation to characterize the attainable range of channel depths and profiles with a given CO_2 laser micromachining system whose laser beam characteristics (intensity profile, beam divergence, and $1/e^2$ beam radius) are known.

6.1.2 Scientific and Technical Contributions

(a) A direct-write laser microfabrication system for polymethyl methacrylate (PMMA) microfluidic chip was developed.

(b) Microchannels with 44μm-240μm wide and 22μm-130μm deep were fabricated with CO_2 laser.

(c) Accurate physical models were developed for the depth and channel profile of ablated channels based on heat balance in microchannel fabrication.

6.2 Direct-write laser polymerization using a frequency-doubled Nd:YAG laser

6.2.1 Summary and conclusion

An advanced laser-direct write system was developed, consisting of a frequency doubled Nd: YAG laser, a beam delivery system, computer controlled x–y–z stage with nanometer resolution, a CAD design tool, and an *in situ* process monitoring system. This system is capable of fabricating a line width as fine as 840nm. A numerical model based on the Monte Carlo method was developed to simulate light scattering and absorption in photocrosslinkable materials. The influence of critical process parameters was studied through the developed numerical model. In this study, the experimental measurements of curing depth and curing width were found to be in good agreement with the numerical modeling. The successful fabrication of square-, circular-, and honeycomb-cellular structures demonstrated its unique capability of fabricating micro-patterns with arbitrary shapes, and in a wide variety of functional materials. For the first time, sub-micron feature resolution in PETIA and 3μm resolution in PEG-DA were successfully realized by laser direct-writing.

6.2.2 Scientific and Technical Contributions

(a) A direct-write laser polymerization system using frequency-doubled Nd:YAG laser was developed. This system has sub-micron resolution three-dimensional fabrication ability. Based on this system, more precise structures can be fabricated.

(b) Functional structures were fabricated with different photocrosslinkable materials. Structures of a biocompatible hydrogel, PEG-DA, were for the first time fabricated with 3μm resolution by laser direct-writing.

(c) A numerical model based on the Monte Carlo method was developed. This model can precisely predict the cured profile of single-shot exposure in the photopolymerization process.

6.3 Direct laser interference patterning

6.3.1 Summary and conclusion

A method was developed for rapid and large-area fabrication of two-dimensional and three-dimensional periodic structures on photopolymerizable materials with 10ns pulses from a frequency-tripled Nd:YAG laser emitting at 355 nm. Surface areas up to 3.6 cm^2 were patterned in one second showing the high fabrication speeds that can be reached. A concentration of 10 % w/w of the photoinitiator (N-MDEA) was shown to be appropriate to achieve the lowest dose necessary to polymerize PETIA, thus increasing the patterning speed. Different periodic structure arrays including line-, cross-, honeycomb- and dot-like structures were fabricated. When using relatively thick layers of the PETIA solutions, due to the lower mechanical properties of the polymer, the lines fell over sideways during the development process. This problem could be solved with a double exposure process with angles of 45 or 90°, or when thinner layers of the PETIA solution were used. Particularly, for the 45° case, self organization driven processes, probably due to non-axial shrinkage of the polymer, were observed, resulting in a honeycomb-like structure. For samples irradiated with three beams, by tuning the laser intensity or number of laser pulses, it was possible to fabricate different types of periodic arrays from isolated dots to symmetric honeycomb structures. Additionally, it was shown that by changing the intensity of the individual laser beams, other types of periodic patterns could be also fabricated. These

patterns are consistent with predictions of light intensity distributions. Three-dimensional line-like structures were for the first time successfully fabricated in SU-8 a negative photoresist, with the use of an absorber, TINUVIN 384-2. Concentrations of 1%-2% by weight of absorber were found to be appropriate to achieve massive and stable three-dimensional structures. By adjusting the separation angle between two incident beams, sub-microm line-like patterns were realized with Shipley 1813, a positive photoresist.

6.3.2 Scientific and Technical Contributions

(a) A direct laser interference patterning system with a frequency-tripled Nd:YAG laser, beam delivery system, and optical shutter was developed.

(b) PETIA with different concentration of photoinitiator (N-MDEA) was used to investigate the relationship between laser exposure and the percentage of photoinitiator. Different periodic structures, such as line-, cross-, honeycomb- and dot-like structures, were fabricated using PETIA.

(c) Three-dimensional patterns with SU-8 and absorber TINUVIN 384-2 were for the first time realized.

(d) Line-like structures with sub-micron periods were achieved by two laser beam interference on Shipley 1813.

6.4 Laser-induced near-field patterning

6.4.1 Summary and conclusion

This work explored pulsed laser-induced near-field patterning through a monolayer of self-assembled nanospheres acting as near-field enhancing lenslets. Nanoscale features were created using this technique on Poly(3,4-ethylene dioxythiophene)-

poly(styrenesulfonate) (PEDOT-PSS) thin films. The features produced indicated an enhancement of the incident intensity in the near-field due to the presence of the nanospheres. The near-field was calculated for a single sphere on a substrate using Mie theory. The results of these calculations predicted a strong enhancement directly under the sphere, which is assumed to be responsible for the substrate damage restricted to a sub-diffraction-limited area. Periodic nano-cavity arrays were for the first time patterned by combining direct laser interference technology and laser induced near-field technology.

6.4.2 Scientific and Technical Contributions

(a) A laser-induced near-field patterning system was developed, which can realize nano-cavity arrays on up to 3cm^2 area with single-shot laser exposure.

(b) Different sizes of nano-cavity arrays were patterned on Poly(3,4-ethylene dioxythiophene)-poly(styrenesulfonate) (PEDOT-PSS) with different laser fluences and different sizes of silica nanospheres. These samples can be used for biodetectors, flexible photovoltaics, as well as batteries.

(c) Periodic nano-cavity arrays were for the first time patterned by combining direct laser interference technology and laser induced near-field technology.

(d) An analytical model based on Mie theory was developed to predict the near-field intensity enhancement and intensity distributions on the substrate.

BIBLIOGRAPHY

[1] Zhao, X.M., Xia, Y., Whitesides, G.M. (1996) Fabrication of three-dimensional micro-structures: Microtransfer molding. Advanced Materials 8: 837-840.

[2] Kim, E., Xia, Y., Zhao, X.M., Whitesides, G.M. (1997) Solvent-assisted microcontact molding: A convenient method for fabricating three-dimensional structures on surfaces of polymers. Advanced Materials 9: 651-654.

[3] Chou, S.Y. (2001) Nanoimprint lithography and lithographically induced self-assembly. MRS Bulletin 26: 512-517.

[4] Biebuyck, H.A., Larsen, N.B., Delamarche, E., Michel, B. (1997) Lithography beyond light: Microcontact printing with monolayer resists. IBM Journal of Research and Development 41: 159-170.

[5] Nicholas L. Abbott, J.P.F., and George M. Whitesides (1992) Manipulation of the Wettability of Surfaces on the 0.1- to 1 -Micrometer Scale Through Micromachining and Molecular Self-Assembly. Science 257: 1380-1382.

[6] Jones, R.G., Miller Tate, P.C. (1994) Electron beam and X-ray resists. Advanced Materials for Optics and Electronics 4: 139-153.

[7] Tseng, A.A., Kuan, C., Chen, C.D., Ma, K.J. (2003) Electron beam lithography in nanoscale fabrication: recent development. IEEE Transactions on Electronics Packaging Manufacturing 26: 141-149.

[8] Cerrina, F., Marrian, C. (1996) Path to nanolithography. MRS Bulletin 21: 56.

[9] Ziberi, B., Frost, F., Rauschenbach, B. (2006) Pattern transitions on Ge surfaces during low-energy ion beam erosion. Applied Physics Letters 88: 173115-173111.

[10] Schubert, E., Hoche, T., Frost, F., Rauschenbach, B. (2005) Nanostructure fabrication by glancing angle ion beam assisted deposition of silicon. Applied Physics A (Materials Science Processing) A81: 481-486.

[11] Ziberi, B., Frost, F., Rauschenbach, B., Hoche, T. (2005) Highly ordered self-organized dot patterns on Si surfaces by low-energy ion-beam erosion. Applied Physics Letters 87: 33113-33111.

[12] Wang, Z.B., Hong, M.H., Luk'yanchuk, B.S., Lin, Y., Wang, Q.F., Chong, T.C. (2004) Angle effect in laser nanopatterning with particle-mask. Journal of Applied Physics 96: 6845-6850.

[13] Kuiper, S., van Wolferen, H., van Rijn, G., Nijdam, W., Krijnen, G., Elwenspoek, M. (2001) Fabrication of microsieves with sub-micron pore size by laser interference lithography. Journal of Micromechanics and Microengineering 11: 33-37.

[14] Mucklich, F., Lasagni, A., Daniel, C. (2006) Laser interference metallurgy - Using interference as a tool for micro/nano structuring. International Journal of Materials Research 97: 1337-1344.

[15] Kelly, M.K., Rogg, J., Nebel, C.E., Stutzmann, M., Katai, S. (1998) High-resolution thermal processing of semiconductors using pulsed-laser interference patterning. Physica Status Solidi (A) Applied Research 166: 651-657.

[16] Dekker, M. (1998) Microlithography-Science and technology. Eds: J.R.sheats, B. W. Smith.

[17] Boto, A.N., Kok, P., Abrams, D.S., Braunstein, S.L., Williams, C.P., Dowling, J.P. (2000) Quantum interferometric optical lithography: exploiting entanglement to beat the diffraction limit. Physical Review Letters 85: 2733-2736.

[18] Geissler, M., Xia, Y. (2004) Patterning: Principles and some new developments. Advanced Materials 16: 1249-1269.

[19] Voet,A.: interscience Thesis,4: 245-259 1952.

[20] P. O. Hidber, W.H., E. Kim, G. M. Whitesides (1996): Langmuir, pp. 1375-1380.

[21] Suh, K.Y., Kim, Y.S., Lee, H.H. (2001) Capillary force lithography. Advanced Materials 13: 1386-1389.

[22] Khademhosseini, A., Jon, S., Suh, K.Y., Tran, T.-N.T., Eng, G., Yeh, J., Seong, J., Langer, R. (2003) Direct patterning of protein- and cell-resistant polymeric monolayers and microstructures. Advanced Materials 15: 1995-2000.

[23] Chou, S.Y., Kelmel, C., Jian, G. (2002) Ultrafast and direct imprint of nanostructures in silicon. Nature 417: 835-837.

[24] Haghiri-Gosnet, A.M., Vieu, C., Simon, G., Carcenac, F., Madouri, A., Chen, Y., Rousseaux, F., Launois, H. (1995) Fabrication of sub-30 nm masks for x-ray nanolithography. Journal of Vacuum Science & Technology B: Microelectronics Processing and Phenomena 13: 3066-3069.

[25] Devolder, T., Vieu, C., Bernas, H., Ferre, J., Chappert, C., Gierak, J., Jamet, J.P., Aign, T., Meyer, P., Chen, Y., Rousseaux, F., Mathet, V., Launois, H., Kaitasov, O. (1999) Ion beam-induced magnetic patterning at the sub-0.1 μm level. Comptes Rendus de l'Academie des Sciences, Serie II (Mecanique, Physique, Astronomie) 327: 915-923.

[26] Bernas, H., Devolder, T., Chappert, C., Ferre, J., Kottler, V., Chen, Y., Vieu, C., Jamet, J.P., Mathet, V., Cambril, E., Kaitasov, O., Lemerle, S., Rousseaux, F., Launois, H. (1999) Ion beam induced magnetic nanostructure patterning. Nuclear Instruments & Methods in Physics Research, Section B: Beam Interactions with Materials and Atoms 148: 872-879.

[27] Vieu, C., Carcenac, F., Pepin, A., Chen, Y., Mejias, M., Lebib, A., Manin-Ferlazzo, L., Couraud, L., Launois, H. (2000): Electron beam lithography, resolution limits and applications. Elsevier, Ile de Porquerolles, France, pp. 111-117.

[28] Fujita, J., Watanabe, H., Ochiai, Y., Manako, S., Tsai, J.S., Matsui, S. (1995) Sub-10 nm

lithography and development properties of inorganic resist by scanning electron beam. Applied Physics Letters 66: 3065.

[29] Lercel, M.J., Craighead, H.G., Parikh, A.N., Seshadri, K., Allara, D.L. (1996) Sub-10 nm lithography with self-assembled monolayers. Applied Physics Letters 68: 1504.

[30] Medeiros, D.R., Aviram, A., Guarnieri, C.R., Huang, W.S., Kwong, R., Magg, C.K., Mahorowala, A.P., Moreau, W.M., Petrillo, K.E., Angelopoulos, M. (2001) Recent progress in electron-beam resists for advanced mask-making. IBM Journal of Research and Development 45: 639-650.

[31] Carr, D.W., Craighead, H.G. (1997) Fabrication of nanoelectromechanical systems in single crystal silicon using silicon on insulator substrates and electron beam lithography. Journal of Vacuum Science & Technology B: Microelectronics Processing and Phenomena 15: 2760.

[32] Herman, I.P. (1984): LASER FABRICATION OF INTEGRATED CIRCUITS. In Laser Processing and Diagnostics, Proceedings of an International Conference., Springer-Verlag (Springer Series in Chemical Physics 39), Berlin, West Ger, Linz, Austria, pp. 396-416 BN - 393-540-13843-13849.

[33] Delfino, M. (1983): Laser activated flow for integrated circuit fabrication. In Laser Processing of Semiconductor Devices, 18-19 Jan. 1983 Proceedings of the SPIE - The International Society for Optical Engineering, Los Angeles, CA, USA, pp. 32-37.

[34] Chao, W., Yuen Chuen, C., Lam, Y.L. (2002) Fabrication of diffractive optical elements with arbitrary surface-relief profile by direct laser writing. Optical Engineering 41: 1240-1245.

[35] P.L. Burn, A. Kraft, Bradley, A.R. Brown, R.H. Friend, R.W. Gymer (1992) Nature 356.

[36] Huang, S.M., Hong, M.H., Wu, D.J., Van, L.H., Ong, T.S., Luk'yanchuk, B.S., Chong, T.C. (2003): Three-dimensional optical storage by use of an ultrafast laser. In Optical data storage 2003, 11-14 May 2003 Proceedings of the SPIE - The International Society for Optical Engineering, SPIE-Int. Soc. Opt. Eng, Vancouver, BC, Canada, pp. 264-268.

[37] Joohan, K., Xianfan, X. (2003) Excimer laser fabrication of polymer microfluidic devices. Journal of Laser Applications 15: 255-260.

[38] Mansuripur, M., Khulbe, P.K., Kuebler, S.M., Perry, J.W., Giridhar, M.S., Erwin, J.K., Seong, K., Marder, S.R., Peyghambarian, N. (2003): Information storage and retrieval using macromolecules as storage media. In Optical data storage 2003, 11-14 May 2003 Proceedings of the SPIE - The International Society for Optical Engineering, SPIE-Int. Soc. Opt. Eng, Vancouver, BC, Canada, pp. 231-243.

[39] Matsuo, S., Kondo, T., Juodkazis, S., Mizeikis, V., Misawa, H. (2002): Fabrication of three-dimensional photonic crystals by femtosecond laser interference. SPIE-Int. Soc. Opt. Eng, San Jose, CA, USA, pp. 327-334.

[40] Pan, C.T., Shen, S.C. (2004) Design and fabrication of polymeric micro-optical components using excimer laser ablation. Materials Science and Technology 20: 270-274.

[41] Burns, M.A., Johnson, B.N., Brahmasandra, S.N., Handique, K., Webster, J.R., Krishnan, M.,

Sammarco, T.S., Man, P.M., Jones, D., Heldsinger, D., Mastrangelo, C.H., Burke, D.T. (1998) Integrated nanoliter DNA analysis device. Science 282: 484-487.

[42] Duffy, D.C., McDonald, J.C., Schueller, O.J.A., Whitesides, G.M. (1998) Rapid prototyping of microfluidic systems in poly(dimethylsiloxane). Analytical Chemistry 70: 4974-4984.

[43] Jacobson, S.C., Hergenroder, R., Koutny, L.B., Warmack, R.J., Ramsey, J.M. (1994) Effects of injection schemes and column geometry on the performance of microchip electrophoresis devices. Analytical Chemistry 66: 1107-1113.

[44] Khandurina, J., Jacobson, S.C., Waters, L.C., Foote, R.S., Ramsey, J.M. (1999) Microfabricated porous membrane structure for sample concentration and electrophoretic analysis. Analytical Chemistry 71: 1815-1819.

[45] Fluri, K., Fitzpatrick, G., Chiem, N., Harrison, D.J. (1996) Integrated capillary electrophoresis devices with an efficient postcolumn reactor in planar quartz and glass chips. Analytical Chemistry 68: 4285- 4290.

[46] Kytai Truong Nguyen, J.L.W. (2002) Photopolymerizable hydrogels for tissue engineering applications. Biomaterials 23: 4307–4314.

[47] Nayak, P., Mishra, D.K., Parida, D., Sahoo, K.C., Nanda, M., Lenka, S., Nayak, P.L. (1997) Polymers from renewable resources. IX. Interpenetrating polymer networks based on castor oil polyurethane poly(hydroxyethyl methacrylate): synthesis, chemical, thermal, and mechanical properties. Journal of Applied Polymer Science 63: 671-679.

[48] Narasimhan, J., Papautsky, I. (2004) Polymer embossing tools for rapid prototyping of plastic microfluidic devices. Journal of Micromechanics and Microengineering 14: 96-103.

[49] Pfleging, W., Hanemann, T., Bernauer, W., Torge, M. (2002): Laser micromachining of polymeric mold inserts for rapid prototyping of PMMA devices via photomolding. In Photon Processing in Microelectronics and Photonics, 21-24 Jan. 2002 Proceedings of the SPIE - The International Society for Optical Engineering, SPIE-Int. Soc. Opt. Eng, San Jose, CA, USA, pp. 318-329.

[50] Yao, L., Liu, B., Chen, T., Liu, S., Zuo, T. (2005) Micro flow-through PCR in a PMMA chip fabricated by KrF excimer laser. Biomedical Microdevices 7: 253-257.

[51] Li, B., Yu, H., Sharon, A., Zhang, X. (2004) Rapid three-dimensional manufacturing of microfluidic structures using a scanning laser system. Applied Physics Letters 85: 2426-2428.

[52] Franke, H., Sterkenburgh, T. (1994): Patterning polymer surfaces by laser ablation for integrated optics. In Proceedings of the 1994 IEEE 4th International Conference on Properties and Applications of Dielectric Materials. Part 1 (of 2), Jul 3-8 1994, IEEE, Piscataway, NJ, USA, Brisbane, Aust, pp. 208-210.

[53] Srinivasan, R. (1993) Ablation of polymethyl methacrylate films by pulsed (ns) ultraviolet and infrared lasers: A comparative study by ultrafast imaging. Journal of Applied Physics 73: 2743-2750.

[54] Cheng, J.-Y., Wei, C.-W., Hsu, K.-H., Young, T.-H. (2004) Direct-write laser

micromachining and universal surface modification of PMMA for device development. Sensors and Actuators B (Chemical) B99: 186-196.

[55] Dinger, C., Sterkenburgh, T., Holler, T., Franke, H. (1993): Patterning multimode polymeric lightguides using a CO₂ laser. In Nonconducting Photopolymers and Applications, 20-21 July 1992. Proceedings of the SPIE - The International Society for Optical Engineering, San Diego, CA, USA, pp. 278-287.

[56] Klank, H., Kutter, J.P., Geschke, O. (2002) CO_2-laser micromachining and back-end processing for rapid production of PMMA-based microfluidic systems. Lab on a Chip 2: 242-246.

[57] Snakenborg, D., Klank, H., Kutter, J.P. (2004) Microstructure fabrication with a CO_2 laser system. Journal of Micromechanics and Microengineering 14: 182-189.

[58] Modest, M.F. (1996) Three-dimensional, transient model for laser machining of ablating/decomposing materials. International Journal of Heat and Mass Transfer 39: 221-234.

[59] Atanasov, P.A., Baeva, M.G. (1997): CW CO_2 laser cutting of plastics. In XI International Symposium on Gas Flow and Chemical Lasers and High Power Laser Conference, 25-30 Aug. 1996. Proceedings of the SPIE - The International Society for Optical Engineering, SPIE-Int. Soc. Opt. Eng, Edinburgh, UK, pp. 772-775.

[60] Berrie, P.G., Birkett, F.N. (1980) DRILLING AND CUTTING OF POLYMETHYL METHACRYLATE (PERSPEX) BY CO_2 LASER. Optics and Lasers in Engineering 1: 107-129.

[61] Zissi, S., Bertsch, A., Jezequel, J.Y., Corbel, S., Lougnot, D.J., Andre, J.C. (1996) Stereolithography and microtechniques. Microsystem Technologies 2: 97-102.

[62] Takagi, T., Nakajima, N. (1993): Photoforming applied to fine machining. Publ by IEEE, Piscataway, NJ, USA, Fort Lauderdale, FL, USA, pp. 173-178.

[63] Ikuta, K., Hirowatari, K. (1993): Real three dimensional micro fabrication using stereo lithography and metal molding. IEEE, Fort Lauderdale, FL, USA, pp. 42-47.

[64] Zhang, X., Jiang, X.N., Sun, C. (1998): Micro-stereolithography for MEMS. ASME, Anaheim, CA, USA, pp. 3-9.

[65] Bertsch, A., Jiguet, S., Bernhard, P., Renaud, P. (2003): Microstereolithography: A review. Materials Research Society, Boston, MA, United States, pp. 3-15.

[66] Bertsch, A., Zissi, S., Jezequel, J.Y., Corbel, S., Andre, J.C. (1997) Microstereophotolithography using a liquid crystal display as dynamic mask-generator. Microsystem Technologies 3: 42-47.

[67] Chatwin, C., Farsari, M., Huang, S., Heywood, M., Birch, P., Young, R., Richardson, J. (1998) UV microstereolithography system that uses spatial light modulator technology. Applied Optics 37: 7514-7522.

[68] Monneret, S., Loubere, V., Corbel, S. (1999): Microstereolithography using a dynamic mask generator and a noncoherent visible light source. SPIE-Int. Soc. Opt. Eng, Paris, France, pp. 553-561.

[69] Sun, C., Fang, N., Wu, D.M., Zhang, X. (2005) Projection micro-stereolithography using digital micro-mirror dynamic mask. Sensors and Actuators, A: Physical 121: 113-120.

[70] Wenhui, Z., Kuebler, S.M., Braun, K.L., Tianyue, Y., Cammack, J.K., Ober, C.K., Perry, J.W., Marder, S.R. (2002) An efficient two-photon-generated photoacid applied to positive-tone 3D microfabrication. Science 296: 1106-1109.

[71] Kawata, S., Sun, H.B., Tanaka, T., Takada, K. (2001) Finer features for functional microdevices. Nature 412: 697-698.

[72] Maruo, S., Ikuta, K., Ogawa, M. (2004): Laser-driven multi-degrees-of-freedom nanomanipulators produced by two-photon microstereolithography. SPIE - The International Society for Optical Engineering, Nara, Japan, pp. 89-94.

[73] Maruo, S., Inoue, H. (2006) Optically driven micropump produced by three-dimensional two-photon microfabrication. Applied Physics Letters 89: 144101-144101.

[74] Terris, B.D., Weller, D., Folks, L., Baglin, J.E.E., Kellock, A.J., Rothuizen, H., Vettiger, P. (2000) Patterning magnetic films by ion beam irradiation. Journal of Applied Physics 87: 7004.

[75] Hori, M. (1999) Near-field Nano-optics. Kluwer Academic, New York.

[76] Betzig, E., Trautman, J.K., Wolfe, R., Gyorgy, E.M., Finn, P.L., Kryder, M.H., Chang, C.H. (1992) Near-field magneto-optics and high density data storage. Applied Physics Letters 61: 142.

[77] Allegrini, M., Patane, S., Arena, A., Andreozzi, L., Faetti, M., Giordano, M. (2002) Near-field optical writing on azo-polymethacrylate spin-coated films. Optics Communications 210: 37-41.

[78] Munzer, H.J., Mosbacher, M., Bertsch, M., Dubbers, O., Burmeister, F., Pack, A., Wannemacher, R., Runge, B.U., Bauerle, D., Boneberg, J., Leiderer, P. (2002): Optical near field effects in surface nanostructuring and laser cleaning. SPIE-Int. Soc. Opt. Eng, Singapore, pp. 180-183.

[79] Halfpenny, D.R., and Kane, D. M., (1999) A Quantitative Analysis of Single Pulse Ultraviolet Dry Laser Cleaning. J. Appl. Phys. 86: 6641-6646.

[80] Ikawa, T., Mitsuoka, T., Hasegawa, L., Tsuchimori, M., Watanabe, O., Kawata, K., Egami, C., Sugihara, O., Okamoto, N. (2000) Optical near field induced change in viscoelasticity on an azobenzene-containing polymer surface. Journal of Physical Chemistry B 104: 9055-9058.

[81] Moreno, F., and F. Gonzalez, (1998) Light scattering from microstructures. Springer.

[82] Munzer, H.J., Mosbacher, M., Bertsch, M., Zimmermann, J., Leiderer, P., Boneberg, J. (2001): Local field enhancement effects for nanostructuring of surfaces. Blackwell Science, Enschede, Netherlands, pp. 129-135.

[83] Jakubiak, R., Bunning, T.J., Vaia, R.A., Natarajan, L.V., Tondiglia, V.P. (2003) Electrically switchable, one-dimensional polymeric resonators from holographic photopolymerization: A new approach for active photonic bandgap materials. Advanced Materials 15: 241-244.

[84] Jakubiak, R., Natarajan, L.V., Tondiglia, V., He, G.S., Prasad, P.N., Bunning, T.J., Vaia, R.A. (2004) Electrically switchable lasing from pyrromethene 597 embedded holographic-polymer dispersed liquid crystals. Applied Physics Letters 85: 6095-6097.

[85] Divliansky, I.B., Shishido, A., Khoo, I.C., Mayer, T.S., Pena, D., Nishimura, S., Keating, C.D., Mallouk, T.E. (2001) Fabrication of two-dimensional photonic crystals using interference lithography and electrodeposition of CdSe. Applied Physics Letters 79: 3392.

[86] Mutzel, M., Tandler, S., Haubrich, D., Meschede, D., Peithmann, K., Flaspohler, M., Buse, K. (2002) Atom lithography with a holographic light mask. Physical Review Letters 88: 083601-083601.

[87] Shishido, A., Diviliansky, I.B., Khoo, I.C., Mayer, T.S., Nishimura, S., Egan, G.L., Mallouk, T.E. (2001) Direct fabrication of two-dimensional titania arrays using interference photolithography. Applied Physics Letters 79: 3332.

[88] Solak, H.H., David, C., Gobrecht, J., Wang, L., Cerrina, F. (2002) Multiple-beam interference lithography with electron beam written gratings. Journal of Vacuum Science and Technology B: Microelectronics and Nanometer Structures 20: 2844-2848.

[89] Kim, D.Y., Tripathy, S.K., Lian, L., Kumar, J. (1995) Laser-induced holographic surface relief gratings on nonlinear optical polymer films. Applied Physics Letters 66: 1166-1168.

[90] Phillips, H.M., Callahan, D.L., Sauerbrey, R., Szabo, G., Bor, Z. (1991) Sub-100 nm lines produced by direct laser ablation in polyimide. Applied Physics Letters 58: 2761-2763.

[91] Kuhn, W., Ber. Deutsch. (1930) Chem. Ges. 63: 1503-1509.

[92] Simha, R. (1941) J. Appl. Phys. 12: 569-578.

[93] Chiantore, O., Luda di Cortemiglia, M.P., Guaita, M. (1989) Changes of degree of polymerisation in the thermal degradation of poly(methyl methacrylate). Polymer Degradation and Stability 24: 113-126.

[94] Kashiwagi, T., Inaba, A., Brown, J.E. (1986): Differences in PMMA degradation Characteristics and their effects on its fire properities. In Fire Safety Science, Proceedings of the First International Symposium., Hemisphere Publ Corp, Washington, DC, USA, Berkeley, CA, USA, pp. 483-493 BN - 480-89116-89456-89111.

[95] Joeckle, R., Rapp, G., Sontag, A. (1991): Boiling process in PMMA irradiated by CO_2, DF and HF laser radiations. In 8th International Symposium on Gas Flow and Chemical Lasers Part 2 (of 2), Sep 10-14 1990, Publ by Int Soc for Optical Engineering, Bellingham, WA, USA, Madrid, Spain, pp. 683-687.

[96] Choi, W.C., Chryssolouris, G. (1995) Analysis of the laser grooving and cutting processes. Journal of Physics D (Applied Physics) 28: 873-878.

[97] Dajun Yuan, S.D. (2007) Experimental and theoretical analysis of direct-write laser micromachining of polymethyl methacrylate by CO_2 laser ablation. Journal of applied physics 101.

[98] JP Fouassier, J.R.: Radiation Curing in Polymer Science and Technology. Elsevier, London 1993.

[99] Geogie, O.: Principles of polymerization. Wiley, New York 1991.

[100] Fouassier JP, R.J.: Lasers in polymer science and technology. CRC Press, Boca Taton, FL 1990.

[101] Albot, R.: Photoreactive polymers: The science and technology of resists. Wiley, New York 1989.

[102] JP, Fouassier: Photoinitiation, photopolymerization and photocuring: Fundamentals and applications. Hanser, Munich Vienna, New York 1995.

[103] Jacbs, P.F.: Rapid Prototyping &Manufacturing: Fundamentals of Stereolithography. Society of Manufacturing Engineers, Dearborn, MI 1992.

[104] Hoffman, A.S. (2002) Hydrogels for biomedical applications. Advanced Drug Delivery Reviews 54: 3-12.

[105] Drury, J.L., Mooney, D.J. (2003) Hydrogels for tissue engineering: Scaffold design variables and applications. Biomaterials 24: 4337-4351.

[106] DeRossi, D.K..; Osada, Y.; Yamauchi: A. Polymer Gels: Fundamentals and Biomedical Applications. Plenum Press, New York 1991.

[107] Hennink, W.E., Van Nostrum, C.F. (2002) Novel crosslinking methods to design hydrogels. Advanced Drug Delivery Reviews 54: 13-36.

[108] Akiyoshi, K., Kang, E.-C., Kurumada, S., Sunamoto, J., Principi, T., Winnik, F.M. (2000) Controlled association of amphiphilic polymers in water: Thermosensitive nanoparticles formed by self-assembly of hydrophobically modified pullulans and poly(N-isopropylacrylamides). Macromolecules 33: 3244-3249.

[109] Eddington, D.T., Beebe, D.J. (2004) Flow control with hydrogels. Advanced Drug Delivery Reviews 56: 199-210.

[110] Tanaka, T., Fillmore, D., Shao-Tang, S., Nishio, I., Swislow, G., Shah, A. (1980) Phase transitions in ionic gels. Physical Review Letters 45: 1636-1639.

[111] Jones, C.D., Lyon, L.A. (2000) Synthesis and characterization of multiresponsive core-shell microgels. Macromolecules 33: 8301-8306.

[112] Saunders, B.R., Crowther, H.M., Morris, G.E., Mears, S.J., Cosgrove, T., Vincent, B. (1999) Factors affecting the swelling of poly(N-isopropylacrylamide) microgel particles: fundamental and commercial implications. Colloids and Surfaces A: Physicochemical and Engineering Aspects 149: 57-64.

[113] J L Hill-West, S.M.C., M J Slepian, and J A Hubbell (1994) Inhibition of thrombosis and intimal thickening by in situ photopolymerization of thin hydrogel barriers. Proc Natl Acad Sci U

S A 91: 5967–5971.

[114] Sawhney, A.S., Pathak, C.P., van Rensburg, J.J., Dunn, R.C., Hubbell, J.A. (1994) Optimization of photopolymerized bioerodible hydrogel properties for adhesion prevention. Journal of Biomedical Materials Research 28: 831-838.

[115] Hill West, J.L.C., S M Dunn, R C : Hubbell, J A (1994) Efficacy of a resorbable hydrogel barrier, oxidized regenerated cellulose, and hyaluronic acid in the prevention of ovarian adhesions in a rabbit model. Fertil-Steril. 62: 630-634.

[116] Chowdhury SM, H.J. (1996) Adhesion prevention with ancrod released via a tissue-adherent hydrogel. J Surg Res 61: 58-64.

[117] Hubbell, Y.A.a.J.A. (2000) Intraarterial protein delivery via intimally-adherent bilayer hydrogels. Journal of Controlled Release 64: 205-215.

[118] Quinn, C.P., Pathak, C.P., Heller, A., Hubbell, J.A. (1995) Photo-crosslinked copolymers of 2-hydroxyethyl methacrylate, poly(ethylene glycol) tetra-acrylate and ethylene dimethacrylate for improving biocompatibility of biosensors. Biomaterials 16: 389-396.

[119] Russell, R.J., Pishko, M.V., Gefrides, C.C., McShane, M.J., Cote, G.L. (1999) Fluorescence-based glucose biosensor using Concanavalin A and dextran encapsulated in a Poly(ethylene glycol) hydrogel. Analytical Chemistry 71: 3126-3132.

[120] Pathak, C.P., Sawhney, A.S., Hubbell, J.A. (1992) Rapid photopolymerization of immunoprotective gels in contact with cells and tissue. Journal of the American Chemical Society 114: 8311.

[121] Elisseeff, J., McIntosh, W., Anseth, K., Riley, S., Ragan, P., Langer, R. (2000) Photoencapsulation of chondrocytes in poly(ethylene oxide)-based semi-interpenetrating networks. Journal of Biomedical Materials Research 51: 164-171.

[122] Awhney, A.S., Pathak, C.P., Hubbell, J.A. (1993) Bioerodible hydrogels based on photopolymerized poly(ethylene glycol)-co-poly(α-hydroxy acid) diacrylate macromers. Macromolecules 26: 581-587.

[123] In-Sook Kima, (2000) Self-assembled hydrogel nanoparticles composed of dextran and poly(ethylene glycol) macromer. International Journal of Pharmaceutics 205: 109-116.

[124] Martens, P., Anseth, K.S. (2000) Characterization of hydrogels formed from acrylate modified poly(vinyl alcohol) macromers. Polymer 41: 7715-7722.

[125] Matsuda, T.M., M J : Miwa, H : Sakurai, K : Iida, F (1992) Photoinduced prevention of tissue adhesion. ASAIO-J 38: 154-157.

[126] Bulpitt, P., Aeschlimann, D. (1999) New strategy for chemical modification of hyaluronic acid: Preparation of functionalized derivatives and their use in the formation of novel biocompatible hydrogels. Journal of Biomedical Materials Research 47: 152-169.

[127] Kim, S.-H., Chu, C.-C. (2000) Synthesis and characterization of dextran-methacrylate hydrogels and structural study by SEM. Journal of Biomedical Materials Research 49: 517-527.

[128] Jacobs, P.F.: Rapid Prototyping &Manufacturing: Fundamentals of Stereolithography. Society of Manufacturing Engineers, Dearborn, MI 1992.

[129] Verhaegen, F.a.J.S. (2003) Monte Carlo modeling of external radiotherapy photon beams. Physics in Medicine and Biology 48: 107-164.

[130] Andreo, P. (1990) Monte Carlo techniques in medical radiation Physics. Physics in Medicine and Biology 36: 861-920.

[131] Ma, C.-M. (1998) Characterization of computer simulated radiotherapy beams for Monte-Carlo treatment planning. Radiation Physics and Chemistry 53: 329-344.

[132] Wilson, B.C. (1983) A monte carlo model for the absorption and flux distributions of light in tissue. Med. Phys 10: 824-830.

[133] Chiu D T, J.N.L., Huang S, Kane R S, Wargo C J, Choi I S (2000) Patterned deposition of cells and proteins onto surfaces by using three-dimensional microfluidic systems. Proc. Natl Acad. 97: 2408-2413

[134] Yin L, B.H.a.E.E. (2004) Scaffold topography alters intracellular calcium dynamics in cultured cardiomyocyte networks. Am. J. Physiol. Heart Circ. Physiol 287: 1276-1285.

[135] H, Elbat (2003) Tension development and nuclear eccentricity in topographically controlled cardiac syncytium. Biomed. Microdevices 5: 163-165.

[136] Motlagh D, Desai T A and Russell B (2003) Microtextured substrata alter gene expression, protein localization and the shape of cardiac myocytes. Biomaterials 24: 2463-2476.

[137] Tan J L, T.J., Pirone D M, Gray D S, Bhadriraju K and Chen C S (2003) Cells lying on a bed of microneedles: an approach to isolate mechanical force Proc. Natl Acad. Sci. USA 100: 1484-1489.

[138] Park J Y, R.J., Choi S K, Seo E, Cha J M, Ryu S, Kim J, Kim B and Lee S H (2005) Real-time measurement of the contractile forces of self-organized cardiomyocytes on hybrid biopolymer microcantilevers Anal. Chem. 77: 6571-6580.

[139] Harris, J.M., Zalipsky, S., Eds: Poly(ethylene glycol) Chemistry and Biological Applications;. ACS Symposium Series 680; American Chemical Society:, Washinton DC 1997.

[140] Graham, N.B.: Poly(Ethylene Glycol) Chemistry. Plenum Press, New York 1992.

[141] Chem, M. Negative Tone Photoresist formulation SU-8 2-25. Technical Data Sheet: 2.

[142] ciba Ciba® TINUVIN® 384-2 Technical Data Sheet.

[143] ciba Ciba® TINUVIN® 171 Technical Data Sheet.

[144] Chem, M. Positive Tone Photoresist formulation Shipley 1813. Technical Data Sheet.

[145] Espanet, A., Ecoffet, C., Lougnot, D.J. (1999) PEW: Photopolymerization by evanescent

waves. II. Revealing dramatic inhibiting effects of oxygen at submicrometer scale. Journal of Polymer Science, Part A: Polymer Chemistry 37: 2075-2085.

[146] Mele, E., Pisignano, D., Varda, M., Farsari, M., Filippidis, G., Fotakis, C., Athanassiou, A., Cingolani, R. (2006) Smart photochromic gratings with switchable wettability realized by green-light interferometry. Applied Physics Letters 88: 203124.

[147] Lecamp, L., Youssef, B., Bunel, C., Lebaudy, P. (1997) Photoinitiated polymerization of a dimethacrylate oligomer: 1. Influence of photoinitiator concentration, temperature and light intensity. Polymer 38: 6089-6096.

[148] Espanet, A., Dos Santos, G., Ecoffet, C., Lougnot, D.J. (1999): Photopolymerization by evanescent waves: characterization of photopolymerizable formulation for photolithography with nanometric resolution. Elsevier, Strasbourg, France, pp. 87-92.

[149] Hiroshi Itoh, Y.A., Masayasu Furuse, Yasuharu Noishiki, and Teruo Miyata (2000) A Honeycomb Collagen Carrier for Cell Culture as a Tissue Engineering Scaffold. Artificial Organs 25: 213-217.

[150] Yang, S., Chen, G., Megens, M., Ullal, C.K., Han, Y.-J., Rapaport, R., Thomas, E.L., Aizenberg, J. (2005) Functional biomimetic microlens arrays with integrated pores. Advanced Materials 17: 435-438.

[151] Ullal, C.K., Maldovan, M., Wohlgemuth, M., Thomas, E.L., White, C.A., Shu, Y. (2003) Triply periodic bicontinuous structures through interference lithography: a level-set approach. Journal of the Optical Society of America A (Optics, Image Science and Vision) 20: 948-954.

[152] Aizenberg, J., Tkachenko, A., Weiner, S., Addadi, L., Hendler, G. (2001) Calcitic microlenses as part of the photoreceptor system in brittlestars. Nature 412: 819-822.

[153] J. Y. Yang, D.H.K., J.L. Hendricks, M. Leach, R. Northey, D. C. Martin (2005) Surfactant-Templated poly(3,4-ethylenedioxythiophene) (PEDOT) Conducting Polymer On Microfabricated Neural Probes. Acta Biomaterialia 1: 125-136.

[154] T. Aernouts, P.V., W. Geens, J. Poortmans, P. Heremans, S. Borghs, R. Mertens, R. Andriessen, L. Leenders (2004) Printable anodes for flexible organic solar cell modules. Thin Solid Films 451: 22-25.

[155] V. G. Khomenko, V.Z.B., A. S. Katashinkii, Electrochimca (2005) Acta Biomaterialia 50 55-62.

[156] Holdcroft, S. (2001) Advanced Materials 13 798-812.

[157] G. Venugopal, X.Q., G.E. Johnson, F. Houlihan, E. Chin, O. Nalamasu (1995) chem. mater. 7 379-390.

[158] Denkov, N.D., Velev, O.D., Kralchevsky, P.A., Ivanov, I.B., Yoshimura, H., Nagayama, K. (1992) Mechanism of formation of two-dimensional crystals from latex particles on substrates. Langmuir 8: 3183-3190.

[159] Kralchevsky, P.A., Paunov, V.N. (1992) Contribution of ionic correlations to excess free

energy and disjoining pressure of thin liquid films. 1. Electric double layer inside the film. Colloids and Surfaces 64: 245.

[160] Paunov, V.N., Kralchevsky, P.A. (1992) Contribution of ionic correlations to excess free energy and disjoining pressure of thin liquid films. 2. Electric double layers outside the film. Colloids and Surfaces 64: 265.

[161] Ivanov, I.B., Kralchevsky, P.A., Dimitrov, A.S., Nikolov, A.D. (1992) Dynamics of contact lines in foam films. Advances in Colloid and Interface Science 39: 77-101.

[162] Hulteen, J.C., Van Duyne, R.P. (1995): Nanosphere lithography: a materials general fabrication process for periodic particle array surfaces. Denver, CO, USA, pp. 1553-1558.

[163] Micheletto, R., Fukuda, H., Ohtsu, M. (1995) Simple method for the production of a two-dimensional, ordered array of small latex particles. Langmuir 11: 3333.

[164] Max Born, Email Wolf: Principles of Optics: Electromagnetic theory of propagation interference and diffraction of light. Cambridge University press, london 1999.

[165] Alex J. Heltzel, S.T., John R. Howell, Shaochen Chen (2005) Analytical and experimental investigation of laser microsphere interaction for nanoscale surface modification. Journal of Heat Transfer 127: 1231-1235.